

The US/UK

World Magnetic Model

for 2015-2020

Arnaud Chulliat
Patrick Alken
Manoj Nair
Adam Woods
Stefan Maus

NOAA National Geophysical Data
Center
325 Broadway
NOAA E/GC3
Boulder, CO 80305-3328
USA

Susan Macmillan
Ciaran Beggan
Brian Hamilton
Victoria Ridley
Alan Thomson

British Geological Survey
Geomagnetism Team
Murchison House
West Mains Road
Edinburgh EH9 3LA
UK

Bibliographic Reference:

Chulliat, A., S. Macmillan, P. Alken, C. Beggan, M. Nair, B. Hamilton, A. Woods, V. Ridley, S. Maus and A. Thomson, 2015, *The US/UK World Magnetic Model for 2015-2020: Technical Report*, National Geophysical Data Center, NOAA. doi: [10.7289/V5TB14V7](https://doi.org/10.7289/V5TB14V7)



**British
Geological Survey**

NATIONAL ENVIRONMENT RESEARCH COUNCIL



ABSTRACT

This report contains a complete description of the World Magnetic Model (WMM) 2015. [Section 1](#) contains information that users of WMM2015 require in order to implement the model and software in navigation and heading systems, and to understand magnetic charts, poles and geomagnetic coordinate systems. [Section 2](#) contains a detailed summary of the data used and the modeling techniques employed. [Section 3](#) contains an assessment of the model uncertainties and a description of the error model provided with the WMM2015. [Section 4](#) contains charts of all the magnetic elements at 2015.0 and their expected annual rates of change between 2015.0 and 2020.0. These predicted changes are based upon the best knowledge of the geomagnetic main field evolution at the time the WMM was released.

Sponsored by the U.S. National Geospatial-Intelligence Agency (NGA) and the U.K. Defence Geographic Centre (DGC), the World Magnetic Model (WMM) is produced by the U.S. National Oceanic and Atmospheric Administration's National Geophysical Data Center (NOAA/NGDC) and the British Geological Survey (BGS). It is the standard model used by the U.S. Department of Defense (DoD), the U.K. Ministry of Defence, the North Atlantic Treaty Organization (NATO) and the International Hydrographic Organization (IHO), for navigation, attitude and heading referencing systems using the geomagnetic field. It is also used widely in civilian navigation and heading systems.

CONTACTS

The model, associated software, digital charts and documentation are available at <http://www.ngdc.noaa.gov/geomag/WMM/> or by contacting NGDC, BGS, or NGA.

Please cite using these identifiers. Recommended usage and additional information available at:

Technical Report – doi:[10.7289/V5TB14V7](https://doi.org/10.7289/V5TB14V7)

Dataset – doi:[10.7289/V5TH8JNW](https://doi.org/10.7289/V5TH8JNW)

MODEL AND SOFTWARE SUPPORT

National Geophysical Data Center

NOAA E/GC 3
325 Broadway
Boulder, CO 80305-3328
USA

Attention: Manoj Nair or Arnaud Chulliat
Phone: + (303) 497-4642 or -6522
Email: Manoj.C.Nair@noaa.gov or Arnaud.Chulliat@noaa.gov
Web: <http://www.ngdc.noaa.gov/geomag/WMM/>

British Geological Survey

Murchison House
West Mains Road
Edinburgh, EH9 3LA
UK
Attention: Susan Macmillan or Ciaran Beggan
Phone: + 44 131 667 1000
Email: smac@bgs.ac.uk or ciar@bgs.ac.uk
Web: <http://www.geomag.bgs.ac.uk/research/modelling/WorldMagneticModel.html>

APPLICABILITY WITHIN THE U.S. DEPARTMENT OF DEFENSE

National Geospatial-Intelligence Agency

Geomatics Office
NGA-SN, Mail Stop L-41
3838 Vogel Road
Arnold, MO 63010-6238
U.S.A.

Email: WGS84@nga.mil

APPLICABILITY WITHIN THE U.K. MINISTRY OF DEFENCE

Defence Geographic Centre

Matthew Shimell
MacLeod Building, Elmwood Avenue
Feltham, Middlesex
TW13 7AH
UK

Email: JFIGFndn-DGCRGeodesy01@mod.uk

Giles André
MacLeod Building, Elmwood Avenue
Feltham, Middlesex
TW13 7AH
UK

Email: JFIGFndn-DGCRGeoResearchHd@mod.uk

The NATO and military specifications for magnetic models are STANAG 7172 (NATO Standardization Agency, 2011) and MIL-W-89500 (Defense Mapping Agency, 1993). Magnetic model requirements that are more stringent than those set forth in these specifications should be addressed to NGDC and BGS (e.g., those that must include magnetic effects of the Earth's crust, ionosphere, or magnetosphere and/or require greater spatial or temporal resolution on a regional or local basis).

ACKNOWLEDGEMENTS

This work was carried out under the sponsorship of the U.S. National Geospatial-Intelligence Agency (NGA) and the UK Ministry of Defence through the Defence Geographic Centre (DGC). Heather McCullough (NOAA/NGDC) and Mara Sprain (NOAA/NCDC) edited and proofread this report. The maps of the geomagnetic elements were designed by Jesse Varner (NOAA/NGDC and Cooperative Institute for Research in the Environmental Sciences, CIRES), with support from Brian Meyer (NOAA/NGDC and CIRES). Susan McLean (NOAA/NGDC) is the U.S. manager for the WMM project, which is funded by NGA. NGA personnel oversee the WMM and Enhanced Magnetic Model (EMM) development, and reviewed this report and contributed to the error analysis. Data from the Swarm satellite mission were provided by the European Space Agency (ESA), supported by ESA member states. Other satellite data were provided by the Ørsted satellite mission and data center (operated by the Danish Technical University) and the CHAMP mission and data center (operated by Helmholtz Centre Potsdam – GFZ German Research Centre for Geosciences, Germany). Many institutes and agencies are involved in the operation of geomagnetic observatories around the world. In particular we would like to thank: Centre de Recherche en Astronomie Astrophysique et Geophysique, ALGERIA; Servicio Meteorologico Nacional, ARGENTINA; Universidad Nacional de la Plata, ARGENTINA; Geoscience Australia, AUSTRALIA; Zentralanstalt für Meteorologie und Geodynamik, AUSTRIA; Institut Royal Météorologique de Belgique, BELGIUM; CNPq-Observatório Nacional, BRAZIL; Academy of

Sciences, BULGARIA; Geological Survey of Canada, CANADA; Centro Meteorológico Regional Pacífico, CHILE; Academy of Sciences, CHINA; Seismological Bureau, CHINA; Academy of Sciences, CZECH REPUBLIC; Danish Technical University, DENMARK; Addis Ababa University, ETHIOPIA; Finnish Meteorological Institute, FINLAND; Sodankylä Geophysical Observatory, FINLAND; Institut de Physique du Globe de Paris, FRANCE; Ecole et Observatoire des Sciences de la Terre, FRANCE; Ludwig Maximilians University Munich, GERMANY; Alfred-Wegener-Institute for Polar & Marine Research, GERMANY; Helmholtz Centre Potsdam, GERMANY; Universities of Karlsruhe and Stuttgart, GERMANY; Institute of Geology and Mineral Exploration, GREECE; Academy of Sciences, HUNGARY; Eötvös Loránd Geophysical Institute of Hungary, HUNGARY; University of Iceland, ICELAND; Indian Institute of Geomagnetism, INDIA; National Geophysical Research Institute, INDIA; Meteorological and Geophysical Agency, INDONESIA; The Irish Meteorological Service, IRELAND; Survey of Israel, ISRAEL; Instituto Nazionale di Geofisica e Vulcanologia, ITALY; Japan Coast Guard, JAPAN; Japan Meteorological Agency, JAPAN; Geographical Survey Institute, JAPAN; Institute of the Ionosphere, KAZAKHSTAN; National Centre for Geophysical Research, LEBANON; Université d'Antananarivo, MADAGASCAR; Gan Meteorological Office, MALDIVES; Institute of Geological and Nuclear Sciences, NEW ZEALAND; University of Tromsø, NORWAY; Instituto Geofísico del Perú, PERU; Academy of Sciences, POLAND; Instituto Nacional de Geología, REPÚBLICA DE MOÇAMBIQUE; Geological Survey of Romania, ROMANIA; Academy of Sciences, RUSSIA; Institute of Solar-Terrestrial Physics, RUSSIA; Dept. of Agriculture, Forestry, Fisheries & Meteorology, SAMOA; Geomagnetic College Grocka, SERBIA & MONTENEGRO; Slovenska Akademia Vied, SLOVAKIA; National Research Foundation, SOUTH AFRICA; Observatori de l'Ebre, SPAIN; Real Instituto y Observatorio de la Armada, SPAIN; Instituto Geográfico Nacional, SPAIN; Sveriges Geologiska Undersökning, SWEDEN; Swedish Institute of Space Physics, SWEDEN; ETH Zurich, SWITZERLAND; Earthquake Research Institute, TURKEY; US Geological Survey, UNITED STATES OF AMERICA; British Geological Survey, UNITED KINGDOM; Academy of Sciences, UKRAINE; Ukrainian Antarctic Center, UKRAINE and National Centre for Science and Technology, VIETNAM. The INTERMAGNET program and the ICSU World Data System (primarily World Data Centre for Geomagnetism, Edinburgh) assist in the quality control and dissemination of observatory data. The magnetic activity indices K_p and D_{st} were computed and provided by Helmholtz Centre Potsdam, Germany and World Data Center for Geomagnetism in Kyoto, respectively. Solar wind data are measured by the Advanced Composition Explorer (ACE) satellite and made available by NASA. This model could not have been produced without the efforts of all of these institutes.

TABLE OF CONTENTS

| | |
|---|-----|
| Abstract | i |
| Contacts | ii |
| Acknowledgements | iii |
| Table of Contents | v |
| | |
| 1. The Model | 1 |
| 1.1 Introduction | 1 |
| 1.1.1 Magnetic elements | 2 |
| 1.1.2 Grid variation | 4 |
| 1.1.3 Range of the magnetic elements at the Earth's surface | 5 |
| 1.2 Relevant model equations | 6 |
| 1.3 The WMM2015 coefficients | 12 |
| 1.4 Singularities at the geographic poles | 13 |
| 1.5 Model equations numerical example | 14 |
| 1.6 Supersession of the models | 16 |
| 1.7 Policy on alternate software for the U.S. Department of Defense | 16 |
| 1.8 Magnetic poles and geomagnetic coordinate systems | 17 |
| 1.9 Description of charts | 19 |
| 1.10 Test values | 19 |
| | |
| 2. Construction of the Model | 21 |
| 2.1 Background on the geomagnetic field | 21 |
| 2.2 Data acquisition and quality control | 23 |
| 2.2.1 Satellite data | 23 |
| 2.2.2 Observatory data | 31 |
| 2.2.3 Other data and derived products | 37 |
| 2.3 Derivation of the model | 40 |
| 2.3.1 Parent model for main field coefficients | 41 |
| 2.3.2 Parent model for secular variation coefficients | 43 |
| 2.3.3 Validation process | 46 |
| | |
| 3. Model Uncertainties | 47 |
| 3.1 Sources of uncertainty | 47 |
| 3.2 Estimating uncertainty | 48 |
| 3.2.1 Formal commission error | 49 |
| 3.2.2 Commission error from model comparisons | 50 |
| 3.2.3 Crustal field and secular variation contributions – method #1 | 53 |
| 3.2.4 Crustal field and secular variation contributions – method #2 | 55 |
| 3.2.5 Disturbance field contribution | 58 |
| 3.3 Total error budget | 60 |
| 3.4 Error model | 61 |
| | |
| 4. Charts | 64 |
| 5. References and bibliography | 105 |

1. THE MODEL

1.1 INTRODUCTION

The Earth is like a giant magnet. At every location on or above the Earth, its magnetic field has a more or less well-known direction, which can be used as a reference frame to orient ships, aircraft, satellites, antennas, drilling equipment and handheld devices. At some places on the globe the horizontal direction of the magnetic field coincides with the direction of geographic north (“true” north), but in general this is not the case. The angular amount by which the horizontal direction of the magnetic field differs from true north is called the magnetic declination, or simply declination (D , see Figure 1). This is the correction required to convert between a magnetic bearing and a true bearing. The main utility of the World Magnetic Model (WMM) is to provide magnetic declination for any desired location on the globe. In addition to the magnetic declination, the WMM also provides the complete geometry of the field from 1 km below the Earth’s surface to 850 km above the surface. The magnetic field extends deep into the Earth and far out into space, but the WMM is not valid at these extremes.

The Earth’s magnetism has several sources. All sources affect a scientific or navigational instrument but only some are represented in the WMM. The strongest contribution, by far, is the magnetic field produced by the Earth’s liquid-iron outer core, called the “core field”. Magnetic minerals in the crust and upper mantle make a further contribution that can be locally significant. Electric currents induced by the flow of conducting sea water through the ambient magnetic field make a further, albeit weak, contribution to the observed magnetic field. All of these are of “internal” origin and included in the WMM. Deliberately excluded from the WMM by the data selection process and by other means are so-called “disturbance fields”. These are contributions arising from electric currents in the upper atmosphere and near-Earth space. These “external” magnetic fields are time-varying, and have a further effect. They induce electric currents in the Earth and oceans, producing secondary internal magnetic fields, which are considered part of the disturbance field and are not represented in the WMM.

The mathematical method of the WMM is an expansion of the magnetic potential into spherical harmonic functions to degree and order 12. The minimum wavelength resolved is $360^\circ / \sqrt{12 \times 13} = 28.8^\circ$ in arc-length, corresponding to 3200 km at the Earth's surface (see section 3.6.3 of Backus et al., 1996). The WMM is a model of those internal magnetic fields that are not part of the disturbance field and have spatial wavelengths exceeding 30° in arc-length. This works out to be almost the entire core field and the long-wavelength portion of the crustal and oceanic fields. In this report, the term "main field" refers to the portion of the Earth's magnetic field at epoch 2015.0 that is modeled by the WMM.

The core field changes perceptibly from year to year. This effect, called secular variation (SV), is accounted for in the WMM by a linear SV model. Specifically, a straight line is used as the model of the time-dependence of each coefficient of the spherical harmonic representation of the magnetic potential (see [section 1.2](#)). Due to unpredictable non-linear changes in the core field, the values of the WMM coefficients have to be updated every five years. The revision described in this report, WMM2015, is valid from 2015.0 to 2020.0.

1.1.1 MAGNETIC ELEMENTS

The geomagnetic field vector, \mathbf{B}_m , is described by seven elements. These are the northerly intensity X , the easterly intensity Y , the vertical intensity Z (positive downwards) and the following quantities derived from X , Y and Z : the horizontal intensity H , the total intensity F , the inclination angle I , (also called the dip angle and measured from the horizontal plane to the field vector, positive downwards) and the declination angle D (also called the magnetic variation and measured clockwise from true north to the horizontal component of the field vector). In the descriptions of X , Y , Z , H , F , I and D above, the vertical direction is perpendicular to the WGS 84 ellipsoid model of the Earth, the horizontal plane is perpendicular to the vertical direction, and the rotational directions clockwise and counter-clockwise are determined by a view from above (see Figure 1).

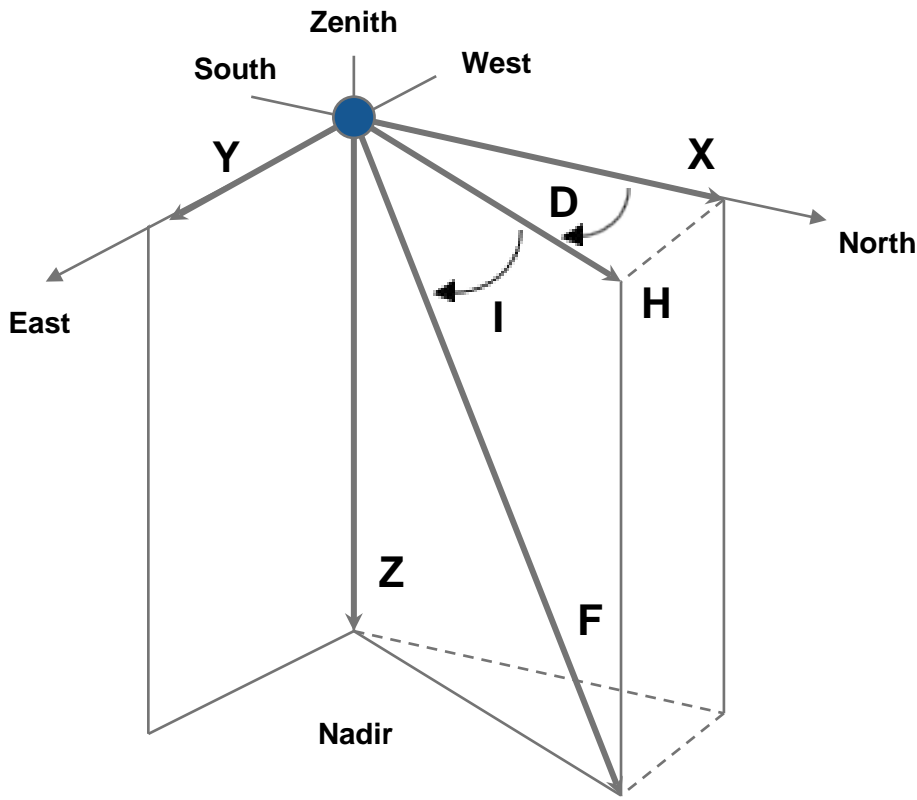


Figure 1: The seven elements of the geomagnetic field vector \mathbf{B}_m associated with an arbitrary point in space.

The quantities X , Y and Z are the sizes of perpendicular vectors that add vectorially to \mathbf{B}_m . Conversely, X , Y and Z can be determined from the quantities F , I and D (i.e., the quantities that specify the size and direction of \mathbf{B}_m).

1.1.2 GRID VARIATION

In the polar regions, or near the rotation axis of the Earth, the angle D changes strongly with a change in the longitude of the observer, and is therefore a poor measure of the direction of \mathbf{B}_m . For this reason, the WMM technical report and software have defined an auxiliary angle, GV , for the direction of \mathbf{B}_m in the horizontal plane. Its definition is:

$$\begin{aligned} GV &= D - \lambda \quad \text{for } \varphi > 55^\circ, \\ GV &= D + \lambda \quad \text{for } \varphi < -55^\circ \\ GV &\text{ is undefined otherwise} \end{aligned} \tag{1}$$

where λ is the longitude and φ is the geodetic latitude. The angle GV should also be understood as the angle on the plane of the Universal Polar Stereographic (UPS) grid for the appropriate hemisphere at the observer's location measured clockwise from the direction parallel to the UPS Northing axis (y -axis) to the horizontal component of \mathbf{B}_m . To emphasize this, the designation GV_{UPS} may be used.

The quantity GV_{UPS} defined above is an example of a more general concept, namely grid variation or grivation. Grivation is the angle on the plane of a chosen grid coordinate system at the observer's location measured clockwise from the direction parallel to the grid's Northing axis to the horizontal component of \mathbf{B}_m . It is useful for local surveys, where location is given by grid coordinates rather than by longitude and latitude. It is dependent on the map projection used to define the grid coordinates. In general it is

$$GV_{\text{grid}} = D - C \tag{2}$$

where D is the magnetic declination and C is the “convergence-of-meridians” defined as the clockwise angle from the northward meridional arc to the grid Northing direction. Large scale military topographic mapping routinely employs the Universal Transverse Mercator (UTM) grid coordinates for the map projection of the sheet, for the definition of a grid to overprint, and for a grivation calculation as defined above. The latter could be notated GV_{UTM} .

In the new WMM subroutine library, both GV_{UPS} and GV_{UTM} are provided within certain restrictions (see the software user's guide (<http://www.ngdc.noaa.gov/geomag/WMM/soft.shtml>)).

1.1.3 RANGE OF THE MAGNETIC ELEMENTS AT THE EARTH'S SURFACE

Table 1 shows the expected range of the magnetic field elements and GV at the Earth's surface.

Table 1: Ranges of magnetic elements and GV at the Earth's surface.

| Element | Name | Alternative Name | Range at Earth's Surface | | | Positive Sense |
|---------|----------------------|---------------------|--------------------------|-------|--------|------------------|
| | | | Min | Max | Unit | |
| X | North component | Northerly intensity | -17000 | 42000 | nT | North |
| Y | East component | Easterly intensity | -18000 | 17000 | nT | East |
| Z | Down component | Vertical intensity | -67000 | 61000 | nT | Down |
| H | Horizontal intensity | | 0 | 42000 | nT | |
| F | Total intensity | Total field | 22000 | 67000 | nT | |
| I | Inclination | Dip | -90 | 90 | Degree | Down |
| D | Declination | Magnetic variation | -180 | 180 | Degree | East / Clockwise |
| GV | Grid variation | Gravitation | -180 | 180 | Degree | East / Clockwise |

1.2 RELEVANT MODEL EQUATIONS

This section describes the representation of the magnetic field in the WMM and lists the equations needed to obtain the magnetic field elements for the desired location and time from the WMM coefficients. All variables in this section adhere to the following measurement conventions: angles are in radians, lengths are in meters, magnetic intensities are in nano-Teslas (nT) and times are in years. The software may display these quantities in other units, which it will identify.

The main magnetic field \mathbf{B}_m is a potential field and therefore can be written in geocentric spherical coordinates (longitude λ , latitude φ' , radius r) as the negative spatial gradient of a scalar potential

$$\mathbf{B}_m(\lambda, \varphi', r, t) = -\nabla V(\lambda, \varphi', r, t) \quad (3)$$

This potential can be expanded in terms of spherical harmonics:

$$V(\lambda, \varphi', r, t) = a \sum_{n=1}^N \left(\frac{a}{r}\right)^{n+1} \sum_{m=0}^n (g_n^m(t) \cos(m\lambda) + h_n^m(t) \sin(m\lambda)) \check{P}_n^m(\sin \varphi') \quad (4)$$

where $N=12$ is the degree of the expansion of the WMM, a (6371200 m) is the geomagnetic reference radius, (λ, φ', r) are the longitude, latitude and radius in a spherical geocentric reference frame, and $g_n^m(t)$ and $h_n^m(t)$ are the time-dependent Gauss coefficients of degree n and order m describing the Earth's main magnetic field. For any real number μ , $\check{P}_n^m(\mu)$ are the Schmidt semi-normalized associated Legendre functions defined as:

$$\begin{aligned} \check{P}_n^m(\mu) &= \sqrt{2 \frac{(n-m)!}{(n+m)!}} P_{n,m}(\mu) \quad \text{if } m > 0 \\ \check{P}_n^m(\mu) &= P_{n,m}(\mu) \quad \text{if } m = 0 \end{aligned} \quad (5)$$

Here, the definition of $P_{n,m}(\mu)$ is commonly used in geodesy and geomagnetism (e.g., Heiskanen and Moritz, 1967, equation 1-60; Langel, 1987, equation 8). Sample functions, for geocentric latitude φ' , are:

$$\begin{aligned}
 P_{3,0}(\sin \varphi') &= \frac{1}{2}(\sin \varphi')(5 \sin^2 \varphi' - 3) \\
 P_{3,1}(\sin \varphi') &= -\frac{3}{2}(\cos \varphi')(1 - 5 \sin^2 \varphi') \\
 P_{3,2}(\sin \varphi') &= 15(\sin \varphi')(1 - \sin^2 \varphi') \\
 P_{3,3}(\sin \varphi') &= 15 \cos^3 \varphi'
 \end{aligned} \tag{6}$$

These $P_{n,m}(\mu)$ are related to the $P_n^m(\mu)$ defined in Abramowitz and Stegun (1972, Chapter 8) or Gradshteyn and Ryzhik (1994, Chapter 8.7) by $P_{n,m}(\mu) = (-1)^m P_n^m(\mu)$.

WMM2015 comprises two sets of Gauss coefficients to degree and order $N=12$. One set provides a spherical-harmonic main field model for 2015.0 in units of nT, the other set provides a predictive secular variation model for the period 2015.0 to 2020.0 in units of nT/year. The secular variation model was derived from geomagnetic data prior to 2015.0. Specifically, it represents the average of instantaneous changes of the main field at 0.1 year intervals over a year starting at 2013.6. However, this represents our best knowledge of the geomagnetic main field evolution at the time of the WMM release, and is expected to yield geomagnetic main field values within defined uncertainty parameters for the lifetime of the model.

A step by step procedure is provided below for computing the magnetic field elements at a given location and time ($\lambda, \varphi, h_{MSL}, t$), where λ and φ are the geodetic longitude and latitude, h_{MSL} is Mean Sea Level (MSL) height, and t is the time given in decimal years.

In the first step, the user provides the time, location and MSL height at which the magnetic elements are to be calculated. The MSL height is then converted to height h above the WGS 84 ellipsoid by using the geopotential model EGM96 (Lemoine et al., 1998). This is accomplished by interpolating a grid of the geoid height file with a spatial resolution of 15 arc-minutes. This stage of converting MSL height to height above the WGS84 ellipsoid has a very small effect on the resulting magnetic field values (of the order of 1 nT or less) and is unnecessary in the majority of implementations. Note that the user can also directly enter the height above the WGS84 ellipsoid into the software.

The geodetic coordinates (λ, φ, h) are then transformed into spherical geocentric coordinates (λ, φ', r) by recognizing that λ is the same in both coordinate systems, and that (φ', r) is computed from (φ, h) according to the equations:

$$\begin{aligned} p &= (R_c + h) \cos \varphi \\ z &= (R_c (1 - e^2) + h) \sin \varphi \\ r &= \sqrt{p^2 + z^2} \\ \varphi' &= \arcsin \frac{z}{r} \end{aligned} \tag{7}$$

Here, $p = \sqrt{x^2 + y^2}$, where x, y and z are the coordinates of a geocentric Cartesian coordinate system in which the positive x and z axes point in the directions of the prime meridian ($\lambda=0$) and the Earth's rotation axis, respectively. The semi-major axis A , reciprocal flattening $1/f$, eccentricity squared e^2 and radius of curvature of the prime vertical (also called normal section) R_c at the given latitude φ are given for the WGS 84 ellipsoid as

$$\begin{aligned} A &= 6378137 \text{ m} \\ \frac{1}{f} &= 298.257223563 \\ e^2 &= f(2 - f) \end{aligned} \tag{8}$$

$$R_c = \frac{A}{\sqrt{1 - e^2 \sin^2 \varphi}}$$

In the second step, the Gauss coefficients $g_n^m(t)$ and $h_n^m(t)$ are determined for the desired time t from the model coefficients $g_n^m(t_0)$, $h_n^m(t_0)$, $\dot{g}_n^m(t_0)$ and $\dot{h}_n^m(t_0)$ as

$$\begin{aligned} g_n^m(t) &= g_n^m(t_0) + (t - t_0) \dot{g}_n^m(t_0) \\ h_n^m(t) &= h_n^m(t_0) + (t - t_0) \dot{h}_n^m(t_0) \end{aligned} \quad (9)$$

where the time is given in decimal years and $t_0 = 2015.0$, the reference epoch of the model. The quantities $g_n^m(t_0)$ and $h_n^m(t_0)$ are called the main field coefficients and the quantities $\dot{g}_n^m(t_0)$ and $\dot{h}_n^m(t_0)$ are called the secular variation coefficients.

In the third step, the field vector components X' , Y' and Z' in geocentric coordinates are computed as

$$\begin{aligned} X'(\lambda, \varphi', r) &= -\frac{1}{r} \frac{\partial V}{\partial \varphi'} \\ &= -\sum_{n=1}^{12} \left(\frac{a}{r} \right)^{n+2} \sum_{m=0}^n (g_n^m(t) \cos m\lambda + h_n^m(t) \sin m\lambda) \frac{d \breve{P}_n^m(\sin \varphi')}{d \varphi'} \end{aligned} \quad (10)$$

$$\begin{aligned} Y'(\lambda, \varphi', r) &= -\frac{1}{r \cos \varphi'} \frac{\partial V}{\partial \lambda} \\ &= \frac{1}{\cos \varphi'} \sum_{n=1}^{12} \left(\frac{a}{r} \right)^{n+2} \sum_{m=0}^n m(g_n^m(t) \sin m\lambda - h_n^m(t) \cos m\lambda) \breve{P}_n^m(\sin \varphi') \end{aligned} \quad (11)$$

$$\begin{aligned}
Z'(\lambda, \varphi', r) &= \frac{\partial V}{\partial r} \\
&= -\sum_{n=1}^{12} (n+1) \left(\frac{a}{r} \right)^{n+2} \sum_{m=0}^n (g_n^m(t) \cos m\lambda + h_n^m(t) \sin m\lambda) \check{P}_n^m(\sin \varphi')
\end{aligned} \tag{12}$$

At this point, the secular variation of the field components can be computed as

$$\begin{aligned}
\dot{X}'(\lambda, \varphi', r) &= -\frac{1}{r} \frac{\partial \dot{V}}{\partial \varphi'} \\
&= -\sum_{n=1}^{12} \left(\frac{a}{r} \right)^{n+2} \sum_{m=0}^n (\dot{g}_n^m \cos m\lambda + \dot{h}_n^m \sin m\lambda) \frac{d \check{P}_n^m(\sin \varphi')}{d \varphi'}
\end{aligned} \tag{13}$$

$$\begin{aligned}
\dot{Y}'(\lambda, \varphi', r) &= -\frac{1}{r \cos \varphi'} \frac{\partial \dot{V}}{\partial \lambda} \\
&= \frac{1}{\cos \varphi'} \sum_{n=1}^{12} \left(\frac{a}{r} \right)^{n+2} \sum_{m=0}^n m (\dot{g}_n^m \sin m\lambda - \dot{h}_n^m \cos m\lambda) \check{P}_n^m(\sin \varphi')
\end{aligned} \tag{14}$$

$$\begin{aligned}
\dot{Z}'(\lambda, \varphi', r) &= \frac{\partial \dot{V}}{\partial r} \\
&= -\sum_{n=1}^{12} (n+1) \left(\frac{a}{r} \right)^{n+2} \sum_{m=0}^n (\dot{g}_n^m \cos m\lambda + \dot{h}_n^m \sin m\lambda) \check{P}_n^m(\sin \varphi')
\end{aligned} \tag{15}$$

$$\frac{d \check{P}_n^m(\sin \varphi')}{d \varphi'} = (n+1)(\tan \varphi') \check{P}_n^m(\sin \varphi') - \sqrt{(n+1)^2 - m^2} (\sec \varphi') \check{P}_{n+1}^m(\sin \varphi') \tag{16}$$

In the fourth step, the geocentric magnetic field vector components X' , Y' and Z' , are rotated into the ellipsoidal reference frame, using

$$\begin{aligned}
X &= X' \cos(\varphi' - \varphi) - Z' \sin(\varphi' - \varphi) \\
Y &= Y' \\
Z &= X' \sin(\varphi' - \varphi) + Z' \cos(\varphi' - \varphi)
\end{aligned} \tag{17}$$

Similarly, the time derivatives of the vector components, \dot{X}' , \dot{Y}' and \dot{Z}' are rotated using

$$\begin{aligned}
\dot{X} &= \dot{X}' \cos(\varphi' - \varphi) - \dot{Z}' \sin(\varphi' - \varphi) \\
\dot{Y} &= \dot{Y}' \\
\dot{Z} &= \dot{X}' \sin(\varphi' - \varphi) + \dot{Z}' \cos(\varphi' - \varphi)
\end{aligned} \tag{18}$$

In the last step, the magnetic elements H , F , I and D are computed from the orthogonal components:

$$H = \sqrt{X^2 + Y^2}, \quad F = \sqrt{H^2 + Z^2}, \quad I = \arctan(Z, H), \quad D = \arctan(Y, X) \tag{19}$$

where $\arctan(a, b)$ is $\tan^{-1}(a/b)$, taking into account the angular quadrant, avoiding a division by zero, and resulting in a declination in the range of $-\pi$ to π and an inclination in the range of $-\pi/2$ to $\pi/2$. These angles in radians are then output by the WMM software in degrees.

The secular variation of these elements is computed using

$$\begin{aligned}
\dot{H} &= \frac{X \cdot \dot{X} + Y \cdot \dot{Y}}{H} \\
\dot{F} &= \frac{X \cdot \dot{X} + Y \cdot \dot{Y} + Z \cdot \dot{Z}}{F} \\
\dot{I} &= \frac{H \cdot \dot{Z} - Z \cdot \dot{H}}{F^2} \\
\dot{D} &= \frac{X \cdot \dot{Y} - Y \cdot \dot{X}}{H^2} \\
G\dot{V} &= \dot{D}
\end{aligned} \tag{20}$$

where \dot{I} , \dot{D} and $G\dot{V}$ are given in radians per year. The WMM software then outputs these angles in arc-minutes per year or decimal degrees per year.

1.3 THE WMM2015 COEFFICIENTS

The model coefficients, also referred to as Gauss coefficients, are listed in Table 2. These coefficients can be used to compute values for the field elements and their annual rates of change at any location near the surface of the Earth, and at any date between 2015.0 and 2020.0.

Table 2: Final coefficients for WMM2015. Units are nT for the main field, and nT per year for the secular variation. The index n is the degree and m is the order. Since $h_n^m(t_0)$ and $\dot{h}_n^m(t_0)$ are not defined for $m=0$, the corresponding fields are left blank.

| n | m | $g_n^m(t_0)$ | $h_n^m(t_0)$ | $\dot{g}_n^m(t_0)$ | $\dot{h}_n^m(t_0)$ |
|-----|-----|--------------|--------------|--------------------|--------------------|
| 1 | 0 | -29438.5 | | 10.7 | |
| 1 | 1 | -1501.1 | 4796.2 | 17.9 | -26.8 |
| 2 | 0 | -2445.3 | | -8.6 | 0.0 |
| 2 | 1 | 3012.5 | -2845.6 | -3.3 | -27.1 |
| 2 | 2 | 1676.6 | -642.0 | 2.4 | -13.3 |
| 3 | 0 | 1351.1 | | 3.1 | |
| 3 | 1 | -2352.3 | -115.3 | -6.2 | 8.4 |
| 3 | 2 | 1225.6 | 245.0 | -0.4 | -0.4 |
| 3 | 3 | 581.9 | -538.3 | -10.4 | 2.3 |
| 4 | 0 | 907.2 | | -0.4 | |
| 4 | 1 | 813.7 | 283.4 | 0.8 | -0.6 |
| 4 | 2 | 120.3 | -188.6 | -9.2 | 5.3 |
| 4 | 3 | -335.0 | 180.9 | 4.0 | 3.0 |
| 4 | 4 | 70.3 | -329.5 | -4.2 | -5.3 |
| 5 | 0 | -232.6 | | -0.2 | |
| 5 | 1 | 360.1 | 47.4 | 0.1 | 0.4 |
| 5 | 2 | 192.4 | 196.9 | -1.4 | 1.6 |
| 5 | 3 | -141.0 | -119.4 | 0.0 | -1.1 |
| 5 | 4 | -157.4 | 16.1 | 1.3 | 3.3 |
| 5 | 5 | 4.3 | 100.1 | 3.8 | 0.1 |
| 6 | 0 | 69.5 | | -0.5 | |
| 6 | 1 | 67.4 | -20.7 | -0.2 | 0.0 |
| 6 | 2 | 72.8 | 33.2 | -0.6 | -2.2 |
| 6 | 3 | -129.8 | 58.8 | 2.4 | -0.7 |
| 6 | 4 | -29.0 | -66.5 | -1.1 | 0.1 |
| 6 | 5 | 13.2 | 7.3 | 0.3 | 1.0 |
| 6 | 6 | -70.9 | 62.5 | 1.5 | 1.3 |
| 7 | 0 | 81.6 | | 0.2 | |
| 7 | 1 | -76.1 | -54.1 | -0.2 | 0.7 |
| 7 | 2 | -6.8 | -19.4 | -0.4 | 0.5 |
| 7 | 3 | 51.9 | 5.6 | 1.3 | -0.2 |
| 7 | 4 | 15.0 | 24.4 | 0.2 | -0.1 |
| 7 | 5 | 9.3 | 3.3 | -0.4 | -0.7 |
| 7 | 6 | -2.8 | -27.5 | -0.9 | 0.1 |
| 7 | 7 | 6.7 | -2.3 | 0.3 | 0.1 |
| 8 | 0 | 24.0 | | 0.0 | |
| 8 | 1 | 8.6 | 10.2 | 0.1 | -0.3 |
| 8 | 2 | -16.9 | -18.1 | -0.5 | 0.3 |
| 8 | 3 | -3.2 | 13.2 | 0.5 | 0.3 |
| 8 | 4 | -20.6 | -14.6 | -0.2 | 0.6 |
| 8 | 5 | 13.3 | 16.2 | 0.4 | -0.1 |
| 8 | 6 | 11.7 | 5.7 | 0.2 | -0.2 |
| 8 | 7 | -16.0 | -9.1 | -0.4 | 0.3 |
| 8 | 8 | -2.0 | 2.2 | 0.3 | 0.0 |
| 9 | 0 | 5.4 | | 0.0 | |

| n | m | $g_n^m(t_0)$ | $h_n^m(t_0)$ | $\dot{g}_n^m(t_0)$ | $\dot{h}_n^m(t_0)$ |
|-----|-----|--------------|--------------|--------------------|--------------------|
| 9 | 1 | 8.8 | -21.6 | -0.1 | -0.2 |
| 9 | 2 | 3.1 | 10.8 | -0.1 | -0.1 |
| 9 | 3 | -3.1 | 11.7 | 0.4 | -0.2 |
| 9 | 4 | 0.6 | -6.8 | -0.5 | 0.1 |
| 9 | 5 | -13.3 | -6.9 | -0.2 | 0.1 |
| 9 | 6 | -0.1 | 7.8 | 0.1 | 0.0 |
| 9 | 7 | 8.7 | 1.0 | 0.0 | -0.2 |
| 9 | 8 | -9.1 | -3.9 | -0.2 | 0.4 |
| 9 | 9 | -10.5 | 8.5 | -0.1 | 0.3 |
| 10 | 0 | -1.9 | | 0.0 | |
| 10 | 1 | -6.5 | 3.3 | 0.0 | 0.1 |
| 10 | 2 | 0.2 | -0.3 | -0.1 | -0.1 |
| 10 | 3 | 0.6 | 4.6 | 0.3 | 0.0 |
| 10 | 4 | -0.6 | 4.4 | -0.1 | 0.0 |
| 10 | 5 | 1.7 | -7.9 | -0.1 | -0.2 |
| 10 | 6 | -0.7 | -0.6 | -0.1 | 0.1 |
| 10 | 7 | 2.1 | -4.1 | 0.0 | -0.1 |
| 10 | 8 | 2.3 | -2.8 | -0.2 | -0.2 |
| 10 | 9 | -1.8 | -1.1 | -0.1 | 0.1 |
| 10 | 10 | -3.6 | -8.7 | -0.2 | -0.1 |
| 11 | 0 | 3.1 | | 0.0 | |
| 11 | 1 | -1.5 | -0.1 | 0.0 | 0.0 |
| 11 | 2 | -2.3 | 2.1 | -0.1 | 0.1 |
| 11 | 3 | 2.1 | -0.7 | 0.1 | 0.0 |
| 11 | 4 | -0.9 | -1.1 | 0.0 | 0.1 |
| 11 | 5 | 0.6 | 0.7 | 0.0 | 0.0 |
| 11 | 6 | -0.7 | -0.2 | 0.0 | 0.0 |
| 11 | 7 | 0.2 | -2.1 | 0.0 | 0.1 |
| 11 | 8 | 1.7 | -1.5 | 0.0 | 0.0 |
| 11 | 9 | -0.2 | -2.5 | 0.0 | -0.1 |
| 11 | 10 | 0.4 | -2.0 | -0.1 | 0.0 |
| 11 | 11 | 3.5 | -2.3 | -0.1 | -0.1 |
| 12 | 0 | -2.0 | | 0.1 | |
| 12 | 1 | -0.3 | -1.0 | 0.0 | 0.0 |
| 12 | 2 | 0.4 | 0.5 | 0.0 | 0.0 |
| 12 | 3 | 1.3 | 1.8 | 0.1 | -0.1 |
| 12 | 4 | -0.9 | -2.2 | -0.1 | 0.0 |
| 12 | 5 | 0.9 | 0.3 | 0.0 | 0.0 |
| 12 | 6 | 0.1 | 0.7 | 0.1 | 0.0 |
| 12 | 7 | 0.5 | -0.1 | 0.0 | 0.0 |
| 12 | 8 | -0.4 | 0.3 | 0.0 | 0.0 |
| 12 | 9 | -0.4 | 0.2 | 0.0 | 0.0 |
| 12 | 10 | 0.2 | -0.9 | 0.0 | 0.0 |
| 12 | 11 | -0.9 | -0.2 | 0.0 | 0.0 |
| 12 | 12 | 0.0 | 0.7 | 0.0 | 0.0 |

1.4 SINGULARITIES AT THE GEOGRAPHIC POLES

The World Magnetic Model has singularities at the North and South geographic poles. This is a mathematical issue, not a geophysical phenomenon, stemming from the ambiguity of longitude at a Pole and at any altitude over a Pole. Related to this, the North-East-Down (NED) frame of unit vectors to which the X', Y', Z' quantities are referred is defined everywhere except at or over a Pole. This section extends these concepts. The North Pole is discussed in the following, with implications for the South Pole.

To most comprehensively appreciate the model equations, let the arbitrariness of the North Pole's longitude disambiguate the North Pole's NED frame. In other words, if the Pole is assigned a longitude of λ , then the NED frame at the Pole is to be oriented so that the unit vector "N" of NED has the same direction as for a point approaching the pole along the λ -meridian, the unit vector "D" is directed downward, and the unit vector "E" is directed so that NED is right-handed. This is equivalent to requiring the NED frame at longitude λ and latitude 90° to be the limit of NED frames as the latitude approaches 90° and the longitude and altitude remain fixed.

On 1 January 2015, directly above the North (resp. South) Pole at 6,371,200 meters from the Earth's center, the magnetic field vector lies in the half-plane of the 173.47°W (resp. 149.87°W) meridian. If the Pole is assigned $\lambda = 0^\circ$, the components X', Y', Z' (also the components X, Y, Z) are 1876.3 nT, -214.8 nT, and 56268.5 nT respectively at the North Pole, 14324.8 nT, -8315.9 nT and -51979.9 nT respectively at the South Pole. A change in the longitude assigned to the Pole is equivalent to a rotation of the NED frame about the polar axis.

The model equations of [section 1.2](#) support the above pole calculation and others like it provided the equation for Y' is extended by continuity as follows to ameliorate the factor $\cos(\varphi')$ in the denominator. As φ' approaches 90° , the function $(\check{P}_n^m(\sin \varphi'))/\cos \varphi'$ approaches zero if $m > 1$. It approaches certain non-zero finite limits if $m = 1$. And it multiplies a zero coefficient and can be ignored if $m = 0$. For $m = 1$ and $1 \leq n \leq 12$ respectively, the limits are:

| 1 | 2 | 3 | 4 | 5 | 6 | 7 | 8 | 9 | 10 | 11 | 12 |
|---|------------|------------|-------------|-------------|-------------|-------------|---|-------------|-------------|-------------|-------------|
| 1 | $\sqrt{3}$ | $\sqrt{6}$ | $\sqrt{10}$ | $\sqrt{15}$ | $\sqrt{21}$ | $2\sqrt{7}$ | 6 | $3\sqrt{5}$ | $\sqrt{55}$ | $\sqrt{66}$ | $\sqrt{78}$ |

1.5 MODEL EQUATIONS NUMERICAL EXAMPLE

A software implementation of the relevant model equations is provided with this report. Most software developers should find the C programs and/or C subroutines to be sufficient for their purposes, after adaptations are made to their own software structures.

To aid software developers who need to re-implement the model equations for special requirements, Tables 3a to 3c provide a numerical example showing the intermediate calculations of [section 1.2](#). For the purpose of verifying the correct implementation of the equations, the tables display many more digits than are warranted by the accuracy of the WMM.

The output in Table 3c includes gravitation calculations for four grid systems, whether or not the grid system is commonly used in that part of the world. This is helpful for the purposes of verifying correct implementation of the mathematics in the software, and if not used the unwanted grid systems may be ignored.

Table 3a: High-precision numerical example, given values for time, altitude, latitude and longitude.

| | | |
|------------------------|----------------|-----|
| Time | 2017.5000 0000 | yr |
| Height-above-Ellipsoid | 100.0000 0000 | km |
| Latitude | -80.0000 0000 | deg |
| Longitude | 240.0000 0000 | deg |

Table 3b: High-precision numerical example, computations of the magnetic field elements

| | | | |
|----|------------|----------------------|--------|
| 1 | lambda | 4.18879 02048 | rad |
| 2 | phi | -1.39626 34016 | rad |
| 3 | h | 1 00000.00000 00000 | m |
| 4 | t | 2017.50000 00000 | yr |
| 5 | phi-prime | -1.39512 89589 | rad |
| 6 | r | 64 57402.34844 73705 | m |
| 7 | g(1,0,t) | -29411.75000 00000 | nT |
| 8 | g(1,1,t) | -1456.35000 00000 | nT |
| 9 | g(2,0,t) | -2466.80000 00000 | nT |
| 10 | g(2,1,t) | 3004.25000 00000 | nT |
| 11 | g(2,2,t) | 1682.60000 00000 | nT |
| 12 | h(1,0,t) | 0.00000 00000 | nT |
| 13 | h(1,1,t) | 4729.20000 00000 | nT |
| 14 | h(2,0,t) | 0.00000 00000 | nT |
| 15 | h(2,1,t) | -2913.35000 00000 | nT |
| 16 | h(2,2,t) | -675.25000 00000 | nT |
| 17 | Xprime | 5626.60683 98092 | nT |
| 18 | Yprime | 14808.84920 23104 | nT |
| 19 | Zprime | -50169.42871 02381 | nT |
| 20 | Xprime-dot | 28.26278 12813 | nT/yr |
| 21 | Yprime-dot | 6.94115 21726 | nT/yr |
| 22 | Zprime-dot | 86.21155 70931 | nT/yr |
| 23 | X | 5683.51754 95763 | nT |
| 24 | Y | 14808.84920 23104 | nT |
| 25 | Z | -50163.01336 54779 | nT |
| 26 | Xdot | 28.16496 10434 | nT/yr |
| 27 | Ydot | 6.94115 21726 | nT/yr |
| 28 | Zdot | 86.24356 41169 | nT/yr |
| 29 | F | 52611.14232 11683 | nT |
| 30 | H | 15862.04231 59539 | nT |
| 31 | D | 1.20433 99870 | rad |
| 32 | I | -1.26453 51837 | rad |
| 33 | Fdot | -77.23402 97896 | nT/yr |
| 34 | Hdot | 16.57204 79716 | nT/yr |
| 35 | Ddot | -0.00150 09297 | rad/yr |
| 36 | Idot | 0.00079 45653 | rad/yr |

Table 3c: High-precision numerical example, grivation calculations. Angles are in degrees.

| Grid System | UPS | UPS | UTM | UTM |
|----------------|-----------------|-----------------|---------------|---------------|
| Grid zone | North | South | 10 | 11 |
| TrueN-to-GridN | 240.00000 00000 | -240.0000000000 | -2.9545046801 | 2.9545046801 |
| GridN-to-MagN | -170.9964016460 | 309.0035983540 | 71.9581030341 | 66.0490936739 |
| TrueN-to-MagN | 69.0035983540 | 69.0035983540 | 69.0035983540 | 69.0035983540 |

1.6 SUPERSESSION OF THE MODELS

WMM2015 supersedes WMM2010 (Maus et al., 2010) and should replace it in navigation and other systems. Also included with the model is software for computing the magnetic field components X , Y , Z , H , F , I , D and auxiliary angle GV as defined above, as well as the model uncertainty on each component (see [section 3](#)). WMM2015 is to be used from 1 January 2015, to 31 December 2019. In late December of 2019, barring unforeseen circumstances, the U.S. and U.K. agencies will replace WMM2015 with a new degree and order 12 main field model, and a new degree and order 12 predictive secular-variation model.

1.7 POLICY ON ALTERNATE SOFTWARE FOR THE U.S. DEPARTMENT OF DEFENSE

The WMM2015 product release includes several software items by which the WMM2015 model may be computed and/or its subroutines incorporated into larger U.S. Department of Defense (DoD) systems. It is hoped that the software provided is useful for most occasions of DoD systems procurement and development.

If there are special requirements, and the model equations must be implemented anew or a separate interpolation algorithm invented, the software developer may use the label WMM2015 for the resulting product provided the resulting software agrees with the relevant model equations within the following tolerances:

Between latitudes 89.992°S and 89.992°N,

Quantities in nanoTeslas shall be correct to within 0.1 nT

Quantities in nanoTeslas/year shall be correct to within 0.1 nT/year

(see [section 1.4](#) for the computation problems exactly at the Poles).

This policy is designed to promote interoperability and to track departures from consistency when necessary. It permits systems developers to display as many digits as needed and not display unneeded digits. It also allows that the computations be taken to less than full double precision accuracy and the software retain the WMM2015 label. This policy refers to the allowed computational error in the software, not to the accuracy or limitations of the science or the geomagnetic model.

If there are special requirements, and the model equations are implemented anew or separate interpolation algorithm invented, and accuracy is sacrificed for speed of computation such that the above tolerances are not met, the label WMM2015 may not be applied to the resulting product. In this situation, the DoD entity or contractor is urged to apply to NGA or NGDC acting on behalf of NGA, for the label to adopt to indicate that this is a modification of WMM2015.

1.8 MAGNETIC POLES AND GEOMAGNETIC COORDINATE SYSTEMS

There are different ways of defining magnetic poles. The most common understanding is that they are the positions on the Earth's surface where the geomagnetic field is perpendicular to the ellipsoid, that is, vertical (assuming the deflection of the vertical is negligible). These positions are called *dip poles*, and the north and south dip poles do not have to be (and are not now) antipodal. In principle the dip poles can be found by experiment, conducting a magnetic survey to determine where the field is vertical. In practice the geomagnetic field is vertical on oval-shaped loci traced on a daily basis, with considerable variation from one day to the next.

Other magnetic pole definitions originate from models of the geomagnetic field (Table 4). The WMM representation of the field includes a magnetic dipole at the center of the Earth. This dipole defines an axis that intersects the Earth's surface at two antipodal points. These points are called *geomagnetic poles*. The geomagnetic poles, otherwise known as the dipole poles, can be

computed from the first three Gauss coefficients of the WMM. Based on the WMM2015 coefficients for 2015.0 the geomagnetic north pole is at 72.62°W longitude and 80.31°N geocentric latitude (80.37°N geodetic latitude), and the geomagnetic south pole is at 107.38°E longitude and 80.31°S geocentric latitude (80.37°S geodetic latitude). The axis of the dipole is currently inclined at 9.69° to the Earth's rotation axis. The same dipole is the basis for the simple geomagnetic coordinate system of geomagnetic latitude and longitude (see [section 4](#), Geomagnetic longitude and latitude in Mercator projection). The geomagnetic equator is at geomagnetic latitude 0°.

The WMM can also be used to calculate dip pole positions. These *model dip poles* are computed from all the Gauss coefficients using an iterative method. In 2015.0 the north dip pole computed from WMM2015 is located at longitude 159.18°W and geodetic latitude 86.27°N and the south dip pole at longitude 136.59°E and geodetic latitude 64.26°S.

Scientists, map makers and polar explorers have an interest in the dip and geomagnetic pole locations. Although geomagnetic pole observations cannot be made to indicate their positions, these poles are arguably of greater significance than the dip poles. Auroral ovals, which are approximately 5° latitude bands where aurorae are likely to be seen, are approximately centered on the geomagnetic poles. They are usually displaced slightly to the night-side of the geomagnetic poles and greatly vary in size: bands of greatest activity occur between 15° and 25° from the geomagnetic poles.

A further concept is that of *eccentric dipole*, or off-centered dipole. The location of the center of the eccentric dipole (sometimes known as magnetic center), computed using the first eight Gauss coefficients for 2015.0 (Langel, 1987, p. 386), is at $(r, \varphi', \lambda) = (577 \text{ kilometers}, 22.57^\circ\text{N}, 138.66^\circ\text{E})$. The axis of the eccentric dipole is parallel to the axis of the (centered) dipole field.

Table 4: Computed pole positions based on the WMM2015.

| | Date | North | South |
|--------------------------|--------|--|---|
| Geomagnetic Poles | 2015.0 | 72.62° W 80.31° N (geocentric) 80.37° S (geodetic) | 107.38° E 80.31° S (geocentric) 80.37° S (geodetic) |
| Model Dip Poles | 2015.0 | 159.18° W 86.27° N | 136.59° E 64.26° S |
| Eccentric Dipole | 2015.0 | $r = 577 \text{ km}$; $\varphi' = 22.57^\circ\text{N}$; $\lambda = 138.66^\circ\text{E}$ | |

1.9 DESCRIPTION OF CHARTS

Charts of the magnetic elements and their annual rates of change, and of grid variation, are available in PDF from the NOAA WMM web site (<http://www.ngdc.noaa.gov/geomag/WMM>), and replicated in [section 4](#). They are also available at the BGS WMM web site (<http://www.geomag.bgs.ac.uk/research/modelling/WorldMagneticModel.html>).

The following charts are available:

- Main field magnetic elements X , Y , Z , H , F , I and D on the Mercator projection between latitudes 70°S and 70°N.
- Main field magnetic elements X , Y , Z , H , F , I and D on the north and south polar stereographic projection for latitudes northward of 55°N and southward of 55°S.
- Secular variation of X , Y , Z , H , F , I and D on the Mercator projection between latitudes 70°S and 70°N.
- Secular variation of X , Y , Z , H , F , I and D on the north and south polar stereographic projection for northward of 55°N and southward of 55°S.
- Grid variation (GV) and its annual change on the north and south polar stereographic projection for northward of 55°N and southward of 55°S.
- Geomagnetic latitude and longitude on the Mercator projection between latitudes 70°S and 70°N.

1.10 TEST VALUES

To verify the correctness of a coefficient update or new software installation, Table 5 provides test values to validate software output. The WMM coefficient file, software that executes the WMM, and several derived products are distributed by NOAA/NGDC and BGS both online and offline on behalf of NGA and DGC.

Table 5: WMM2015 test values. The computation was carried out with double precision arithmetic. Single precision arithmetic can cause differences of up to 0.1 nT. Heights are with respect to the WGS 84 Ellipsoid. Grid Variation is with respect to the Grid North of the Universal Polar Stereographic Projection.

| Date | Height (km) | Lat (deg) | Lon (deg) | X (nT) | Y (nT) | Z (nT) | H (nT) | F (nT) | I (deg) | D (deg) | GV (deg) |
|--------|-------------|-----------|-----------|--------------|--------------|--------------|--------------|--------------|---------------|---------------|----------|
| 2015.0 | 0 | 80 | 0 | 6627.1 | -445.9 | 54432.3 | 6642.1 | 54836.0 | 83.04 | -3.85 | -3.85 |
| 2015.0 | 0 | 0 | 120 | 39518.2 | 392.9 | -11252.4 | 39520.2 | 41090.9 | -15.89 | 0.57 | 0.57 |
| 2015.0 | 0 | -80 | 240 | 5797.3 | 15761.1 | -52919.1 | 16793.5 | 55519.8 | -72.39 | 69.81 | 309.81 |
| 2015.0 | 100 | 80 | 0 | 6314.3 | -471.6 | 52269.8 | 6331.9 | 52652.0 | 83.09 | -4.27 | -4.27 |
| 2015.0 | 100 | 0 | 120 | 37535.6 | 364.4 | -10773.4 | 37537.3 | 39052.7 | -16.01 | 0.56 | 0.56 |
| 2015.0 | 100 | -80 | 240 | 5613.1 | 14791.5 | -50378.6 | 15820.7 | 52804.4 | -72.57 | 69.22 | 309.22 |
| 2017.5 | 0 | 80 | 0 | 6599.4 | -317.1 | 54459.2 | 6607.0 | 54858.5 | 83.08 | -2.75 | -2.75 |
| 2017.5 | 0 | 0 | 120 | 39571.4 | 222.5 | -11030.1 | 39572.0 | 41080.5 | -15.57 | 0.32 | 0.32 |
| 2017.5 | 0 | -80 | 240 | 5873.8 | 15781.4 | -52687.9 | 16839.1 | 55313.4 | -72.28 | 69.58 | 309.58 |
| 2017.5 | 100 | 80 | 0 | 6290.5 | -348.5 | 52292.7 | 6300.1 | 52670.9 | 83.13 | -3.17 | -3.17 |
| 2017.5 | 100 | 0 | 120 | 37585.5 | 209.5 | -10564.2 | 37586.1 | 39042.5 | -15.70 | 0.32 | 0.32 |
| 2017.5 | 100 | -80 | 240 | 5683.5 | 14808.8 | -50163.0 | 15862.0 | 52611.1 | -72.45 | 69.00 | 309.00 |
| Date | Height (km) | Lat (deg) | Lon (deg) | Xdot (nT/yr) | Ydot (nT/yr) | Zdot (nT/yr) | Hdot (nT/yr) | Fdot (nT/yr) | Idot (deg/yr) | Ddot (deg/yr) | |
| 2015.0 | 0 | 80 | 0 | -11.1 | 51.5 | 10.8 | -14.5 | 8.9 | 0.02 | 0.44 | |
| 2015.0 | 0 | 0 | 120 | 21.3 | -68.2 | 88.9 | 20.6 | -4.5 | 0.13 | -0.10 | |
| 2015.0 | 0 | -80 | 240 | 30.6 | 8.1 | 92.4 | 18.2 | -82.6 | 0.05 | -0.09 | |
| 2015.0 | 100 | 80 | 0 | -9.5 | 49.2 | 9.1 | -13.2 | 7.5 | 0.02 | 0.44 | |
| 2015.0 | 100 | 0 | 120 | 20.0 | -61.9 | 83.7 | 19.4 | -4.4 | 0.13 | -0.09 | |
| 2015.0 | 100 | -80 | 240 | 28.2 | 6.9 | 86.2 | 16.5 | -77.3 | 0.05 | -0.09 | |
| 2017.5 | 0 | 80 | 0 | -11.1 | 51.5 | 10.8 | -13.5 | 9.1 | 0.02 | 0.44 | |
| 2017.5 | 0 | 0 | 120 | 21.3 | -68.2 | 88.9 | 20.9 | -3.8 | 0.13 | -0.10 | |
| 2017.5 | 0 | -80 | 240 | 30.6 | 8.1 | 92.4 | 18.3 | -82.5 | 0.05 | -0.09 | |
| 2017.5 | 100 | 80 | 0 | -9.5 | 49.2 | 9.1 | -12.2 | 7.6 | 0.01 | 0.44 | |
| 2017.5 | 100 | 0 | 120 | 20.0 | -61.9 | 83.7 | 19.6 | -3.7 | 0.13 | -0.09 | |
| 2017.5 | 100 | -80 | 240 | 28.2 | 6.9 | 86.2 | 16.6 | -77.2 | 0.05 | -0.09 | |

2. CONSTRUCTION OF THE MODEL

2.1 BACKGROUND ON THE GEOMAGNETIC FIELD

The Earth's magnetic field (\mathbf{B}) is a vector quantity varying in space (r) and time (t). The field, as measured by a magnetic sensor on or above the Earth's surface, is actually a composite of several magnetic field contributions, generated by a variety of sources. These fields are superimposed and the sources and fields interact through inductive processes with each other. The most important of these geomagnetic sources are:

- Core field, \mathbf{B}_{core} , generated in Earth's conducting, fluid outer core;
- Crustal field, $\mathbf{B}_{\text{crust}}$, from Earth's crust/upper mantle;
- Combined disturbance field, $\mathbf{B}_{\text{disturbance}}$, from electrical currents flowing in the upper atmosphere and magnetosphere, which also induce electrical currents in the sea and the ground

The observed magnetic field is a sum of contributions:

$$\mathbf{B}(r, t) = \mathbf{B}_{\text{core}}(r, t) + \mathbf{B}_{\text{crust}}(r) + \mathbf{B}_{\text{disturbance}}(r, t) \quad (21)$$

\mathbf{B}_{core} dominates the field, accounting for over 95% of the field strength at the Earth's surface. *Secular variation* is the slow change in time of \mathbf{B}_{core} . The field arising from magnetized crustal rocks, $\mathbf{B}_{\text{crust}}$, varies spatially, but is nearly constant for the time-scales considered here. In most locations $\mathbf{B}_{\text{crust}}$ is much smaller in magnitude than \mathbf{B}_{core} but can have significant local impact on magnetic compass devices. The field arising from currents flowing in the ionosphere and magnetosphere and their resultant induced currents in the Earth's mantle and crust, $\mathbf{B}_{\text{disturbance}}$, varies both with location and time.

$\mathbf{B}_{\text{crust}}$ has spatial variations on the order of meters to thousands of kilometers and cannot be fully modeled with low degree spherical harmonic models. Therefore, the WMM does not include contributions from the crust except for those of very long wavelength. $\mathbf{B}_{\text{crust}}$ is usually smaller at sea than on land, and decreases with increasing altitude (like the core field, but much more rapidly as its sources are near the Earth's surface). The rock magnetization resulting in $\mathbf{B}_{\text{crust}}$ may be either induced by the core field or remnant, or by a combination of both.

Figure 2 shows the various current systems flowing in the magnetosphere. The disturbance field can vary regularly, with fundamental periods of one day and one year, as well as irregularly on time scales of seconds to days. The regular variations are both diurnal and annual, and are essentially generated by the daylit atmosphere at altitudes of 100-130 kilometers, ionized by the Sun's radiation and, moved in the Earth's magnetic field by winds and tides, thus producing the necessary conditions (motion of a conductor in a magnetic field) for a dynamo to operate. Further daily and annual variations are caused by the rotation of the Earth in the magnetospheric field, which is approximately fixed in orientation relative to the Sun. The irregular variations in the disturbance field are due to magnetic storms and sub-storms. Magnetic storms generally have three phases: an initial phase, often with a sudden commencement and increased horizontal field at mid-latitudes; a main phase; and a recovery phase. The main phase involves an intensification of the ring current (Figure 2) from the plasma sheet.

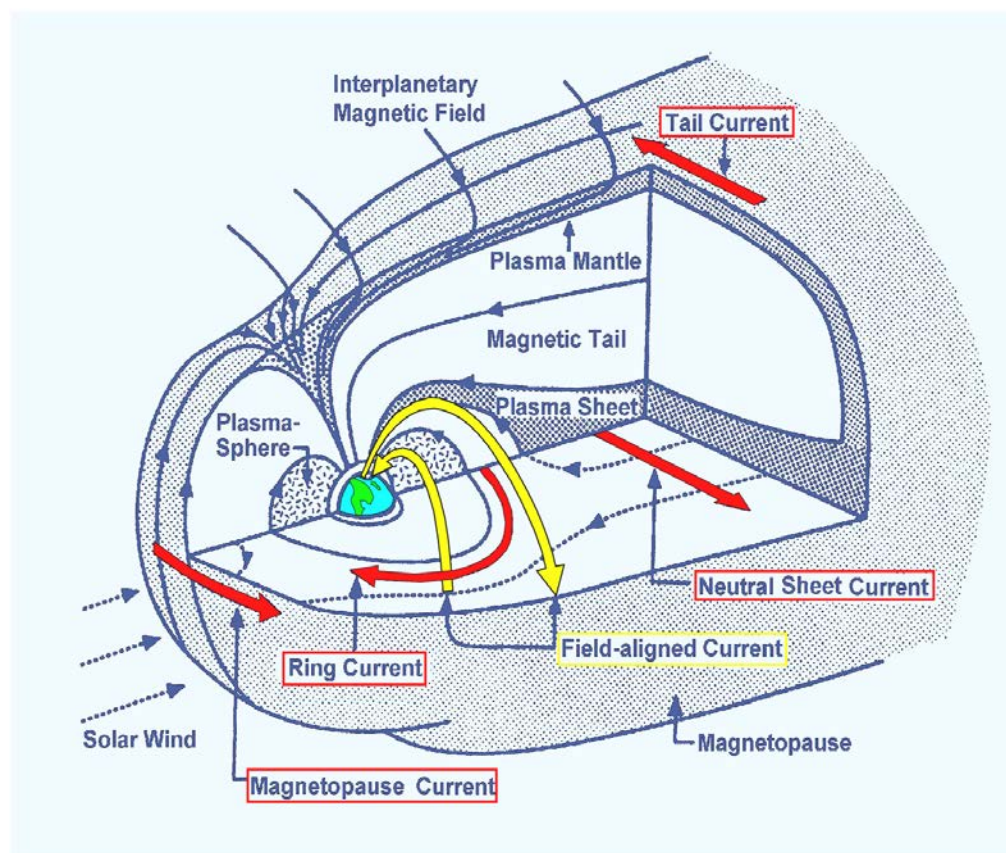


Figure 2: Current systems of the magnetosphere

During the recovery phase the ring current returns to normal over a number of days and associated sub-storms subside. Magnetic storm and sub-storm effects are generally more severe at high geomagnetic latitudes where the ionized region of the upper atmosphere (i.e., the ionosphere) is coupled to the magnetosphere by field-aligned currents. They are therefore

strongly influenced by the interplanetary magnetic field and current systems in the magnetotail. Both the regular and irregular disturbance field variations are modulated by season and the solar magnetic activity cycle. The primary disturbance field is often known as the external field, as its main sources, the ionosphere and magnetosphere, are external to the surface of the Earth where geomagnetic measurements have been traditionally observed. However, this term can be confusing when using satellite data, as the ionospheric dynamo region (100-130 kilometers) is below satellite altitude and therefore effectively internal to the orbital region. For further information about the crustal and disturbance fields, and general information about geomagnetism, see Merrill et al. (1996) and Parkinson (1983).

2.2 DATA ACQUISITION AND QUALITY CONTROL

To create an accurate magnetic field model, it is necessary to have vector component measurements with good global coverage and low noise levels. The three satellites of the European Swarm mission, launched in November 2013, are presently the most suitable global magnetic field observing system. Over the past five years, measurements of the total intensity of the magnetic field were provided by the Danish Ørsted satellite until mid-2013, with vector component measurements from the German CHAMP satellite until September 2010. Ground observatory hourly mean data are also available. Although poorer in spatial coverage, the observatory data can provide valuable constraints on the time variations of the geomagnetic field.

2.2.1 SATELLITE DATA

The principal characteristic of satellite data is global coverage using consistent instrumentation collected within a relatively short time span. The inclination of the orbit (the angle between the plane containing the satellite's path and the Earth's equatorial plane) determines the latitudinal extent of the data coverage: an inclination of 90° provides 100% coverage, an inclination of slightly less or slightly more than 90° results in gaps with no data for small regions around the geographic poles. Another important characteristic of satellite data is that localized, small-scale crustal magnetization and electromagnetic induction effects close to the Earth surface are strongly attenuated at satellite altitude, resulting in a cleaner magnetic environment for measuring the main field.

The Swarm, Ørsted and CHAMP satellites slowly drift in local time (details below) with the Earth rotating beneath them. Thus, they provide a crude picture of the entire Earth within 24

hours. During this time each satellite completes about 15 orbits, with a longitudinal spacing of around 24 degrees. Swarm, Ørsted and CHAMP data were used in the production of the WMM2015.

2.2.1.1 SWARM

Swarm

(http://www.esa.int/Our_Activities/Observing_the_Earth/The_Living_Planet_Programme/Earth_Explorers/Swarm) is a European Space Agency (ESA) mission designed for studying all aspects of the Earth's magnetic field. Swarm is composed of three satellites, two of which fly in a constellation at a lower altitude while the third flies higher and is not synchronized with the lower pair (Friis-Christensen et al., 2006). The Swarm satellites were built by Astrium and launched on 22 November 2013 from Plesetsk in Russia on a Rockot launcher into a low Earth orbit. The mission nominal duration is four years.

SATELLITE AND ORBIT

Swarm is composed of three satellites (A, B, C) which all fly in near-polar orbits. The lower pair (A and C) have inclinations of 87.4° and altitudes of about 470 km in late 2014, while the higher satellite (B) has an inclination of about 88° and an altitude of about 520 km. The satellites complete an orbit in approximately 90 minutes at a speed of about 8 km/s. Each satellite weighed 468 kg at launch and is just over 9 m in length with the boom deployed.

MAGNETOMETERS

Each Swarm satellite carries a Vector Field Magnetometer (VFM) mid-boom (Figure 3), built by the Danish Technical University. The VFMs are tri-axis fluxgate magnetometers sampling the field at 50 Hz. Once calibrated, they have an accuracy better than 1 nT. Additionally, there is an Absolute Scalar Magnetometer (ASM) at the tip of the boom used to perform an absolute calibration of the vector instruments. Each ASM has a redundant sensor. These were built by the French Atomic Energy Commission - Laboratoire d'Electronique de Technologie et d'Instrumentation (CEA-Leti), under a contract with the French National Center for Space Studies (CNES). The scalar magnetometers are optically-pumped metastable helium-4 magnetometers, sampling the field at 1 Hz in nominal mode, and at 250 Hz in a so-called "burst" mode. They have a resolution of 0.1 nT and an absolute accuracy better than 0.3 nT.

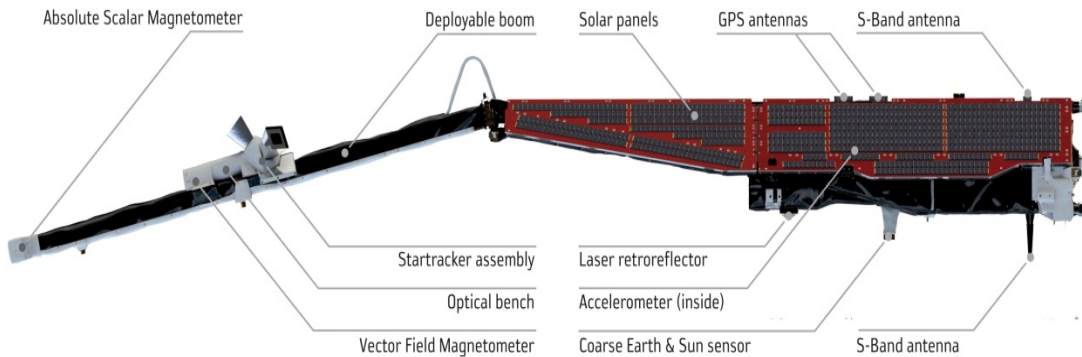


Figure 3: Swarm instruments. On each satellite, the scalar magnetometer is located at the top of the boom. The vector fluxgate magnetometer is located mid-boom, about 1.6 m from them, and is co-mounted with the star imagers.

STAR IMAGERS

A star imager, developed and supplied by the Danish Technical University, provides satellite attitude control. An ultra-stable optical bench connects the star imager and the vector magnetometer. Attitude uncertainty is the largest source of error in satellite vector magnetic data. Star imagers are often blinded by the sun or moon and provide unreliable attitude with regard to rotations about their direction of vision (bore sight). For this reason, Swarm is equipped with a triple-head star imager, while earlier magnetic satellites were equipped with single-head (Ørsted) or dual-head (CHAMP) star imagers.

GLOBAL POSITIONING SYSTEM (GPS) RECEIVERS

Each Swarm satellite is equipped with a dual frequency GPS receiver providing precise positioning and time-tagging of the data acquired by the instruments. Precise positioning is also used for spacecraft control. The GPS receivers were provided by ESA.

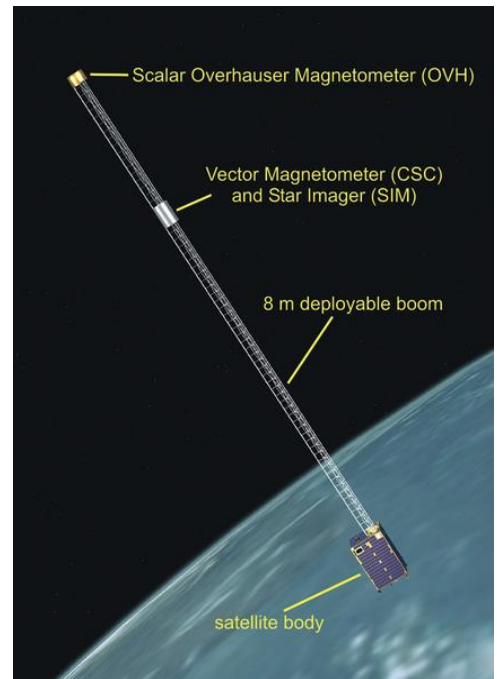
DATA PRODUCTS

Swarm's standard data products are labeled from level-0 to level-2, according to the amount of processing applied to the original data. Level-0 products are raw measurements from the onboard instruments. Level-1 products are processed raw measurements that are in physical units, as well as having transformations applied so that they are in useful coordinate systems (e.g., geographic). Level-2 refers to scientific products (e.g., field models) which make direct

use of the level-1 data. The data used for the WMM comes from the level-1(b) Swarm dataset (version 0302), which is freely provided by ESA at <https://earth.esa.int/web/guest/swarm/data-access>.

2.2.1.2 ØRSTED

The Danish satellite Ørsted (<http://www.space.dtu.dk/english/Research/Projects/Oersted>) is a dedicated satellite for geomagnetic field modeling. It was launched on 23 February 1999 from Vandenburg Air Force Base in California on a Delta II rocket, along with the American ARGOS (Advanced Research Global Observation Satellite) and the South African micro-satellite SUNSAT. Initially planned for a minimum of 14 months, Ørsted was still delivering high quality scalar data in mid-2013, more than 14 years following its launch.



SATELLITE AND ORBIT

Figure 4: Ørsted satellite

The Ørsted satellite (Figure 4) has a mass of 62 kg and measured 34 x 45 x 72 cm when the 8-m boom was stowed. The satellite was launched into a retrograde orbit with apogee ~850 km, perigee ~640 km, inclination 96.5° and nodal period 99.6 minutes.

MAGNETOMETERS

At the tip of the 8-m boom, an Overhauser magnetometer (OVH) measures the strength of the magnetic field. It is accurate to 0.5 nT. As on the Swarm satellite, the main purpose of this instrument is the absolute calibration of the vector magnetometer. The OVH was built at LETI in Grenoble and was provided by the French National Center for Space Studies, CNES. At some distance from the OVH (to avoid mutual disturbances of the magnetometers), a Compact Spherical Coil (CSC) fluxgate magnetometer, built at the Danish Technical University, measured the magnetic vector field (strength and direction) until 2005. This instrument was stable to within 0.5 nT over time spans of several days.

STAR IMAGER

A single-head star imager is co-located with the fluxgate magnetometer to determine its orientation. The star imager is accurate to about 30 arc-seconds for rotations around its axis of vision (bore sight) and to about 5 arc-seconds for rotations about any axis perpendicular to the bore sight. This instrument was built at the Danish Technical University.

GPS RECEIVER

Ørsted has a Turbo-Rogue GPS receiver to accurately determine the position of the satellite and provide time synchronization for the instruments. The GPS receiver was supplied by NASA, built at their Jet Propulsion Laboratory.

DATA PRODUCTS

The calibrated data products relevant to main field modeling are the MAG-F product for the strength of the field (scalar data) and the MAG-L product for the vector field. The data are available through the Danish National Space Institute (<http://www.space.dtu.dk>).

2.2.1.3 CHAMP

CHAllenging Minisatellite Payload (CHAMP; <http://op.gfz-potsdam.de/champ>) was a German satellite mission dedicated to improving gravity and magnetic field models of the Earth. CHAMP was proposed in 1994 by GeoForschungsZentrum Potsdam in response to an initiative of the German Space Agency (DLR) to support the space industry in the "New States" of the united Germany by financing a small satellite mission. CHAMP was launched with a Russian COSMOS vehicle on 15 July 2000 into a low Earth orbit. Designed to last five years, the mission completed a full decade before re-entry in September 2010.

SATELLITE AND ORBIT

A limiting factor for low-altitude Earth satellite missions is the considerable drag of the atmospheric neutral gas below 600 km. Satellite drag was the primary factor in the short lifespan (seven months) of the Magsat mission (1979/1980) and the reason a higher altitude orbit was chosen for Ørsted. To achieve long mission duration on a low orbit, CHAMP was constructed with a large weight (522 kg), a small cross section, and a stable attitude. The

design of Swarm was very similar to CHAMP. CHAMP was launched into an almost circular, near polar ($\text{inclination} = 87.3^\circ$) orbit with an initial altitude of 454 km. While Magsat was on a strictly sun-synchronous dawn/dusk orbit, CHAMP advances one hour in local time within eleven days. It takes approximately 90 minutes to complete one revolution at a speed of about 8 km/s.

MAGNETOMETERS

CHAMP carried the same scalar and vector magnetometers as Ørsted (Figure 5). At the tip of the 4-m long boom, a proton precession Overhauser magnetometer measured the total intensity of the magnetic field, once per second. This instrument, developed by LETI, Grenoble, had an absolute accuracy of 0.5 nT. Its measurements were used in the absolute calibration of the vector magnetometer, located mid-boom on an optical bench. The fluxgate magnetometer was developed and supplied by the Danish Technical University and sampled the field at 50 Hz with a 0.1 nT resolution.

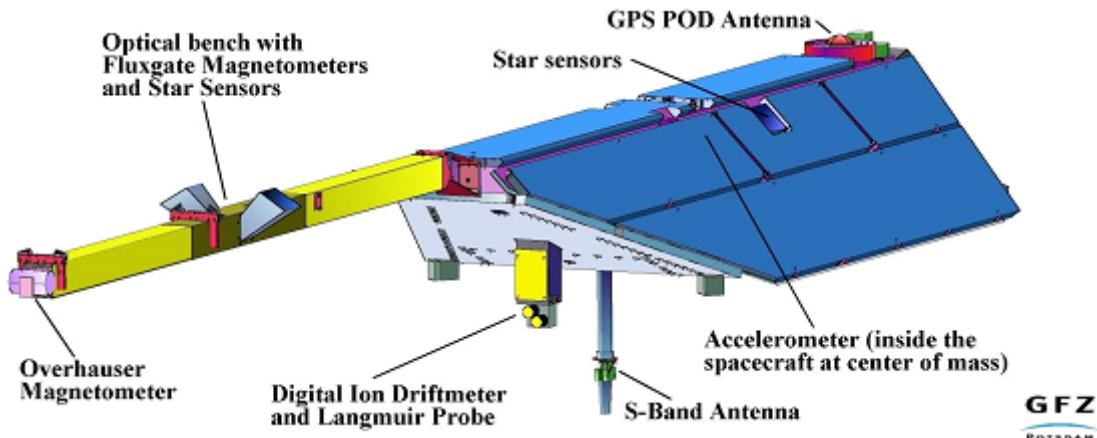


Figure 5: Front view of the CHAMP satellite

STAR IMAGERS

The star imager was built by the same laboratory as that of Ørsted (Danish Technical University), but was equipped with a dual head. This improved relative attitude by an order of magnitude to about 3 arc-seconds accuracy for rotations about all axes, corresponding to around 0.5 nT accuracy for the vector components. Since this high accuracy was only achieved in dual-head mode (62% of CHAMP data), the subsequent Swarm mission was equipped with triple-head star imagers. A further, redundant dual-head star imager on the body of CHAMP was of limited utility for the magnetic field measurements, due to the flexibility of the boom.

GPS RECEIVER

Apart from providing the accurate position of CHAMP, the Black Jack GPS receiver (supplied by NASA) had the important task of providing an absolute time frame. A pulse delivered every second was used to synchronize the instruments on board. Furthermore, it provided a stable reference frequency for the proton precession magnetometer readings, giving them absolute accuracy.

DATA PRODUCTS

CHAMP's level-3 products comprise the final processed, edited and calibrated data that were used in the WMM. These data are archived and distributed by the Information System and Data Centre (ISDC) at GFZ Potsdam (<http://isdc.gfz-potsdam.de/champ>).

2.2.1.3 IN-ORBIT CALIBRATION OF SATELLITE MAGNETOMETERS

Experience with several satellite missions shows that calibration parameters can change significantly during deployment into space. Furthermore, calibration parameters exhibit gradual changes over the life of the mission. Regular in-flight calibration and updates of the respective parameters is therefore essential. To enable a successful calibration in orbit, it is of critical importance that the instruments be built in such a way that they can be described by a linear model with constant (over one day) calibration parameters. While these parameters may change slowly over the mission lifetime, they must be independent of strength or direction of the ambient magnetic field. In particular, past satellite magnetic missions have shown that it is not possible to perform an in-orbit scalar calibration of a vector magnetometer when the component readings suffer from a "transverse field effect."

The linear instrument model used for successfully calibrating both Ørsted and CHAMP satellite magnetic data is described in detail by Olsen et al. (2003). A similar model is used for Swarm. It can be formulated as a linear transform from the desired quantity \mathbf{B} , the magnetic field vector in the reference frame of the star tracker, to the instrument output vector \mathbf{E} as

$$\mathbf{E} = \underline{\mathbf{S}} \underline{\mathbf{P}} \underline{\mathbf{R}} \mathbf{B} + \mathbf{b} \quad (22)$$

where $\underline{\mathbf{S}}$ is a diagonal matrix of scale factors, $\underline{\mathbf{P}}$ corrects for non-orthogonalities of the sensor elements, $\underline{\mathbf{R}}$ rotates from the star tracker reference frame into the vector magnetometer

frame, and \mathbf{b} is the offset vector. Each of these corrections has three parameters which have to be determined in the calibration.

The scalar in-orbit calibration is based on a comparison between the readings of the scalar and vector magnetometer. In a least-squares estimation procedure, the nine calibration parameters of a fluxgate can be determined. Here, the synthetic laboratory test field is replaced by the natural ambient field recorded over a day. This allows for regular verification of the offset vector \mathbf{b} , non-orthogonalities $\underline{\mathbf{P}}$, and scale factors $\underline{\mathbf{S}}$.

The calibration parameters of the matrix $\underline{\mathbf{R}}$, namely the three rotation angles between the magnetometer and star tracker reference systems, are determined in a final, independent step. To determine these angles, one makes use of the fact that $\text{div}(\mathbf{B})$ is zero, and chooses measurements outside of the auroral current regions, where $\text{curl}(\mathbf{B})$ is also zero. Under these circumstances, the effect of misalignments of the star tracker and vector magnetometer reference system can be separated cleanly from genuine magnetic fields, and the three calibration parameters of the matrix $\underline{\mathbf{R}}$ can be determined by a least-squares inversion. This calibration can only succeed if the vector magnetometer and the star tracker are co-mounted onto an optical bench with sufficient rigidity and temperature stability.

2.2.2 OBSERVATORY DATA

One of the principal characteristics of observatory data is the long-term continuous coverage over time. The spatial distribution of observatories is largely determined by the location of habitable land and by the availability of local expertise, funds and energy supply. While the distribution is uneven and sparse compared to that of satellite data, it has been reasonably constant in time (Figure 6).

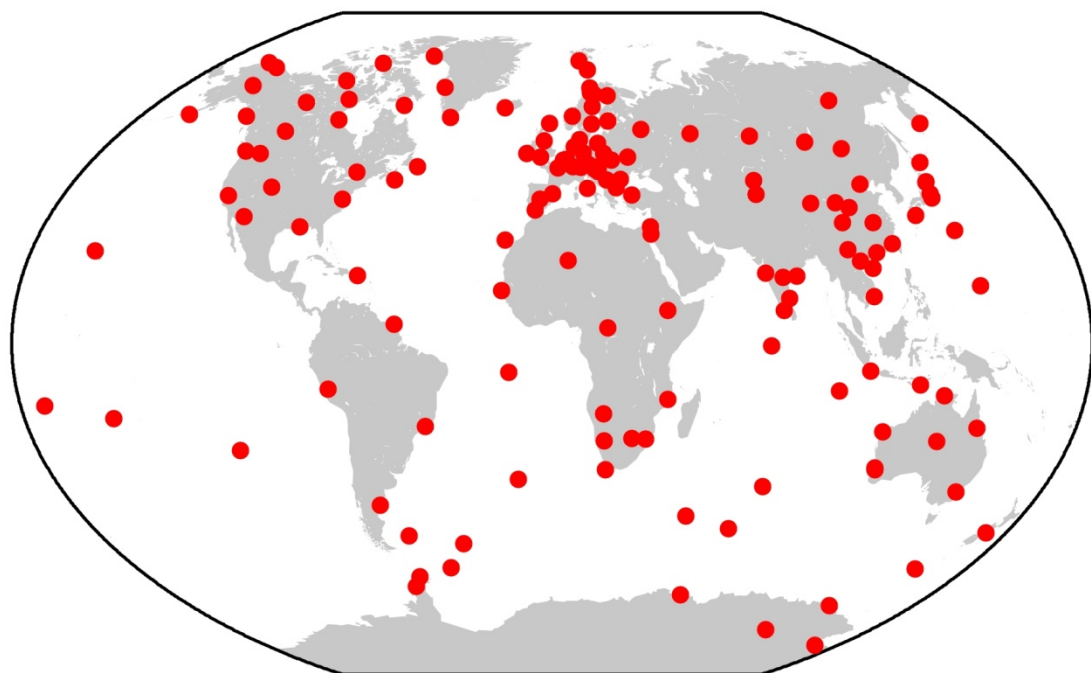


Figure 6: Locations of observatories whose data were used in WMM2015.

INSTRUMENTATION

There are three categories of instruments at an observatory. The first category comprises variometers, which make continuous measurements of elements of the geomagnetic field vector. Both analog and digital variometers require temperature-controlled environments, extremely stable platforms, and can generally operate without manual intervention. Today, the most common type of variometer is the tri-axial fluxgate magnetometer.

The second category comprises absolute instruments that can make measurements of the magnetic field in terms of absolute physical basic units or universal physical constants. The most common types of absolute instrument are the fluxgate theodolite, for measuring D and I , and the proton precession magnetometer for measuring F . In the former instrument the basic unit of measurement is an angle. To determine these angles, the fluxgate sensor mounted on the telescope of a non-magnetic theodolite is used to detect when it is perpendicular to the magnetic field vector. With the fluxgate sensor operating in this null-field mode, the stability of the sensor and its electronics is maximized. To complete the determination of D and I , true north is found by reference to a fixed mark of known azimuth, usually by astronomical observations. In a proton precession absolute magnetometer, the universal physical constant is the gyromagnetic ratio of the proton. Measurements with a fluxgate theodolite can only be made manually while a proton magnetometer can operate automatically.

The third category comprises semi-absolute instruments. These are instruments that measure deviations from a field, which is determined on a regular basis using an absolute instrument. One example is a proton vector magnetometer where artificial orthogonal bias fields are applied to a proton precession magnetometer sensor, located at the center of a set of coils through which currents can be passed, to obtain the components of the field vector. Like variometers, these instruments are temperature-sensitive and require stable platforms. For more information on magnetic instrumentation and operation of magnetic observatories, see Macmillan (2007), and Jankowski and Sucksdorff (1996).

DATA COLLATION AND QUALITY CONTROL

BGS and NOAA actively collect observatory data through their involvement in the World Data Center (WDC) system. They maintain databases suitable for magnetic field modeling, maintain contacts with organizations operating magnetic observatories, and collaborate with other WDCs. Each year BGS sends requests to all organizations with operating observatories for the latest data and other relevant information. The WDCs for geomagnetism benefit greatly from the efforts of INTERMAGNET, an organization whose objectives are to establish a global network of cooperating digital magnetic observatories, to adopt modern standard specifications for measuring and recording equipment, and to facilitate data exchange and the production of geomagnetic products in close to real time. In addition to operating eight of the observatories shown in Figure 7 (see [section 3.2.2](#)), BGS runs one of five INTERMAGNET GINs (Geomagnetic Information Node), and plays a leading role in the organization (<http://www.intermagnet.org>).

The hourly means used in the WMM were selected from definitive data held at <http://www.wdc.bgs.ac.uk> and from recent quasi-definitive data (Peltier and Chulliat, 2010; Clarke et al., 2013) produced primarily by INTERMAGNET observatories. The quality of the data an observatory produces is the responsibility of the operator. The most important aspect of the quality for global modeling is the stability of the baseline, the difference between the calibrated variometer data and the absolute observations. A baseline with many points, low scatter, few drifts and offsets is an indicator of good quality. Baseline plots for the INTERMAGNET observatories are available along with their definitive data.

Quality assurance and control measures, other than those carried out by the observatory operators, are also accomplished by INTERMAGNET through its observatory standardization program, the WDCs, and by participation in the International Association of Geomagnetism and Aeronomy (IAGA) Observatory Workshops.

Final quality control procedures prior to deriving the WMM are completed by BGS. For the hourly means this involves plotting all data to identify typographical errors and large offsets, and then plotting residuals to hourly models to identify remaining measurement artifacts such as noise, small offsets and trends. Hourly spherical harmonic models of degree 9 and order 1 are fit to residuals after estimates of the core, crustal and ionospheric fields are removed from the observatory hourly means, the details of which are in Macmillan and Olsen (2013). Observatories used in the production of WMM2015 are listed in Table 6.

Table 6: Observatories used in production of WMM2015. The number of data is the number of selected hourly mean values for 2009 and onwards, and * indicates an observatory record with a jump (i.e., an offset present at some point in the data).

| IAGA code | Latitude | Longitude | Altitude (km) | Number of data |
|-----------|----------|-----------|---------------|----------------|
| AAA | 43.183 | 76.917 | 1.300 | 1212 |
| AAE | 9.033 | 38.767 | 2.441 | 1032 |
| ABG | 18.633 | 72.867 | 0.007 | 1068 |
| ABK | 68.350 | 18.817 | 0.380 | 1419 |
| AIA | -65.250 | 295.733 | 0.010 | 823 |
| AMS | -37.833 | 77.567 | 0.048 | 301 |
| API* | -13.800 | 188.233 | 0.004 | 1108 |
| AQU | 42.383 | 13.317 | 0.682 | 306 |
| ARS | 56.433 | 58.567 | 0.290 | 553 |
| ASC | -7.950 | 345.617 | 0.177 | 1456 |
| ASP | -23.767 | 133.883 | 0.557 | 1522 |
| BDV | 49.083 | 14.017 | 0.496 | 1240 |
| BEL | 51.833 | 20.800 | 0.180 | 1322 |
| BFE | 55.633 | 11.667 | 0.080 | 486 |
| BFO | 48.333 | 8.317 | 0.641 | 759 |
| BGY | 31.717 | 35.083 | 0.750 | 1001 |
| BJN | 74.500 | 19.200 | 0.020 | 1426 |
| BLC | 64.333 | 263.967 | 0.030 | 1091 |
| BMT | 40.300 | 116.200 | 0.183 | 830 |
| BNG | 4.317 | 18.567 | 0.395 | 139 |
| BOU | 40.133 | 254.767 | 1.650 | 1522 |
| BOX | 58.067 | 38.217 | 0.115 | 1037 |
| BRW | 71.300 | 203.383 | 0.012 | 1547 |
| BSL | 30.350 | 270.367 | 0.008 | 1094 |
| CBB | 69.117 | 254.967 | 0.020 | 1086 |
| CBI | 27.100 | 142.183 | 0.155 | 838 |
| CDP | 31.000 | 103.700 | 0.653 | 1051 |
| CKI | -12.187 | 96.834 | 0.000 | 423 |
| CLF | 48.017 | 2.267 | 0.145 | 1425 |
| CMO | 64.867 | 212.133 | 0.090 | 1544 |
| CNB | -35.317 | 149.367 | 0.859 | 1537 |
| CTA | -20.083 | 146.267 | 0.370 | 1513 |
| CZT | -46.433 | 51.867 | 0.155 | 1083 |
| DLT | 11.917 | 108.417 | 0.000 | 620 |
| DMC | -75.100 | 123.383 | 3.233 | 744 |
| DOB | 62.067 | 9.117 | 0.660 | 1415 |
| DOU | 50.100 | 4.600 | 0.225 | 1362 |
| DRV | -66.667 | 140.017 | 0.030 | 1512 |
| EBR | 40.957 | 0.333 | 0.053 | 1437 |
| ELT | 29.667 | 34.950 | 0.250 | 240 |
| ESA | 39.233 | 141.350 | 0.396 | 1288 |
| ESK | 55.317 | 356.800 | 0.245 | 1437 |
| EYR | -43.417 | 172.350 | 0.120 | 1468 |
| FCC | 58.783 | 265.917 | 0.015 | 1065 |
| FRD | 38.217 | 282.633 | 0.069 | 1514 |
| FRN | 37.083 | 240.283 | 0.331 | 1108 |
| FUR | 48.167 | 11.283 | 0.572 | 874 |
| GAN | -0.695 | 73.154 | 0.030 | 635 |

| IAGA code | Latitude | Longitude | Altitude (km) | Number of data |
|-----------|----------|-----------|---------------|----------------|
| GCK | 44.633 | 20.767 | 0.231 | 975 |
| GDH | 69.250 | 306.467 | 0.024 | 1473 |
| GLM | 36.400 | 94.900 | 2.802 | 1205 |
| GNA | -31.783 | 115.950 | 0.060 | 1072 |
| GNG | -31.356 | 115.715 | 0.050 | 670 |
| GUA | 13.583 | 144.867 | 0.150 | 1462 |
| GUI | 28.317 | 343.567 | 0.868 | 820 |
| GZH | 22.967 | 112.450 | 0.011 | 308 |
| HAD | 51.000 | 355.517 | 0.095 | 1437 |
| HBK | -25.883 | 27.700 | 1.522 | 957 |
| HER | -34.417 | 19.233 | 0.026 | 1418 |
| HLP | 54.600 | 18.817 | 0.001 | 1012 |
| HON | 21.317 | 202.000 | 0.004 | 1491 |
| HRB | 47.867 | 18.183 | 0.120 | 1012 |
| HRN | 77.000 | 15.550 | 0.015 | 1307 |
| HUA | -12.050 | 284.667 | 3.312 | 1455 |
| HYB | 17.417 | 78.550 | 0.500 | 1163 |
| IPM | -27.167 | 250.583 | 0.083 | 1084 |
| IQA | 63.750 | 291.483 | 0.100 | 1047 |
| IRT | 52.167 | 104.450 | 0.540 | 1329 |
| IZN | 40.500 | 29.733 | 0.256 | 1243 |
| JCO | 70.350 | 211.200 | 0.010 | 1602 |
| KAK | 36.233 | 140.183 | 0.036 | 1505 |
| KDU | -12.683 | 132.467 | 0.014 | 1515 |
| KEP | -54.283 | 323.500 | 0.007 | 871 |
| KIR | 67.850 | 20.417 | 0.395 | 1394 |
| KIV | 50.717 | 30.300 | 0.100 | 814 |
| KMH | -26.533 | 18.117 | 1.065 | 858 |
| KNY | 31.417 | 130.883 | 0.107 | 1423 |
| KNZ | 35.250 | 139.950 | 0.342 | 1336 |
| KOU | 5.217 | 307.283 | 0.010 | 1379 |
| KPG | -10.200 | 123.667 | 0.240 | 225 |
| KSH | 39.500 | 76.000 | 1.321 | 1314 |
| LER | 60.133 | 358.817 | 0.085 | 1437 |
| LIV | -62.667 | 299.600 | 0.019 | 1114 |
| LMM | -25.917 | 32.583 | 0.010 | 94 |
| LRM | -22.217 | 114.100 | 0.004 | 1500 |
| LRV | 64.183 | 338.300 | 0.005 | 1279 |
| LVV | 49.900 | 23.750 | 0.400 | 810 |
| LYC | 64.600 | 18.733 | 0.270 | 1419 |
| LZH | 36.083 | 103.850 | 1.560 | 1322 |
| MAB | 50.300 | 5.683 | 0.440 | 1358 |
| MAW | -67.600 | 62.883 | 0.012 | 1431 |
| MBO | 14.400 | 343.050 | 0.007 | 1292 |
| MCQ | -54.500 | 158.950 | 0.008 | 1553 |
| MEA | 54.617 | 246.650 | 0.700 | 1095 |
| MIZ | 39.117 | 141.200 | 0.125 | 1303 |
| MMB | 43.917 | 144.183 | 0.042 | 1518 |
| MZL | 49.600 | 117.400 | 0.682 | 1308 |
| NAQ | 61.167 | 314.567 | 0.004 | 912 |
| NCK | 47.633 | 16.717 | 0.160 | 815 |
| NEW | 48.267 | 242.867 | 0.770 | 1528 |
| NGK | 52.067 | 12.683 | 0.078 | 1410 |

| IAGA code | Latitude | Longitude | Altitude (km) | Number of data |
|-----------|----------|-----------|---------------|----------------|
| NMP | -15.100 | 39.250 | 0.374 | 685 |
| NUR | 60.500 | 24.650 | 0.105 | 814 |
| NVS | 54.850 | 83.233 | 0.130 | 1506 |
| ORC | -60.733 | 315.217 | 0.000 | 84 |
| OTT | 45.400 | 284.450 | 0.075 | 1099 |
| PAF | -49.350 | 70.250 | 0.015 | 1502 |
| PAG | 42.517 | 24.183 | 0.556 | 1279 |
| PET | 52.967 | 158.250 | 0.110 | 1147 |
| PHU | 21.033 | 105.967 | 0.005 | 1028 |
| PLR | -6.967 | 106.550 | 0.054 | 216 |
| PND | 11.917 | 79.917 | 0.000 | 823 |
| PPT | -17.567 | 210.433 | 0.357 | 1116 |
| PST | -51.700 | 302.100 | 0.135 | 1478 |
| QGZ | 19.000 | 109.800 | 0.227 | 1158 |
| QIX | 34.600 | 108.200 | 0.893 | 1328 |
| QZH | 24.900 | 118.600 | 0.010 | 1249 |
| RES | 74.683 | 265.100 | 0.030 | 1089 |
| SBA | -77.850 | 166.783 | 0.010 | 1366 |
| SBL | 43.933 | 299.983 | 0.005 | 1484 |
| SFS | 36.467 | 353.800 | 0.000 | 1021 |
| SHU | 55.350 | 199.533 | 0.080 | 1083 |
| SIT | 57.067 | 224.667 | 0.024 | 1098 |
| SJG | 18.100 | 293.850 | 0.424 | 1442 |
| SOD | 67.367 | 26.633 | 0.178 | 815 |
| SPT | 39.550 | 355.650 | 0.922 | 1437 |
| STJ | 47.600 | 307.317 | 0.100 | 667 |
| SUA | 44.683 | 26.250 | 0.084 | 1278 |
| TAM | 22.800 | 5.533 | 1.373 | 1377 |
| TDC | -37.100 | 347.683 | 0.042 | 1209 |
| THJ | 24.000 | 102.700 | 1.820 | 1317 |
| THL | 77.483 | 290.833 | 0.057 | 1561 |
| THY | 46.900 | 17.900 | 0.187 | 1240 |
| TIR* | 8.667 | 77.817 | 0.000 | 805 |
| TRO | 69.667 | 18.950 | 0.105 | 1428 |
| TRW | -43.267 | 294.617 | 0.015 | 801 |
| TSU | -19.200 | 17.583 | 0.083 | 551 |
| TUC | 32.167 | 249.267 | 0.770 | 1094 |
| UPS | 59.900 | 17.350 | 0.050 | 1419 |
| VAL | 51.933 | 349.750 | 0.014 | 1279 |
| VIC | 48.517 | 236.583 | 0.197 | 1110 |
| VSK | 17.667 | 83.317 | 0.000 | 555 |
| VSS | -22.400 | 316.350 | 0.457 | 742 |
| WHN | 30.533 | 114.567 | 0.042 | 1329 |
| WIK | 48.267 | 16.317 | 0.400 | 1012 |
| WNG | 53.750 | 9.067 | 0.050 | 1402 |
| YAK | 61.967 | 129.667 | 0.100 | 1054 |
| YKC | 62.483 | 245.517 | 0.198 | 1006 |

2.2.3 OTHER DATA AND DERIVED PRODUCTS

Other magnetic data and products used in the production of the WMM are various magnetic activity indices derived from observatory data, and solar wind data measured by the ACE satellite (<http://www.srl.caltech.edu/ACE>). These are used to either select the data for input to the model or to form part of the input to the model.

INDEX K_P

The planetary K_p ("Planetarische Kennziffer") index (<http://www.gfz-potsdam.de/en/research/organizational-units/departments/department-2/earths-magnetic-field/services/kp-index>) is based on the K-index, a local index of the three-hourly range in magnetic activity of the two horizontal field components (X and Y) relative to an assumed quiet-day curve for the geomagnetic observatory. Local disturbance levels are determined by measuring the range (difference between the highest and lowest values) during three-hour time intervals for the most disturbed magnetic field component. The range is then converted into a local K-index according to a pseudo-logarithmic scale, which is station specific, in an attempt to normalize the frequency of the different disturbance sizes. The three-hourly K_p index is the average of local K values from 13 selected subauroral stations and is expressed in a scale of thirds (28 values). The IAGA station codes (in order of geomagnetic latitude) are: LER, MEA, SIT, ESK, UPS, OTT, BFE, HAD, WNG, NGK, FRD, CNB and EYR. Prior to the averaging, the K values are standardized according to station and season. Also CNB and EYR are averaged first, as are UPS and BFE and then used as single points in the overall average of eleven. The K_p index is used to select measurements during magnetically undisturbed times.

INDEX DST

Charged particles trapped by the geomagnetic field in the magnetosphere drift around the Earth at a distance of 3-8 Earth radii creating a westward electric ring current whose field opposes the main geomagnetic field. The strength of this field is on the order of tens of nT during quiet times and several hundred nT during magnetic storms. Magnetopause, tail and partial ring currents represent additional contributions leading to asymmetries in the field which increase during storms. The symmetric part of this composite disturbance field is tracked by the Dst (disturbance storm-time) index (Sugiura, 1964; <http://wdc.kugi.kyoto->

u.ac.jp/dstdir). It is derived from the measurements collected at four low latitude observatories. The Dst index is used both for data selection and, in terms of the Est/Ist index described below, as a quantitative correction of the disturbance field.

INDICES EST / IST

The Dst index is meant to track the strength of a uniform field in the magnetic northward direction. In practice, however, the measured field is the sum of the external and induced parts. When representing magnetospheric fields by Dst, it is important to separate the external and internal contributions to Dst due to their very different geometries. Using a global conductivity model of the Earth, the Dst index can be separated into Est and Ist indices tracking the external and internal contributions, respectively (Maus and Weidelt, 2004). The Est/Ist indices are available at http://www.ngdc.noaa.gov/geomag/est_ist.shtml. They are used to subtract contributions of the magnetic disturbance field from the data used for estimating the WMM coefficients.

INTERPLANETARY MAGNETIC FIELD

The solar wind drives electric currents in the Earth's magnetosphere and ionosphere. An interplanetary magnetic field (IMF) is carried by the plasma of the solar wind. Relevant for the response of the magnetosphere is the speed of the solar wind and the direction and strength of the IMF. These solar wind parameters are monitored by NASA's Advanced Composition Explorer (ACE) satellite (<http://www.srl.caltech.edu/ACE>). Using magnetospheric models, the ACE solar wind measurements are projected downstream onto the magnetospheric bow shock (the boundary between the solar wind and the magnetosphere) and are made available by NASA as 1-minute readings in geocentric magnetospheric coordinates at <http://omniweb.gsfc.nasa.gov/hw.html>. The IMF is used both for data selection and as a quantitative parameter to correct for magnetospheric disturbance fields.

MERGING ELECTRIC FIELD E_M

The merging electric field, derived from the IMF and solar wind speed (<http://omniweb.gsfc.nasa.gov/hw.html>), is a parameter suitable for describing the variation of

the magnetospheric tail current field. Following Kan and Lee (1979), the merging electric field, E_m , is calculated as

$$E_m = v_{SW} \left(B_y^2 + B_z^2 \right)^{\frac{1}{2}} \sin^2 \left(\frac{\Theta}{2} \right) \quad (23)$$

where v_{SW} is the solar wind velocity, B_y and B_z are the IMF components in the Geocentric Solar Magnetospheric (GSM) frame and Θ is the clock angle of the IMF (i.e., the angle made by the B_y and B_z components of the IMF in the vertical plane to the ecliptic, counted from 0 when IMF B_z is north). The merging electric field goes into saturation for strong solar wind driving. In the parameterization of the tail current field we therefore use the effective field, E'_m , defined as

$$E'_m = \frac{E_{thresh} E_m}{\sqrt{E_{thresh}^2 + E_m^2}} \quad (24)$$

where the threshold electric field is $E_{thresh} = 8$ mV/m.

The merging electric field is used for quantitative correction of disturbance fields.

SOLAR FLUX INDEX F10.7

Extreme ultraviolet (EUV) radiation from the sun ionizes the Earth's atmosphere. A moving 81-day average of the F10.7 solar flux index (available at <http://www.spaceweather.gc.ca/sx-eng.php>) has been shown to provide a good proxy for the intensity of the EUV radiation. The moving average, commonly referred to as F10.7a, also provides a useful proxy for the progression of the solar cycle (<http://www.swpc.noaa.gov/products/solar-cycle-progression>). Magnetic activity is known to lag behind the solar cycle. In magnetospheric field models, the time varying bias of the Dst index can therefore be described using F10.7a with a 20-month time lag. The F10.7a index was used here to correct for solar-cycle dependent magnetospheric disturbance fields.

2.3 DERIVATION OF THE MODEL

Since the WMM only describes the long-wavelength internal part of the geomagnetic field, it is important to separate unrelated contributions to the field, which would otherwise contaminate the WMM coefficients. A successful modeling strategy relies on four elements:

1. DATA SELECTION

Measurements during daytime and during periods of strong solar activity are contaminated by external current systems, which are difficult to accurately model. Therefore, only nighttime data during magnetically quiet periods, as inferred from the above-described indices, were used in estimating the WMM coefficients.

2. DATA CORRECTIONS

Some contributions to the measured magnetic field, such as the crustal magnetic field and the magnetospheric field can be accurately modeled and were corrected for prior to the estimation of the WMM main field coefficients.

3. DATA WEIGHTING

The disturbance field includes features that, even after careful data selection, cannot be modelled. Data including these features, in particular the auroral electrojets, are downweighted in the estimation of the WMM SV coefficients.

4. USE OF EXTENDED PARENT MODELS

To account for contributions that have not been removed in the previous three steps, an extended set of model parameters is co-estimated with the WMM model coefficients. These account for smaller-wavelength internal magnetic field contributions (spherical harmonic degree larger than 12), higher time derivatives (e.g., secular acceleration) and contributions from currents external to the Earth. The set of WMM coefficients plus the extended model parameters is called a *parent model* of the WMM. Two separate parent models were produced, reflecting different modeling strategies employed by NGDC for the main field model and BGS for the secular variation model.

2.3.1 PARENT MODEL FOR MAIN FIELD COEFFICIENTS

The main field parent model was produced from Swarm and Ørsted satellite mission data. Swarm provides the primary set of measurements due to its small polar gap, three-head star camera for accurate attitude determination, and low-noise vector and scalar data. Ørsted provides only scalar field measurements. The following sections describe data selection, corrections and parent model parameterization for the main field coefficients.

DATA SELECTION

Swarm data from all three satellites were used, spanning the time interval 2013.9 to 2014.8 and subsampled to 20 seconds, corresponding to about 140-km along-track spacing. Vector measurements were used only at mid-latitudes (between -55° and +55° geomagnetic latitude), and scalar data were used at all latitudes. Ørsted scalar data was also used from the time period 2013.0 to 2013.5 at all latitudes. For all four satellites, at mid-latitudes, data were selected from the 22:00-5:00 local time sector. At high-latitudes (above 55° geomagnetic latitude), data with a solar zenith angle less than 100° were excluded to ensure the satellites are in darkness (Table 7).

Table 7: Summary of data selection criteria used when producing the parent model for the main field coefficients. Mid-latitudes refer to track segments spanning -55° to 55° geomagnetic latitudes. High-latitudes refer to track segments at <-55° and >55° geomagnetic latitudes.

| | Mid-latitudes | High-latitudes |
|------------------------|----------------------|---|
| $ Dst $ | $\leq 30 \text{ nT}$ | $\leq 30 \text{ nT}$ |
| K_p | $\leq 2\circ$ | $\leq 3-$ |
| $ By \text{ of } IMF $ | | $\leq 8 \text{ nT}$ |
| $Bz \text{ of } IMF$ | | $\geq -2 \text{ nT}, \leq 6 \text{ nT}$ |

DATA CORRECTION AND WEIGHTING

The following corrections were applied to the fully calibrated satellite data:

1. An external magnetospheric model was subtracted from the data. Due to the local-time asymmetry of magnetospheric fields, day-side data must be included in the modeling. Since day-side data are too noisy for inclusion in the modeling of the main

field, the magnetospheric fields are best estimated in a separate processing step. A revised version of the model described in Maus and Lühr (2005) was used. This 18-parameter model quantifies the quiet-time magnetospheric fields, modulated by the Interplanetary Magnetic Field and solar activity. Details of the magnetospheric model are given in Lühr and Maus (2010).

2. The MF7 model, which represents the static internal field due to magnetic anomalies in the Earth's crust, was subtracted from the data. MF7 spans spherical harmonic 16 to 133 and is more fully described in Maus et al. (2008).
3. For vector measurements from the Swarm satellites, Euler rotation angles were computed, representing a fixed rotation from the fluxgate magnetometer frame to the star camera frame. These angles can differ slightly from their preflight values due to thermal and mechanical noise effects.
4. The local data density per unit area at orbital altitude was determined and then used to spatially weight the data. Such a weighting scheme improves the accuracy of the resulting model.

MODEL DESCRIPTION

The parent model for the main field is comprised of:

1. The static part of the internal field to degree and order 20.
2. The secular variation (SV) to degree and order 15.
3. A daily varying degree-1 external field represented by a single value of the strength of the axial dipole field in the Solar-Magnetic (SM) frame for every 24-hour interval. This parameter helps to correct for unknown shifts in the Dst baseline.

To estimate the final model coefficients, we perform a least-squares minimization of the residuals between the data and the model. Because some of the residuals are nonlinear functions of the model parameters, for example the Euler rotation angles, and the Gauss coefficients appearing in the scalar residuals, we use an iterative nonlinear least-squares approach. Full details of this minimization procedure can be found in Alken et al (2015). Once the Gauss coefficients are determined, they are truncated to spherical harmonic degree 12 for the final WMM main field.

2.3.2 PARENT MODEL FOR SECULAR VARIATION COEFFICIENTS

A combined dataset of satellite and ground observatory measurements was used to produce the parent model for estimating the secular variation coefficients. By using data from both satellites and observatories the spatial and temporal continuity is enhanced so as to better characterize the secular variation. The following three sections describe data selection, data weighting, and parent model parameterization for the secular variation coefficients.

DATA SELECTION

Ørsted, CHAMP, and Swarm scalar and vector data were selected between 2009.0 and 2014.8. Scalar data were used only where vector data were unavailable. All satellite data were sub-sampled to every 20th sample (about 20 seconds apart). Equator-ward of 50° geomagnetic latitude, data were selected from the 22:30-05:00 local time sector. Pole-ward of 50° geomagnetic latitude, data were used at all local times and no exclusion based on solar zenith angle was made, in order to avoid seasonal data gaps at high latitudes. Additional selection criteria are given in Table 8.

Vector observatory hourly means were selected within 01:00 to 02:00 local time sector for 148 observatories around the world. Additional selection criteria are given in Table 8. The observatories used and the final numbers of selected hourly mean values are listed in Table 6. The observatory records in Table 6 that are listed as including an unquantified jump were split into two and separate crustal biases are solved for in the parent model. The observatory data were rotated from a geodetic to a geocentric coordinate system.

Table 8: Summary of satellite and observatory data selection criteria, additional to local time, used when producing the parent model for the secular variation coefficients.

| Data selection criteria | |
|--|---|
| Satellite data | |
| Magnetic indices: | |
| K_p | $\leq 2-$ |
| K_p for previous 3 hours | $\leq 2-$ |
| $ dDst/dt $ | $\leq 5 \text{ nT/h}$ |
| Solar wind data: | |
| IMF-Bz | $\geq 0 \text{ nT}, \leq 6 \text{ nT}$ |
| IMF-By | $\geq -3 \text{ nT}, \leq 3 \text{ nT}$ |
| IMF-Bx | $\geq -10 \text{ nT}, \leq 10 \text{ nT}$ |
| Solar wind speed | $\leq 450 \text{ km/s}$ |
| Data consistency check: | |
| $ $ observed magnetic field value - value from <i>a priori</i> model $ $ | $\leq 700 \text{ nT}$ |
| $ $ scalar F from OVH – vector F from CSC $ $ | $\leq 2 \text{ nT}$ |
| Observatory data | |
| Magnetic indices: | |
| K_p | $\leq 2+$ |
| $ dDst/dt $ | $\leq 5 \text{ nT/h}$ |
| Solar wind data: | |
| IMF-Bz | $\geq -2 \text{ nT}$ |

DATA CORRECTION AND WEIGHTING

Corrections were not applied to the satellite data as the magnetospheric field signals are co-estimated in the parent model. The variance associated with each datum was calculated from a combination of the following three quantities (Thomson et al., 2010):

1. a measure of local magnetic activity using the standard deviation along short segments (20 samples) of satellite track,
2. a larger-scale noise estimator derived from activity measured at the geographically nearest magnetic observatories to the sample point, and
3. the number of data per unit area of the globe relative to the mean number of data per unit area. This effectively down-weights higher latitude data.

For high geomagnetic latitudes observatory data were projected onto an *a priori* model vector and the resulting pseudo-scalar data were used in the inversion. For other latitudes, vector data were used. They were then weighted according to the following two criteria:

1. High latitude pseudo-scalar data were assigned lower weight than lower latitude vector data.
2. Pseudo-scalar data were further weighted according to the cosine of the solar zenith angle.

The final ratio of the total weights, estimated by the inverse of the sum of the data variances, of satellite:observatories is approximately 10:1.

MODEL DESCRIPTION

The parent model comprises:

1. The static part of the internal field to degree and order 55.
2. Order 6 B-spline time dependence to internal degree and order 13 with nodes 1 year apart. Order 6 spline means that the 1st to 5th derivatives are continuous functions.
3. Degree and order 1 external field with time-dependence derived from the Vector Magnetic Disturbance index (Thomson and Lesur, 2007); piecewise-linear terms with nodes ¼ year apart; and 24 hour, semi-annual, and annual periodicities. Induced terms also included.
4. Individual terms for the observatory crustal biases.

In order to linearize the problem, scalar satellite data were assumed to lie in a direction estimated by an *a priori* main field model. The model parameters are fit using a regularized minimum norm approach that balances the fit of model to the data with temporal smoothing. This smoothing is necessary to control the time-varying coefficients, especially over periods of varying data coverage through the period 2011-2013 where the parent model relies more heavily on observatory data.

The secular variation coefficients were set equal to the average of the instantaneous rates of change of the internal coefficients from the parent model at 0.1 year intervals between 2013.6 and 2014.5 inclusive.

2.3.3 VALIDATION PROCESS

The existence of two parent models permitted inter-comparison of sets of WMM2015 coefficients. The use of slightly different data sets and modeling methods allows for semi-independent validation of the resulting models, adding confidence to the resulting WMM. The final coefficients were drawn from the NGDC parent model for the main field and from the BGS parent model for the secular variation.

3. MODEL UNCERTAINTIES

The WMM2015 is valid for the period 1 January 2015 to 31 December 2019 at or near the Earth's surface, up to a few hundred kilometers of altitude. However, like any physical model it contains uncertainties that must be carefully considered by its users. This section discusses the various sources of uncertainty for the WMM2015 and quantifies the uncertainties associated with each source at or near the Earth's surface. The uncertainties are then combined into a total error budget, which forms the basis of a simple error model providing the uncertainty for each component of the field.

3.1 SOURCES OF UNCERTAINTY

Apart from human-made disturbances of the measurement, which are not discussed here, there are two sources of disagreement between magnetic field observations and the WMM. The first is due to inaccuracies in the model coefficients and is often referred to as the *commission* error. The second is due to the fact that the WMM does not account for all of the contributions to the observed magnetic field and is often referred to as the *omission* error.

The commission error is the sum of errors due to inaccuracies in main field coefficients, describing the field in 2015.0, and predictive secular variation coefficients, describing the linear part of the field variation from 2015.0 to 2020.0. Since the early 2000s, inaccuracies have been much reduced due to a series of high-precision magnetic survey satellites. However, in the case of the secular variation there is an additional error due to the fact that the true secular variation is not exactly linear. This is because changes of the fluid flow in the Earth's outer core lead to slightly nonlinear changes in the Earth's magnetic field. The nonlinear part of the secular variation is currently unpredictable, but, fortunately, it is small compared to the linear secular variation. It follows that, by surveying the field for several years, one can precisely map the present field and its rate of change, and then linearly extrapolate the rate out into the future for several years. Provided that suitable satellite magnetic observations are available, the prediction of the WMM is highly accurate on its release date and then subsequently deteriorates towards the end of the 5-year epoch, when it has to be updated with revised values of the model coefficients.

The omission error is due to portions of the geomagnetic field that cannot be described by the WMM because either their spatial scale is too small or their time scale is too short. Most of

these contributions are generated in the Earth's crust and upper mantle, and in the ionosphere and magnetosphere, whereas the long-wavelength portion of the Earth's magnetic field represented by the WMM originates within the Earth's fluid outer core. Sources in the crust and upper mantle produce static spatial anomalies, and sources in the ionosphere and magnetosphere produce rapidly varying disturbance fields, either global or regional. The omission error is the largest contributor to the total error (see [section 3.2](#)) and can reach very large values in some locations and at certain times. For example, differences between the observed declination and the WMM can exceed 10 degrees. Anomalies of this magnitude are uncommon but do exist. Declination anomalies on the order of 3 or 4 degrees are not uncommon but are usually of small spatial extent.

On land, spatial anomalies are produced by mountain ranges, ore deposits, cloud to ground lightning, geological faults, etc. The corresponding deviations are usually smaller at sea, increase with increasing latitude, and decrease with increasing altitude of an air- or spacecraft. In ocean areas these anomalies occur most frequently along continental margins, near seamounts, and near ocean ridges, trenches and fault zones, particularly those of volcanic origin.

Since the crustal field is almost constant in time, it can be inferred from all available satellite, marine and aeromagnetic measurements of the past decades. These data have been compiled into an ellipsoidal degree-720 Enhanced Magnetic Model (EMM), available at <http://www.ngdc.noaa.gov/geomag/EMM>. Developed as research models for NGA, the EMM 2010 and the upcoming EMM 2015 provide consistent global representation of the magnetic field, including the crustal field, down to wavelengths of approximately 56 kilometers. The new WMM subroutine library was designed so that it can be used with the EMM. Use of the EMM should be considered in applications with higher demands in pointing accuracy.

3.2 ESTIMATING UNCERTAINTY

Various approaches were used to estimate the WMM2015 uncertainty. Some approaches provide the uncertainties associated with one type of error and/or one omitted source, while others provide combined uncertainties for different sources. It is important to recognize that the omission error, particularly the one associated to the crustal field, dominates over the commission error, and that the omitted sources are only partially sampled in space and time. Therefore, it is not possible to precisely estimate the WMM2015 uncertainty in every location

at the Earth's surface. What is achievable is a global estimate of the uncertainty, based upon a statistical analysis of the differences between the WMM2015 and its predecessors and independent geomagnetic measurements in as many locations as possible at the Earth's surface.

3.2.1 FORMAL COMMISSION ERROR

The errors on the Gauss coefficients of the WMM2015 can be formally estimated from the variance-covariance matrix of these coefficients, defined as

$$\underline{\mathcal{C}} = (\underline{\mathbf{J}}^T \underline{\mathbf{W}} \underline{\mathbf{J}})^{-1} \quad (25)$$

where $\underline{\mathbf{J}}$ is the Jacobian matrix of the nonlinear least squares penalty function used when calculating the main field parent model, and $\underline{\mathbf{W}}$ is a diagonal weighting matrix whose entries are given by $w_i = 1/\sigma_i^2$, with σ_i the error of the i-th measurement. The measurement error is the sum of the instrument error and the error caused by un-modeled fields at satellite altitude. A total measurement error σ was estimated using the final Gauss coefficients of the model as the RMS (root mean square) of the differences between measurements and model predictions. This total error was assigned to each measurement in the weighting matrix.

The errors on the Gauss coefficients were then propagated to errors in magnetic field elements X, Y, Z, H, F, I and D . Taking for example the X element, and computing its model prediction as a set of points all over the Earth's surface will yield a vector $\underline{\mathbf{X}}$. This vector is linearly related to the Gauss coefficients (see equations 10, 11 and 12 in [section 1.2](#)) and so we can write $\underline{\mathbf{X}} = \underline{\mathbf{A}} \underline{\mathbf{g}}$ for a matrix $\underline{\mathbf{A}}$. The variance-covariance matrix of the X element will then be

$$\underline{\mathcal{C}}_X = \underline{\mathbf{A}} \underline{\mathcal{C}} \underline{\mathbf{A}}^T \quad (26)$$

Similar expressions exist for the Y and Z elements. The H, F, I and D elements are related to X, Y and Z by non-linear functions that can be linearized to get similar expressions for their variance-covariance matrices. The diagonal elements of each variance-covariance matrix then give estimates of the commission error for the chosen set of measurement points. The global error for each element was obtained by computing the global RMS of these errors and is given in Table 9.

Table 9: Formal commission errors at Earth's surface.

| Row | | X (nT) | Y (nT) | Z (nT) | H (nT) | F (nT) | I (°) | D (°) | GV (°) |
|-----|-----------------------------------|-----------|-----------|-----------|-----------|-----------|----------|----------|-----------|
| 1 | Formal commission error at 2015.0 | 0.23 | 0.22 | 0.36 | 0.23 | 0.35 | 0.00 | 0.01 | |
| 2 | Formal commission error at 2020.0 | 0.86 | 0.84 | 1.33 | 0.86 | 1.28 | 0.00 | 0.03 | |

3.2.2 COMMISSION ERROR FROM MODEL COMPARISONS

As different data and modelling approaches are used by BGS and NOAA, some insight into the errors arising from incorrect modelling and prediction of the core field signal up to degree 12 can be gained by inter-comparing their respective models and by comparing preliminary and final WMM2015 with WMM2010. These comparisons are done by computing the component values on a 1° latitude/longitude grid (defined using geocentric latitude), and calculating RMS differences weighted by the cosine of the latitude. Table 10 lists these differences.

Table 10: RMS differences at Earth's surface. These approximate the core field contributions to overall errors. Note increase in error if model not updated every 5 years (rows 7 and 8).

| Row | | X (nT) | Y (nT) | Z (nT) | H (nT) | F (nT) | I (°) | D (°) | GV (°) |
|-----|---|-----------|-----------|-----------|-----------|-----------|----------|----------|-----------|
| 1 | NOAA prelim 2 Sep – BGS prelim 17 Sep at 2015.0 | 6 | 4 | 8 | 5 | 7 | 0.01 | 0.07 | 0.16 |
| 2 | NOAA prelim 2 Sep – BGS prelim 17 Sep at 2020.0 | 32 | 33 | 52 | 34 | 38 | 0.08 | 0.22 | 0.48 |
| 3 | 2015prelim - WMM2010 at 2015.0 | 45 | 50 | 78 | 47 | 60 | 0.10 | 0.47 | 1.08 |
| 4 | NOAA final – BGS final at 2015.0 | 3 | 3 | 5 | 3 | 4 | 0.01 | 0.05 | 0.11 |
| 5 | NOAA final – BGS final at 2020.0 | 21 | 17 | 31 | 19 | 29 | 0.03 | 0.16 | 0.35 |
| 6 | WMM2015 - WMM2010 at 2015.0 | 46 | 50 | 79 | 47 | 60 | 0.10 | 0.50 | 1.14 |
| 7 | WMM2015 - WMM2010 at 2020.0 | 101 | 174 | 175 | 104 | 129 | 0.33 | 0.63 | 1.39 |
| 8 | WMM2015 - WMM2005 at 2015.0 | 141 | 133 | 233 | 141 | 174 | 0.29 | 0.49 | 0.96 |

The differences between WMM2010 and WMM2015 predictions for the magnetic field at 2015.0 are shown in Figure 7. The spatial distribution of differences is not necessarily an indication of where the largest errors will occur in the future. However the largest errors in declination and grid variation will again be concentrated near the magnetic poles where the strength of the horizontal component of the field is lowest.

To further demonstrate the difficulty in modelling declination near the magnetic poles the differences in declination between the two parent models from BGS and NOAA, truncated at degree 12, at 2015.0 and 2020.0 are shown in Figure 8.

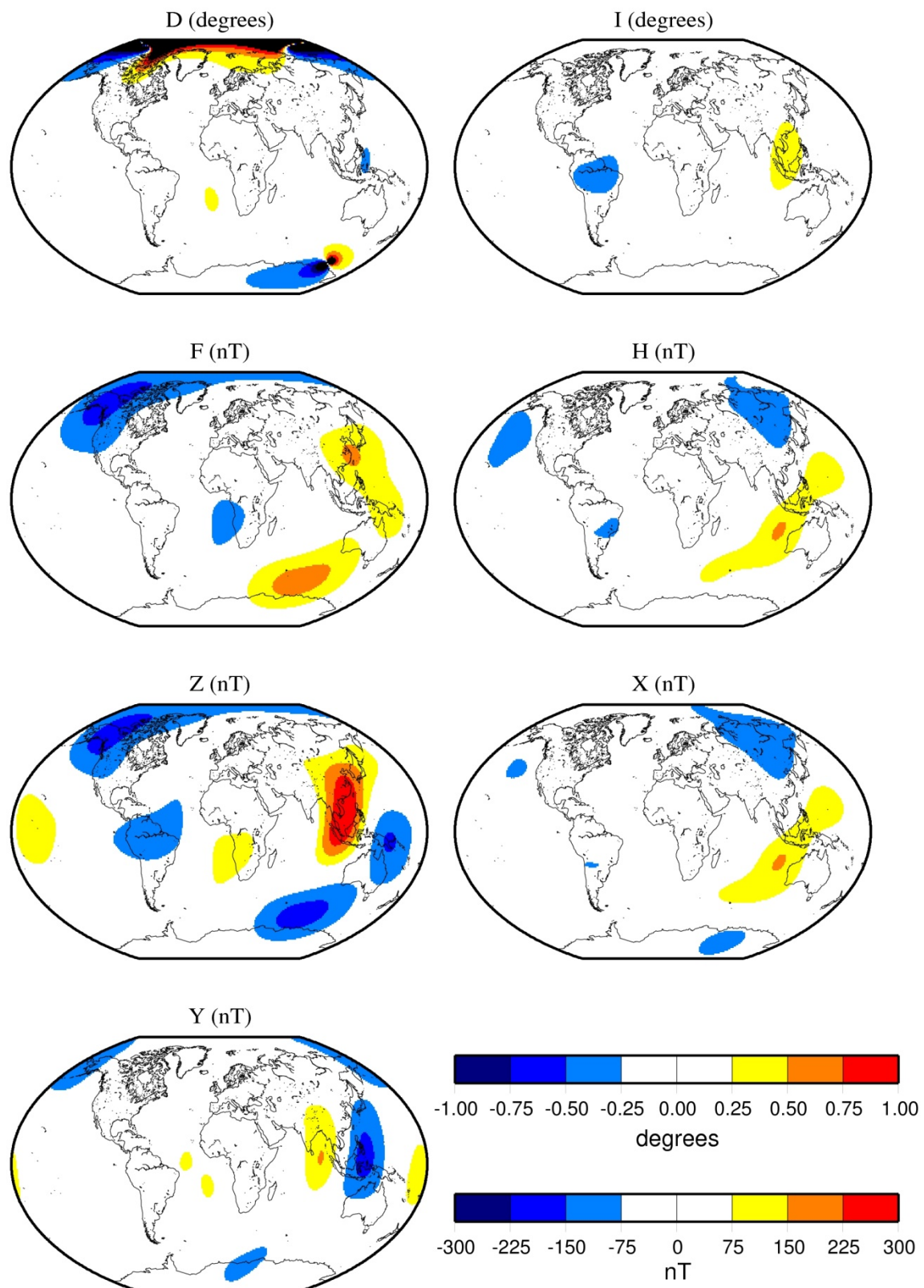


Figure 7: Differences at Earth's surface between WMM2015 and WMM2010 at 2015.0.

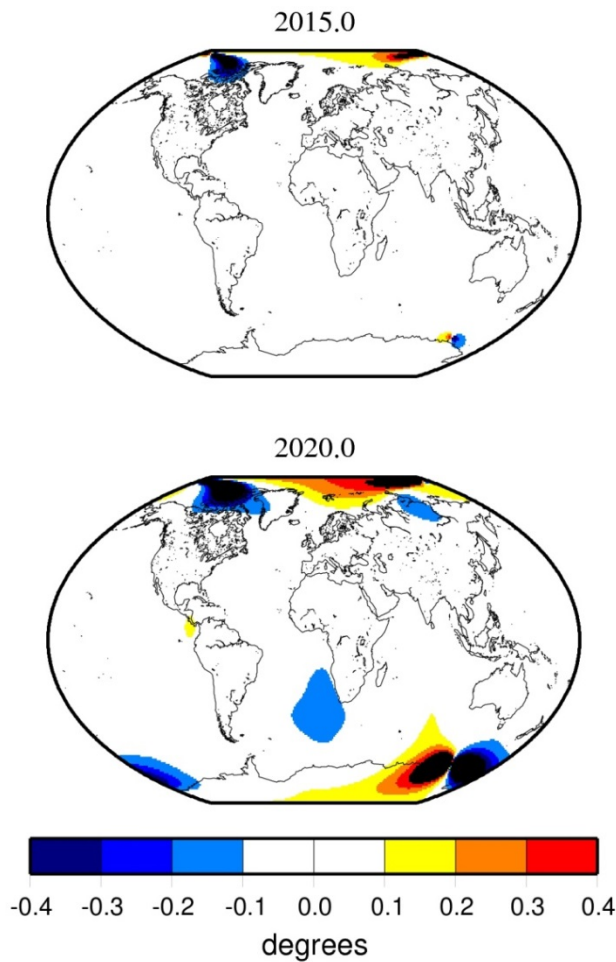


Figure 8: Differences at Earth’s surface in declination from BGS and NOAA truncated parent models at 2015.0 and 2020.0

3.2.3 CRUSTAL FIELD AND SECULAR VARIATION CONTRIBUTIONS – METHOD #1

The crustal field is the largest source of uncertainty of the WMM near the Earth’s surface. Although high resolution crustal field models (such as the EMM) exist, they only describe the largest spatial scales of the crustal field. Therefore, any rigorous attempt to quantify the crustal field contribution to the omission error should rely on actual field measurements. A first method for estimating the crustal field error consisted in comparing past WMM predictions for years 2000-2014 with (a) trackline data from 189 aeromagnetic and marine surveys archived in NGDC’s GEODAS (GEOphysical Data System), and (b) data from 162 geomagnetic observatories archived at BGS’s World Data Centre for Geomagnetism in Edinburgh.

Trackline data have several advantages compared to observatory data when investigating the crustal field error. First, they sample the crustal field at a much larger number of points. The GEODAS dataset used for this analysis includes a total of 6,857,662 data points at different

locations, to be compared with 162 observatory locations. Second, trackline data are typically acquired a few kilometers above the crustal field sources (due to the plane altitude or the depth of the ocean below the survey vessel), which reduces the amplitude of the smallest spatial scales of the field, including very local human-made anomalies. There are disadvantages, however, as only total field data are available from marine and aeromagnetic surveys and it is generally impossible to separate the crustal field from the external field in such data. The following analysis is an attempt at combining advantages from both trackline and observatory datasets.

As a first step, residuals between trackline data and past WMM predictions over 2000-2014 were calculated and sorted according to absolute corrected geomagnetic latitude. Overall, the residuals were found to be normally distributed. RMS values of residuals within each 10 degrees latitudinal bin were then calculated. The obtained values (Figure 9) include both the commission error (mostly the error due to incorrect prediction of the secular variation over each WMM five-year time interval, see [section 3.2.2](#)) and the omission error, with contributions from both the crustal field and the external field. There is a small but clear dependence of the error with latitude, partly due to an increase of the crustal field with latitude, as shown by models such as the degree-720 Enhanced Magnetic Model (EMM), and partly due to the effect of the external field which becomes larger on average near 65° geomagnetic latitude (see [section 3.2.5](#)).

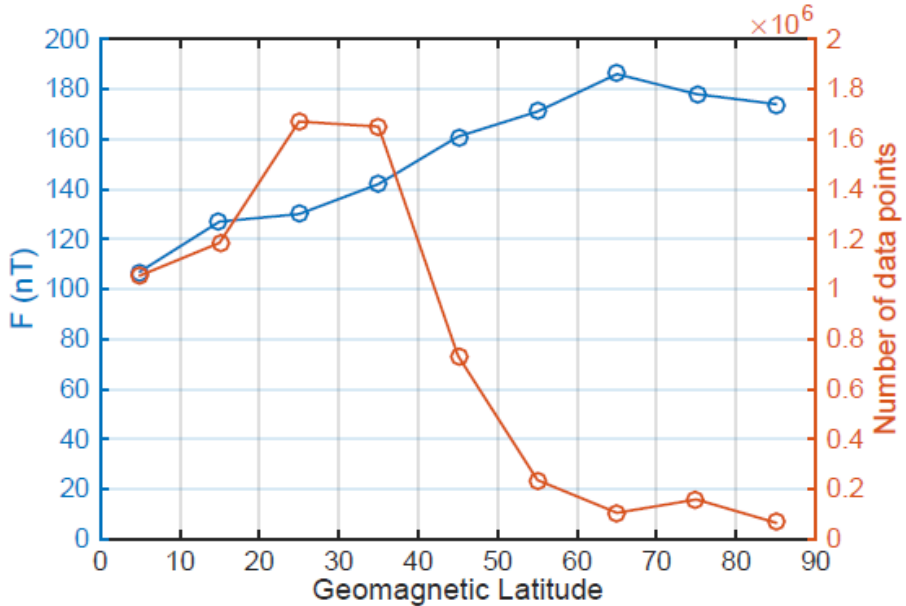


Figure 9: RMS differences between trackline data and WMM for years 2000-2014, sorted accorded to absolute corrected geomagnetic latitude (Richmond, 1995), and corresponding number of data in each 10 degrees latitudinal bin.

As a second step of the analysis, hourly mean values from 162 observatories over 2000-2014

were least-square fitted by cubic splines with knots every year. This procedure removes most of the external field, which varies with timescales smaller than one year, except for some small external fields varying with the 11-year solar cycle. Each spline fit therefore represents the sum of the crustal and core fields at the observatory location. RMS differences between spline fits and WMM predictions were then calculated for each component within 10° latitudinal bins. The RMS error on F was found much larger than the one from trackline data; for example, the RMS error for the 10 to 50 degrees latitude bin is 398 nT, compared to 137 nT from trackline data. This result reflects the very heterogeneous spatial distribution of the global observatory network, which includes observatories located on top of large amplitude but small size crustal field anomalies such as basaltic islands. In order to circumvent this limitation, observatory data were selected so that the resulting RMS error on F matches the one obtained from trackline data in the 10 to 50 degrees latitude bin. This bin is where the external field is expected to have its smallest contribution to trackline data and where most data are available. A robust outlier detection algorithm was used to achieve this observatory selection, leading to the selection of 67 out of 100 observatories in the 10 to 50 degrees bin, and a total of 113 out of 162 observatories for all latitudes. The final, weighted RMS error values for each component are given in Table 11.

Table 11: RMS differences between observatory data and WMM for years 2000-2014, after selection of observatories such that the RMS error on F is the same as that from trackline data in the 10 to 50 degrees geomagnetic latitude bin.

| Row | | X (nT) | Y (nT) | Z (nT) | H (nT) | F (nT) | I (°) | D (°) | GV (°) |
|-----|--|-----------|-----------|-----------|-----------|-----------|----------|----------|-----------|
| 1 | RMS differences from 113 out of 162 observatories at all latitudes | 152 | 88 | 154 | 152 | 140 | 0.21 | 0.36 | 0.71 |

3.2.4 CRUSTAL FIELD AND SECULAR VARIATION CONTRIBUTIONS – METHOD #2

World Magnetic Models/World Chart Models since 1980 (the first time charts were produced jointly between U.K. and U.S.) were compared with compilations of ground-based vector data. Each of the seven models comprises main-field coefficients at a base epoch and predictive secular variation coefficients valid for the following five years. Two data compilations were used in the comparison: (1) repeat station and land survey data and (2) observatory annual means. Both compilations are from the World Data Centre for Geomagnetism (Edinburgh) and have only modest contamination from external fields, as data are mostly reduced to quiet night time or annual mean equivalents in (1) and annual averaging smooths out much of the

unwanted signal in (2). The reason for going so far back in time was to achieve a better spatial coverage. This is still far from ideal but is shown in Figure 10.

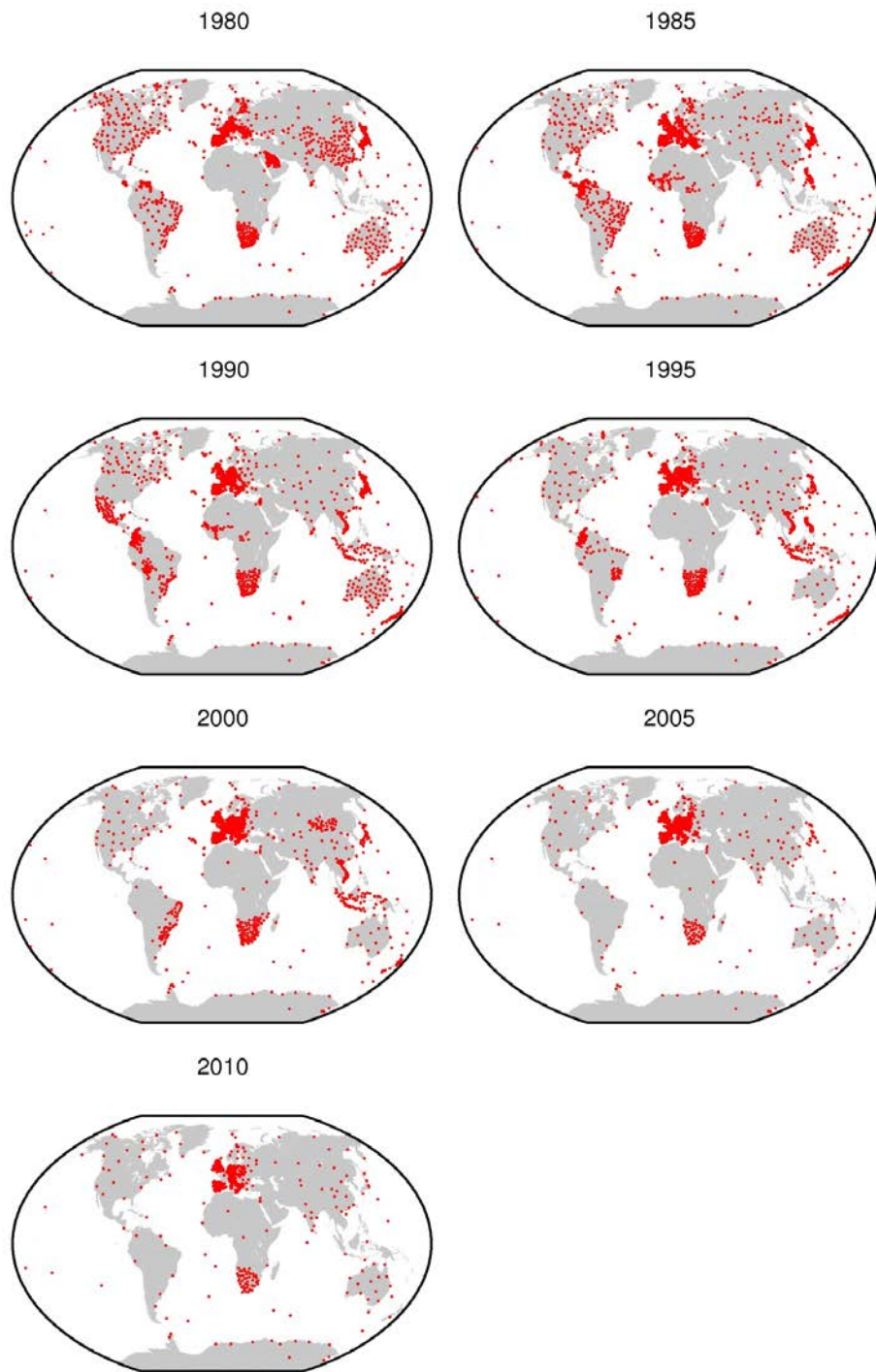


Figure 10: The locations of repeat stations, vector land surveys and observatories providing data used in the comparisons with the seven models.

RMS differences were computed for all seven elements, and for each of the seven models after elimination of outliers (any differences greater than 3 standard deviations). The sample

sizes vary according to the element but are in the range 15000-18000. Table 12 lists these RMS differences.

Table 12: RMS differences between observations and models in World Magnetic Model series.

| | Sample sizes (all/>55° for GV) | X (nT) | Y (nT) | Z (nT) | H (nT) | F (nT) | I (°) | D (°) | GV (°) |
|--|--|-------------------|-------------------|-------------------|-------------------|-------------------|------------------|------------------|-------------------|
| Repeat stations plus observatories 1980 onwards | 15013- 17987/10581 | 187 | 134 | 281 | 168 | 201 | 0.32 | 0.66 | 0.75 |
| Rescaled according to information from EMAG2 and GEODAS | | 113 | 81 | 170 | 102 | 121 | 0.20 | 0.40 | 0.46 |

The contribution to the overall error budget for the WMM from the crustal field estimated here using vector data collected on land is conservative, i.e. over-cautious. One way of justifying the use of lower values is to employ near-surface scalar data, i.e., total intensity. These data are plentiful as they are relatively easy to collect from ships and aircraft and, importantly, they cover both land and sea. Global scalar anomaly compilations have been made in recent years, for example the World Digital Magnetic Anomaly Map (WDMAM) and EMAG2 (Maus et al., 2009). The mean absolute differences for F derived from the land-based vector observations can be compared with those from global compilations. For WDMAM (version A without anomalies estimated from a sea-flooring spreading model) the mean absolute anomaly in F is 98 nT and for EMAG2 it is 105 nT. These are likely to be underestimates at the Earth's surface because these compilations are above the surface at 5 km and 4 km, respectively. However, even if these were to be downward-continued to the Earth's surface they would not be as high as the value from the repeat stations and observatories (201 nT).

Another source of scalar data is NOAA's GEODAS (GEOphysical DAta System), as described in [section 3.2.3](#). For 2000 onwards the spatial distribution of these data is not as good as that of the WDMAM and EMAG2, but they are collected at the Earth's surface. The RMS difference between these data and the relevant WMM is 137 nT.

The values from the repeat stations and observatories are scaled according to the mean of the RMS difference from EMAG2 and the GEODAS surveys (121 nT) and are shown in Table 12.

3.2.5 DISTURBANCE FIELD CONTRIBUTION

The disturbance field is the sum of the contributions of ionospheric and magnetospheric electric currents, plus the corresponding contributions from currents induced by the external time-varying magnetic fields in the Earth and oceans. The strength of the disturbance field is modulated by the 11-year solar cycle. Periods of strong magnetic activity (magnetic storms) occur primarily at solar maximum, although they tend to lag behind the solar cycle by about two years. The epoch of WMM2015 starts in the most active part of the solar cycle and extends into its quietest part.

The contribution from the disturbance field to the WMM uncertainty was estimated from hourly mean values recorded at 162 magnetic observatories over 2000-2014 (see [section 3.2.3](#)). RMS residuals between the data and the cubic spline fit over 2000-2014 were calculated for each observatory and each component. The obtained variation with latitude (Figure 11) is in good agreement the known properties of the external field. Near the geomagnetic equator, the northern external field is enhanced by the so-called equatorial electrojet, a strong electrical current flowing at 110 km altitude along the equator. At higher latitudes, near 65° geomagnetic latitude, intense auroral electrojets can lead to variations as large as several thousands of nT during geomagnetic storms. However, on average, the contribution of the external field to the total error is much smaller than that of the crustal field and for this reason its latitude dependency is neglected in what follows. The global RMS error values for each component are given in Table 13.

Table 13: RMS residuals, attributed to the external field, between observatory data and spline fits for each component and for the years 2000-2014.

| Row | | X (nT) | Y (nT) | Z (nT) | H (nT) | F (nT) | I (°) | D (°) | GV (°) |
|-----|---|-----------|-----------|-----------|-----------|-----------|----------|----------|-----------|
| 1 | RMS external field contribution from 162 observatories at all latitudes | 37 | 25 | 28 | 38 | 30 | 0.04 | 0.27 | 0.52 |

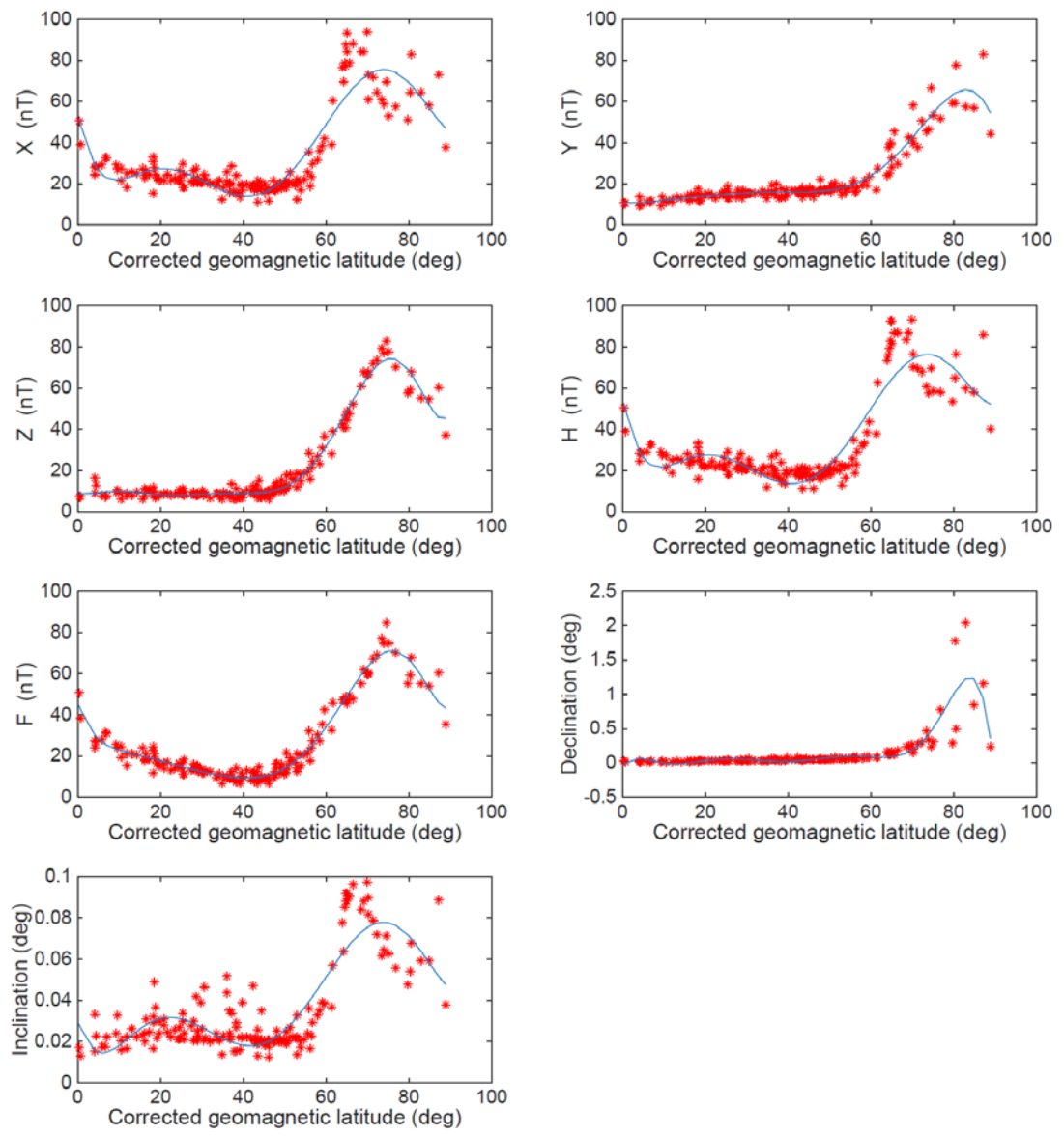


Figure 11: Variation with corrected geomagnetic latitude of the RMS residuals between observatory data and spline fits for the various field components and for the years 2000-2014.

3.3 TOTAL ERROR BUDGET

The results of the error analysis are summarized in Table 14. As the commission error is included in rows 4 and 5, rows 2 and 3 are not taken into account in the total error budget. The two methods used for obtaining the combined crustal field and secular variation contributions have complementary merits and limitations and therefore we averaged both rows to obtain a final estimate for these contributions. Since these errors are statistically independent, the expected total error (row 7) is calculated as the root of the sum of squares of the average of rows 4 and 5 and of row 6. For example, the total error between the observed and modeled declination is estimated to be

$$\sqrt{\left(\frac{0.36 + 0.40}{2}\right)^2 + 0.27^2} = 0.47^\circ \quad (27)$$

The accuracy requirements for the WMM are detailed in the military specification MIL-W-89500 (Defense Mapping Agency, 1993) and are provided in row 1 of Table 14. In summary, the requirement is that the global RMS difference between the WMM and the observed magnetic field at sea level should be within 1° for D and I , within 140 nT for X and Y , within 200 nT for H and Z and within 280 nT for F for the entire 5-year lifetime of the model. In addition, at polar latitudes above 55° , the RMS difference for GV should be within 1° . We find that the actual error values (row 7) are all lower than the required values on average at the Earth's surface.

Table 14: Estimated global RMS errors in WMM2015. Higher values of GV (compared to D) reflect the larger uncertainties of the declination at high latitudes, the only regions where GV is defined.

| Row | | X (nT) | Y (nT) | Z (nT) | H (nT) | F (nT) | I ($^\circ$) | D ($^\circ$) | GV ($^\circ$) |
|-----|--|-----------|-----------|-----------|-----------|-----------|-------------------|-------------------|--------------------|
| 1 | Military specification MIL-W-89500 | 140 | 140 | 200 | 200 | 280 | 1.00 | 1.00 | 1.00 |
| 2 | Formal commission error | 0.9 | 0.8 | 1.3 | 0.9 | 1.3 | 0.0 | 0.0 | 0.0 |
| 3 | Commission error from model comparisons | 39 | 42 | 65 | 41 | 49 | 0.09 | 0.35 | 0.78 |
| 4 | Crustal field and secular variation contributions – method #1 | 152 | 88 | 154 | 152 | 140 | 0.21 | 0.36 | 0.71 |
| 5 | Crustal field and secular variation contributions – method #2 | 113 | 81 | 170 | 102 | 121 | 0.20 | 0.40 | 0.46 |
| 6 | Disturbance field contribution | 37 | 25 | 28 | 38 | 30 | 0.04 | 0.27 | 0.52 |
| 7 | Combined error (average of rows 4 and 5, plus row 6) | 138 | 89 | 165 | 133 | 134 | 0.21 | 0.47 | 0.79 |

3.4 ERROR MODEL

The WMM2015 comes with an error model providing uncertainty estimates for every geomagnetic element (X, Y, Z, H, F, I and D) and every location at the Earth's surface. This model is built upon the results of the error analysis (see [section 3.3](#)), while taking into account the geometrical relationships between the various components [formulas (19) in [section 1.2](#)].

The first part of the error model was built by taking the values obtained in the last row of Table 14 as variances of the X, Y and Z components, and assuming that off-diagonal terms of the variance-covariance matrix for (X, Y, Z) are zero:

$$\delta X = 138 \text{ nT} \quad (28)$$

$$\delta Y = 89 \text{ nT} \quad (29)$$

$$\delta Z = 165 \text{ nT} \quad (30)$$

The error in (X, Y, Z) was then propagated onto (F, I, D, H) by linearizing the relationships (19) between (F, I, D, H) and (X, Y, Z) and neglecting the off-diagonal terms:

$$\delta H = \sqrt{[(\delta X)^2(\cos D)^2 + (\delta Y)^2(\sin D)^2]} \quad (31)$$

$$H \delta D = \sqrt{[(\delta X)^2(\sin D)^2 + (\delta Y)^2(\cos D)^2]} \quad (32)$$

$$\delta F = \sqrt{[(\delta H)^2(\cos I)^2 + (\delta Z)^2(\sin I)^2]} \quad (33)$$

$$F \delta I = \sqrt{[(\delta H)^2(\sin I)^2 + (\delta Z)^2(\cos I)^2]} \quad (34)$$

In order to remove non-physical variations in $\delta H, \delta F$ and δI , these quantities were averaged over the WGS84 ellipsoid yielding:

$$\delta H = 133 \text{ nT} \quad (35)$$

$$\delta F = 152 \text{ nT} \quad (36)$$

$$\delta I = 0.22^\circ \quad (37)$$

These values are remarkably close to the error budget values (Table 14), which suggests that the error analysis is consistent.

The case of δD is different, as H goes to zero at the North and South magnetic poles and therefore δD goes to infinity there. Adopting a global average for δD would thus seriously

underestimate the declination error near the poles. To address this difficulty, the following formula was built:

$$\delta D = \sqrt{(0.23)^2 + (5430/H)^2} \quad (38)$$

where δD is expressed in degrees. This formula is such that:

- (1) At low-latitudes (i.e., for large H values), δD is close to the propagated δD averaged over all locations where $H \geq 5000$ nT (i.e., excluding areas where δD becomes very large due to the geometrical effect), which is equal to 0.26° . Specifically, 0.23° is obtained by taking $\sqrt{(0.26)^2 - (5430/41636)^2}$, so that $\delta D = 0.26^\circ$ where $H = 41636$ nT (maximum value at the Earth's surface).
- (2) Near the poles (i.e., for small H values), δD varies like the global average of the propagated $H \delta D$, which is equal to 5430 nT, divided by H .

[Note that the formula used in the WMM2015 software, online calculators and webpage released on Dec 15, 2014 is slightly different as it was calculated by averaging quantities over the sphere instead of the ellipsoid. Formula (38) then becomes $\delta D = \sqrt{(0.24)^2 + (5432/H)^2}$.]

A global map of the corresponding declination error is provided in Figure 12. As can be seen on this map, the error is lower than the error budget value of 0.47° (Table 14) at mid- to low-latitudes, while it is larger near the magnetic poles and in an area close to South Africa where the horizontal field is very low. The average value of the D error from equation (38) is equal to 0.39° which is close to the error budget value.

The final error model is thus made of equations (28)-(30) and (35)-(38). The uncertainties in X , Y , Z , H , F and I are assumed to be constant over the globe, while the uncertainty in D is assumed to vary with location. All uncertainties are assumed to be constant with altitude. As D is the most important element for navigation and orientation and as propagating the errors in X , Y and Z to D also does a not unreasonable job in mapping the errors arising from the auroral and polar cap currents, we only consider an error model that varies spatially for D .

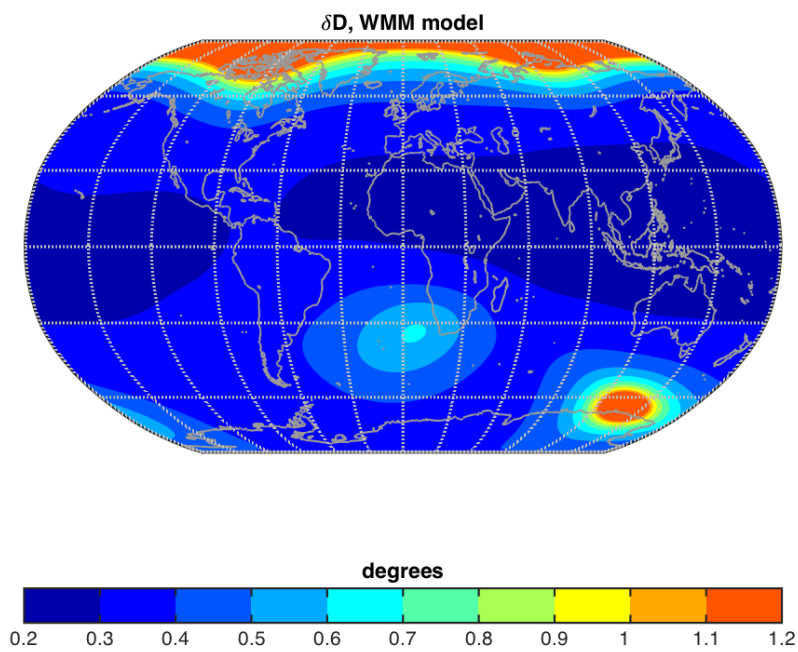


Figure 12: Global distribution of the declination error provided by the WMM2015 error model. The color scale is limited to a maximum value of 1.2° ; the error becomes larger than this near magnetic poles.

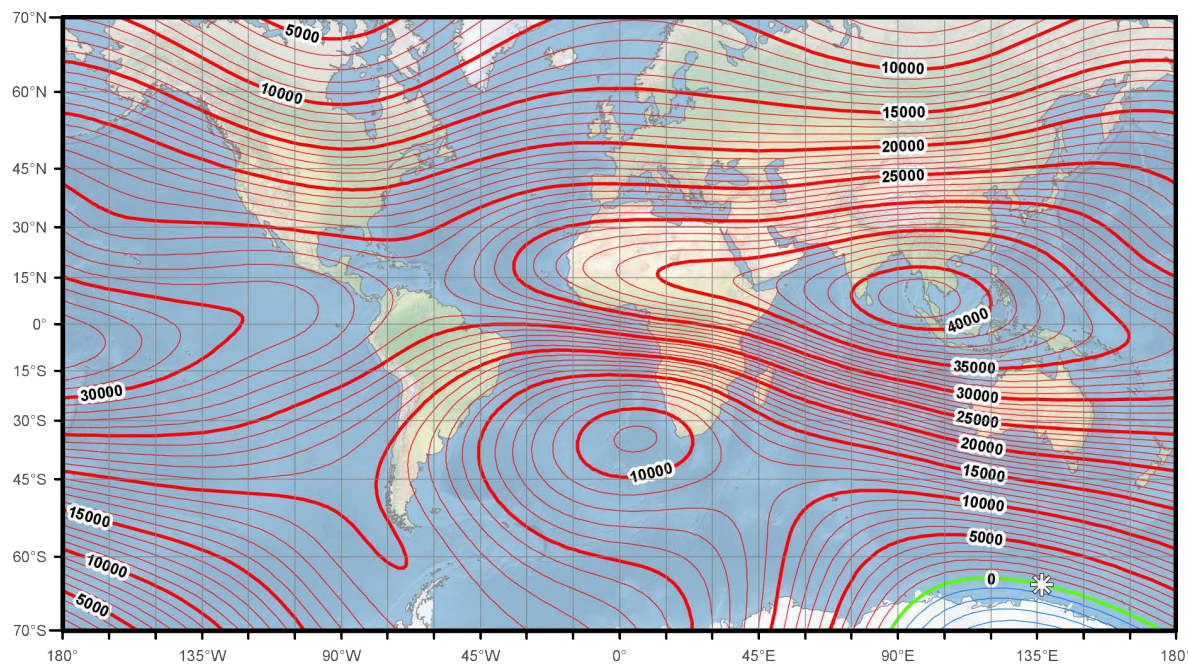
4. CHARTS

This section provides the WMM2015 charts in the following order:

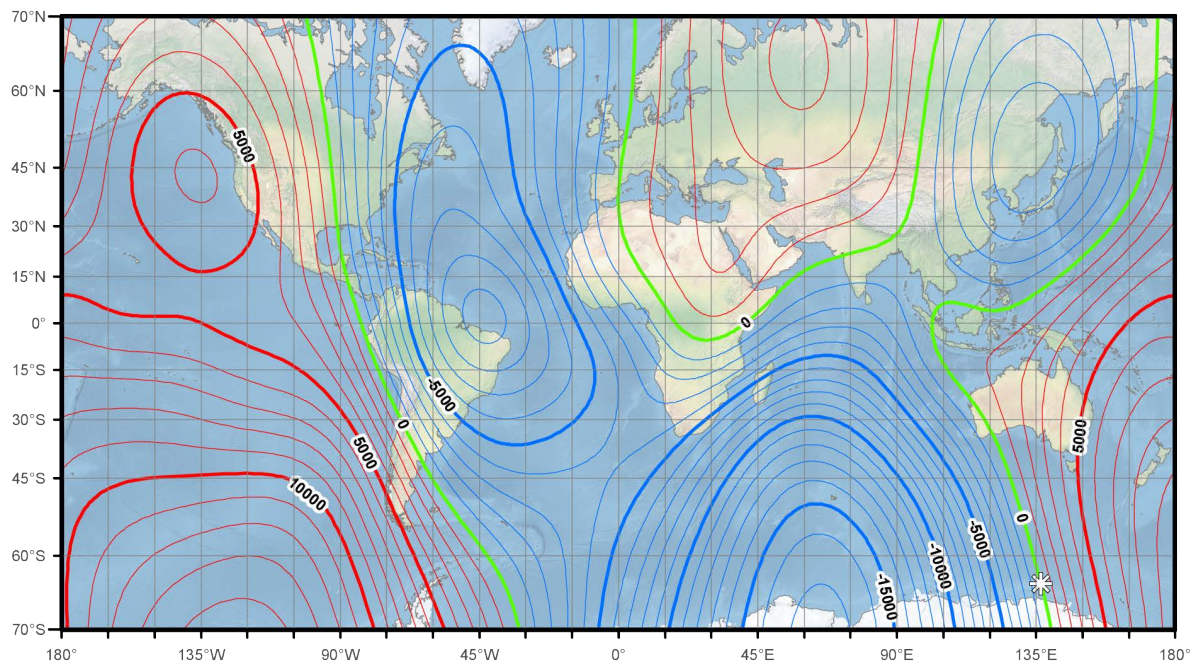
- Main field maps for 2015.0 in Mercator projection for X , Y , Z , H , F , I and D (see pgs. 64-67)
- Main field maps in north polar stereographic projection (see pgs. 68-74)
- Main field maps in south polar stereographic projection (see pgs. 75-81)
- Secular variation maps for 2015.0 – 2020.0 in Mercator projection for X , Y , Z , H , F , I and D (see pgs. 82-85)
- Secular variation maps in north polar stereographic projection (see pgs. 86-92)
- Secular variation maps in south polar stereographic projection (see pgs. 93-99)
- Gravitation maps (see pgs. 100-103)
- Geomagnetic longitude and latitude in Mercator projection (see pg. 104)

The white stars on the maps indicate the 2015.0 positions of the dip poles.

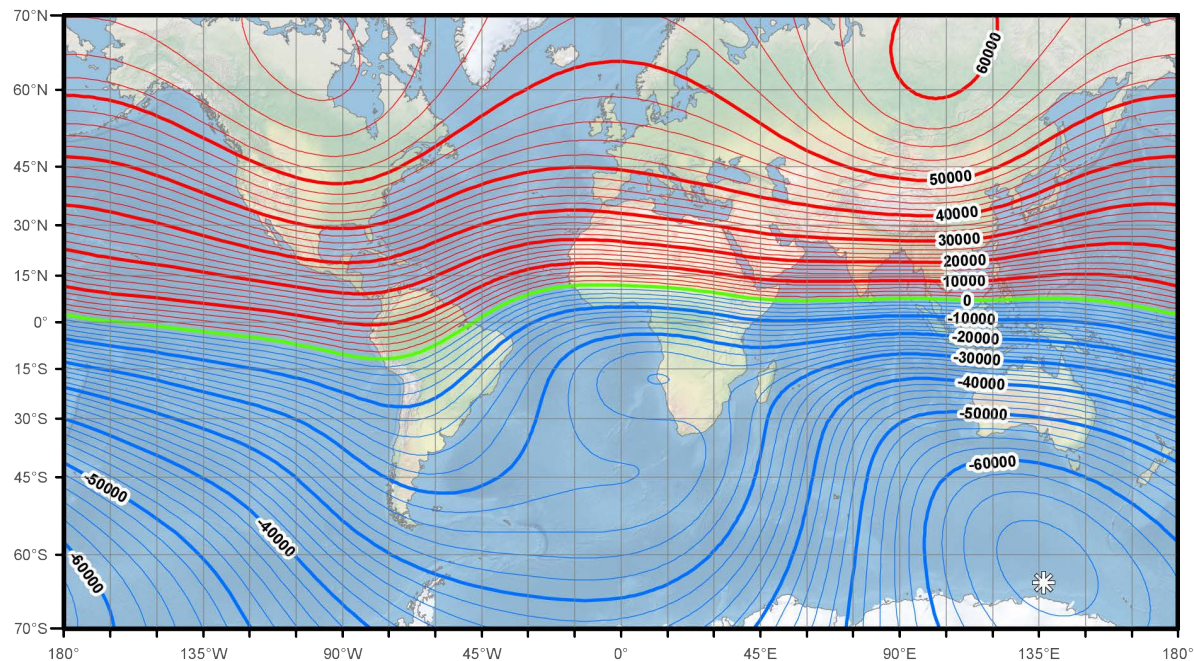
MAIN FIELD MAPS: MERCATOR PROJECTION



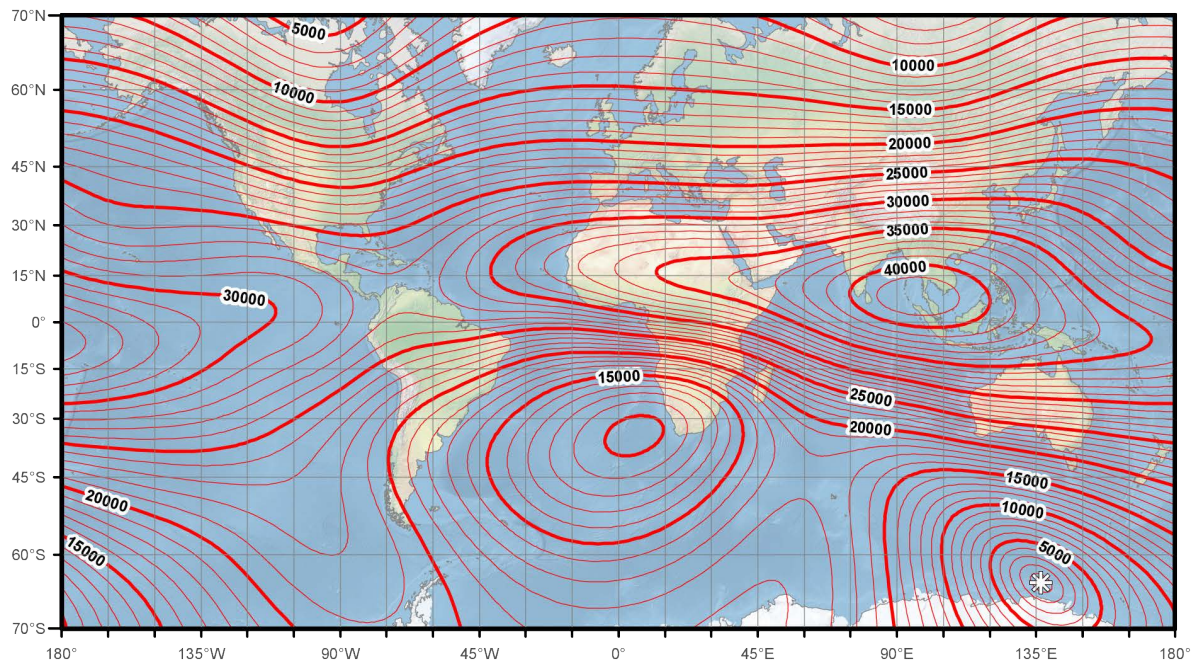
Main field north component (X). Contour interval is 1000 nT. Mercator projection.



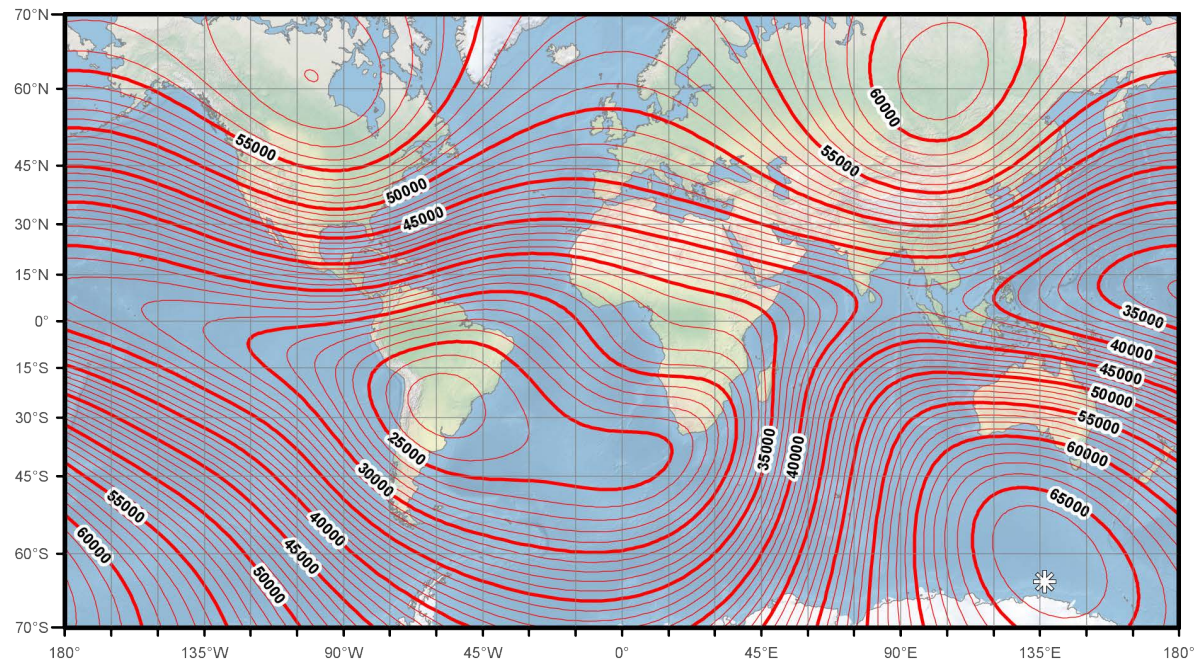
Main field east component (Y). Contour interval is 1000 nT, red contours positive (east); blue negative (west); green zero line. Mercator projection.



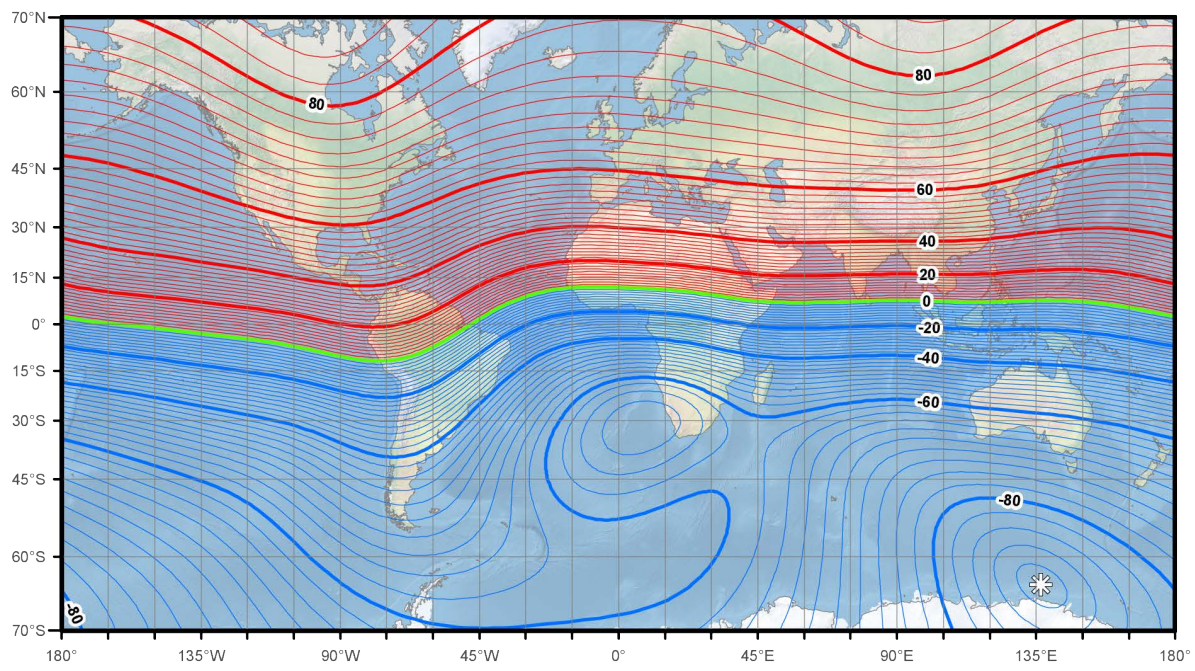
Main field down component (Z). Contour interval is 1000 nT, red contours positive (down); blue negative (up); green zero line. Mercator projection.



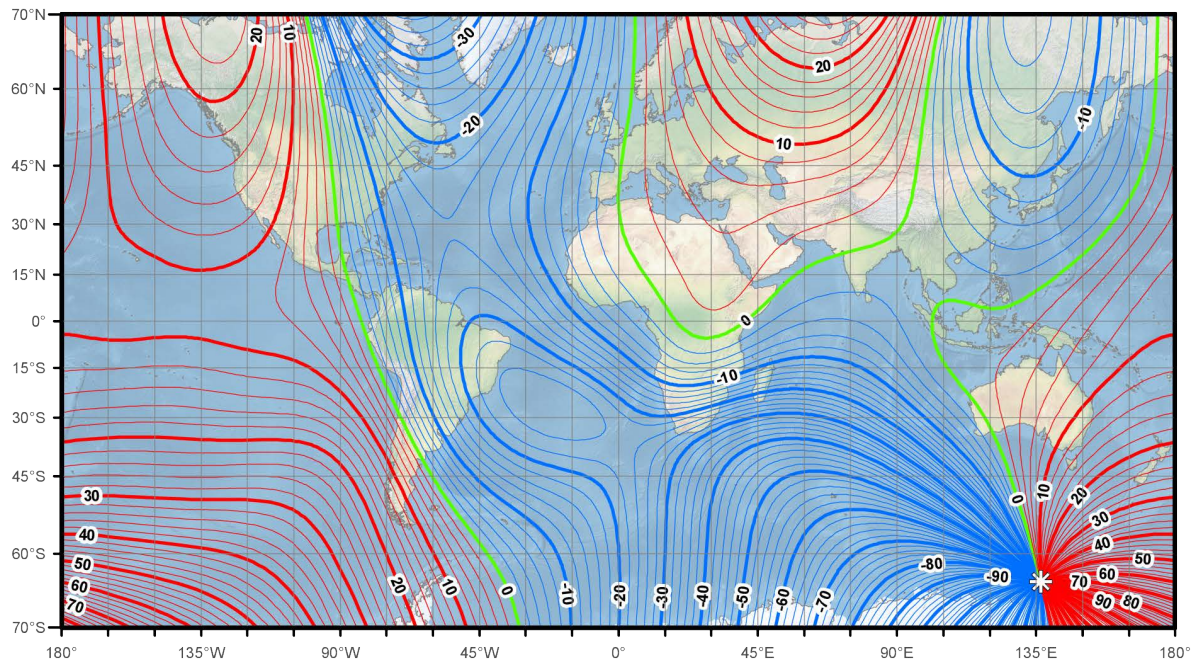
Main field horizontal intensity (H). Contour interval is 1000 nT. Mercator projection.



Main field total intensity (F). Contour interval is 1000 nT. Mercator projection.

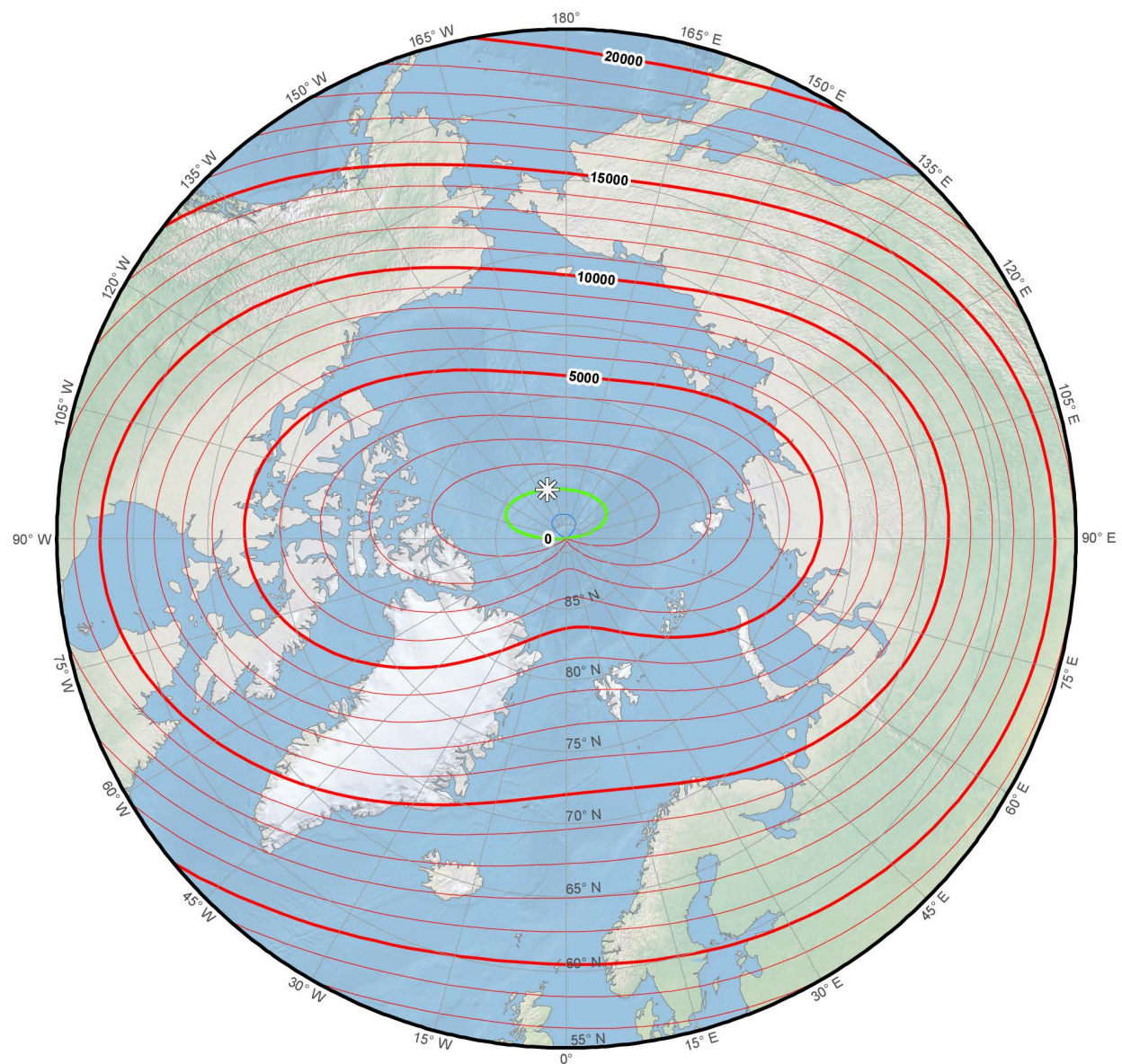


Main field inclination (I). Contour interval is 2 degrees, red contours positive (down); blue contours negative (up); green zero line. Mercator projection.

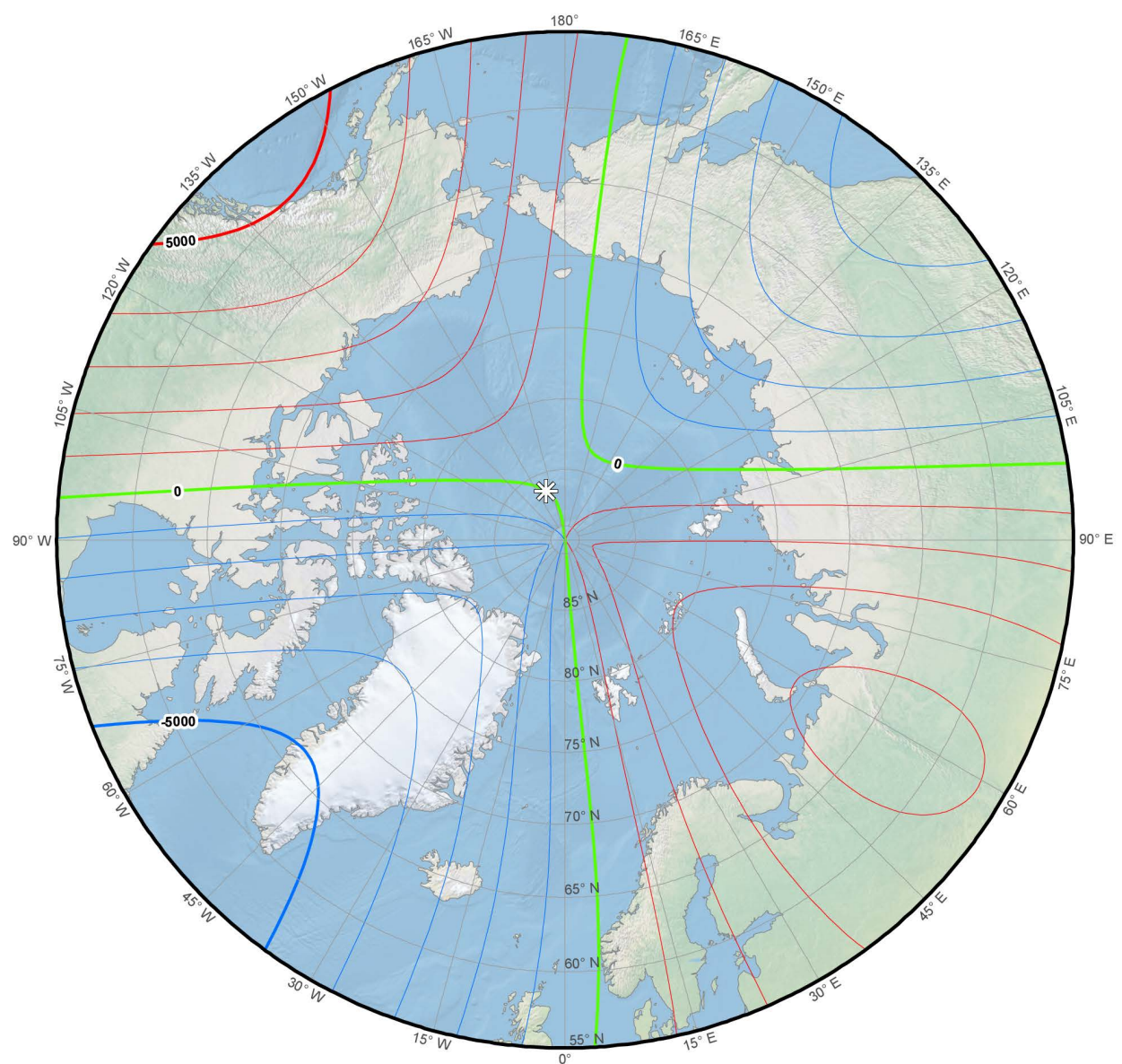


Main field declination (D). Contour interval is 2 degrees, red contours positive (east); blue contours negative (west); green zero (agonic) line. Mercator projection.

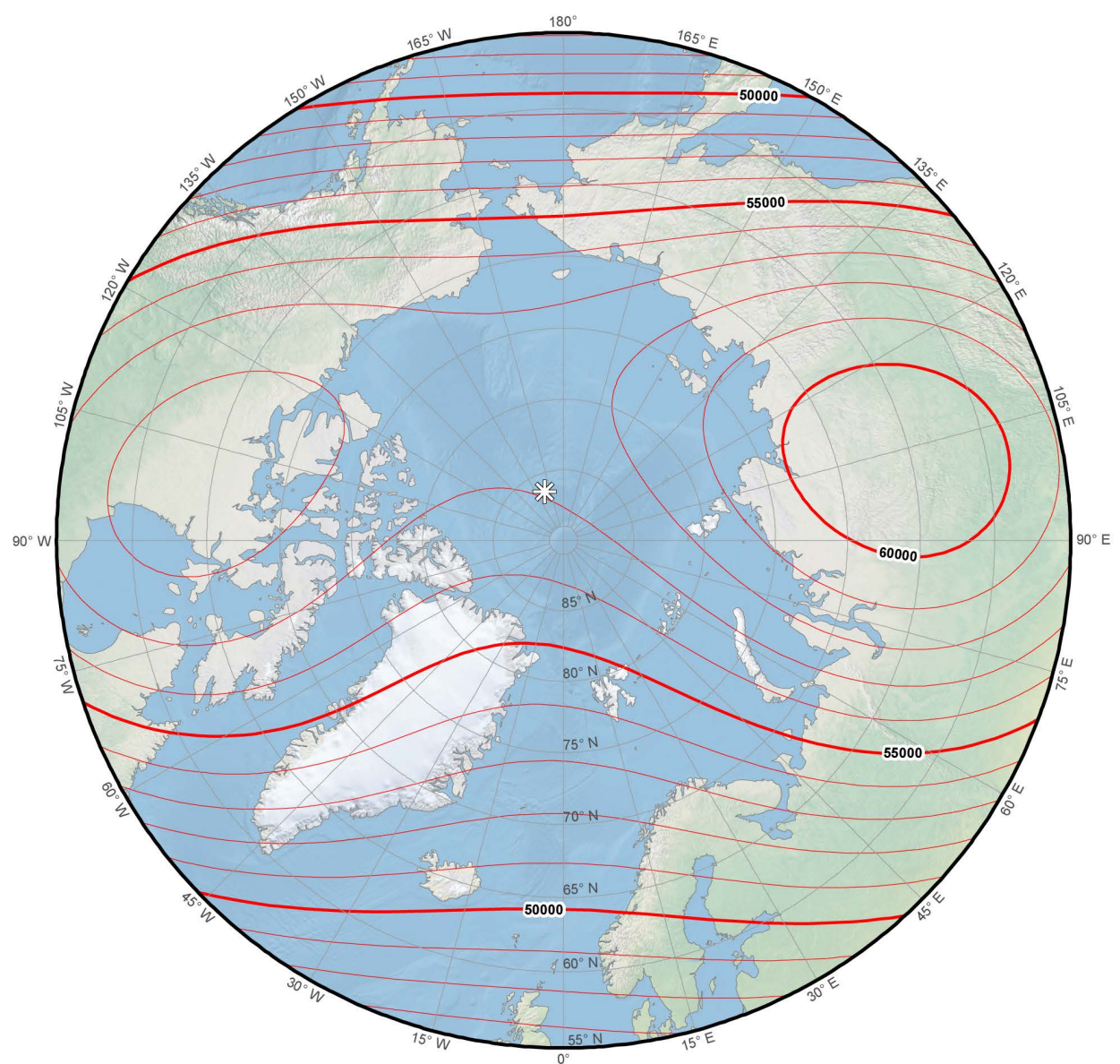
MAIN FIELD MAPS: NORTH POLAR STEREOGRAPHIC PROJECTION



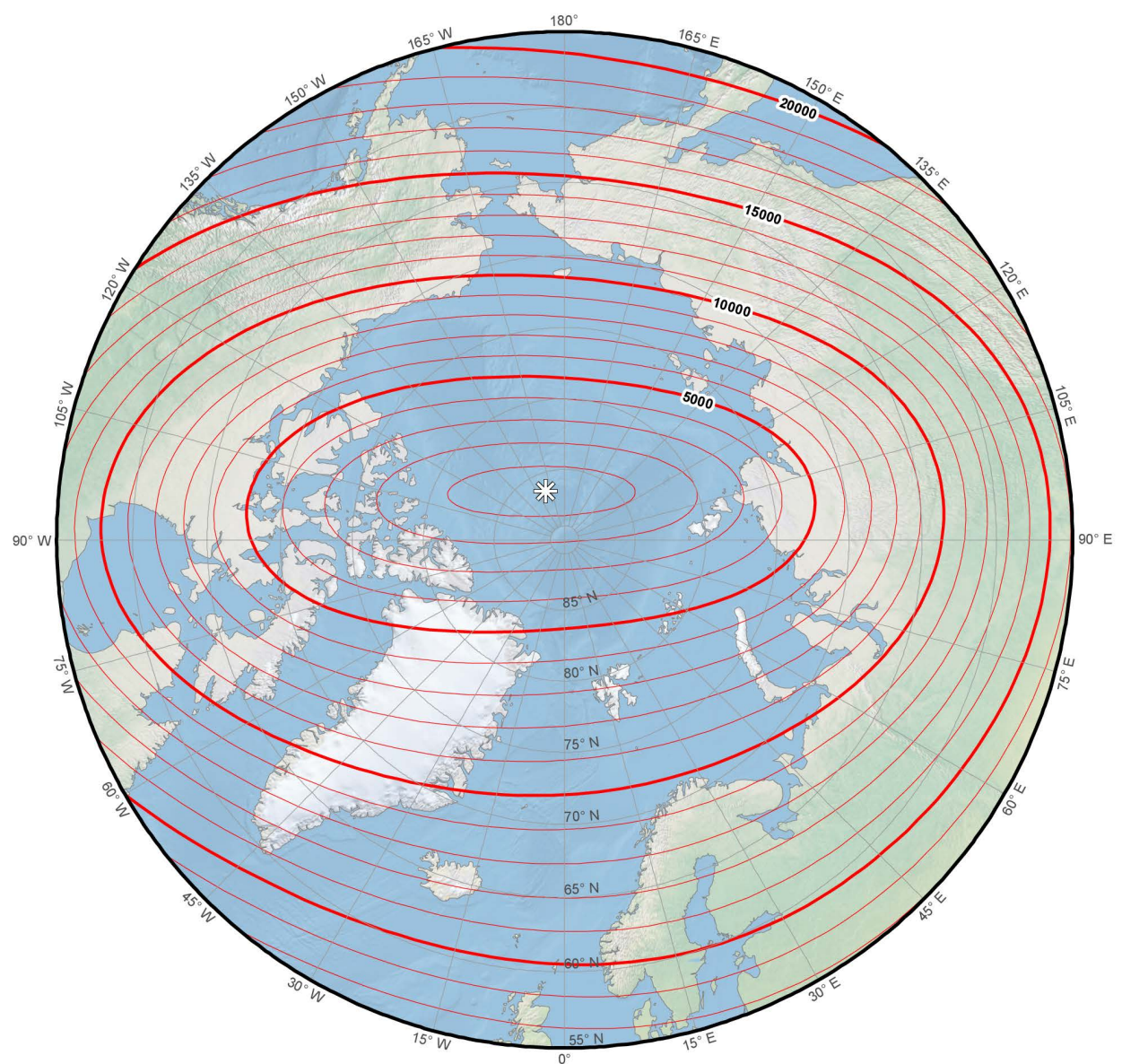
Main field north component (X). Contour interval is 1000 nT. North polar region.
Polar Stereographic Projection.



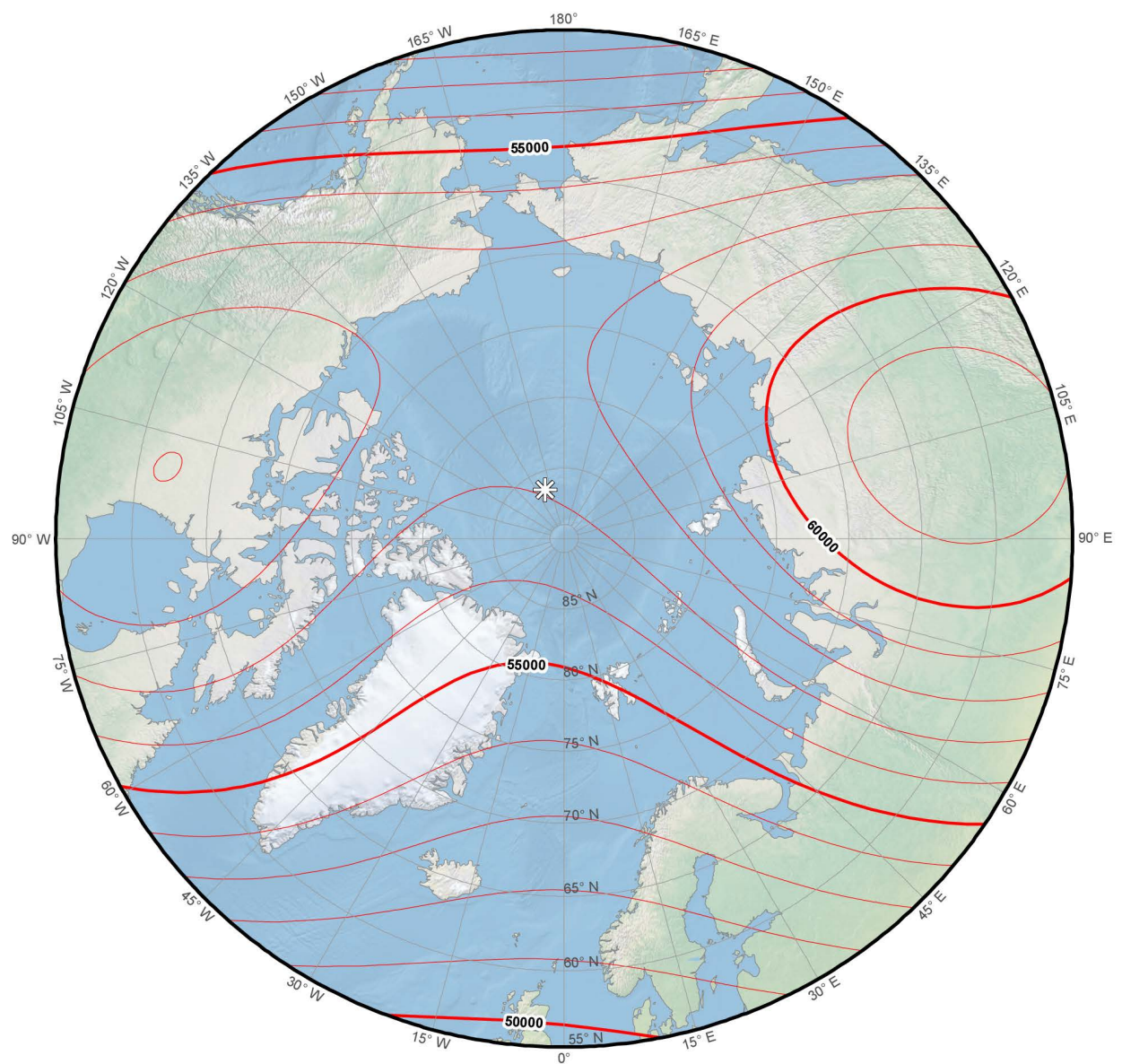
Main field east component (Y). Contour interval is 1000 nT, red contours positive (east); blue contours negative (west); green zero line. North polar region. Polar Stereographic Projection.



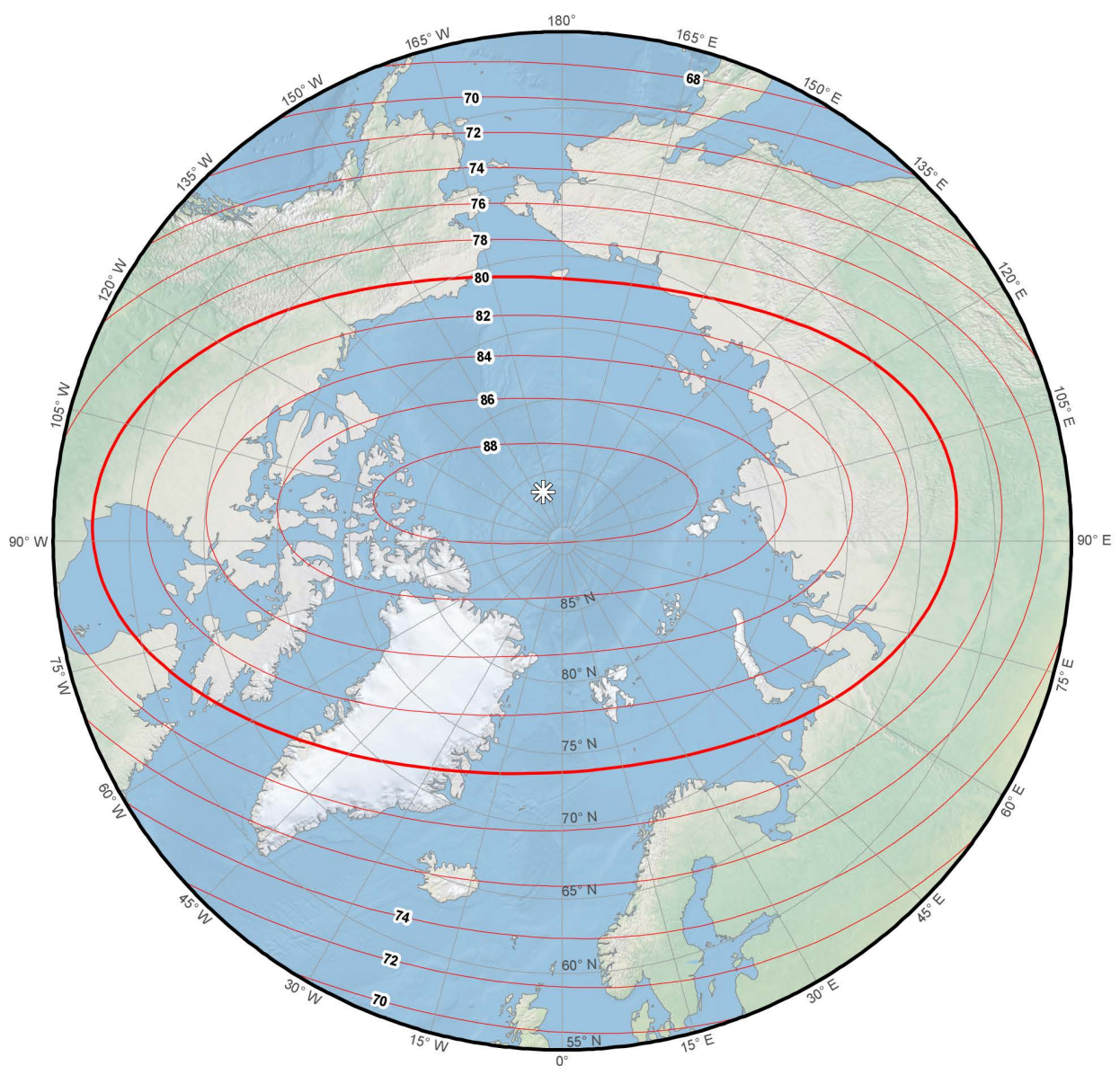
Main field down component (Z). Contour interval is 1000 nT. North polar region.
Polar Stereographic Projection.



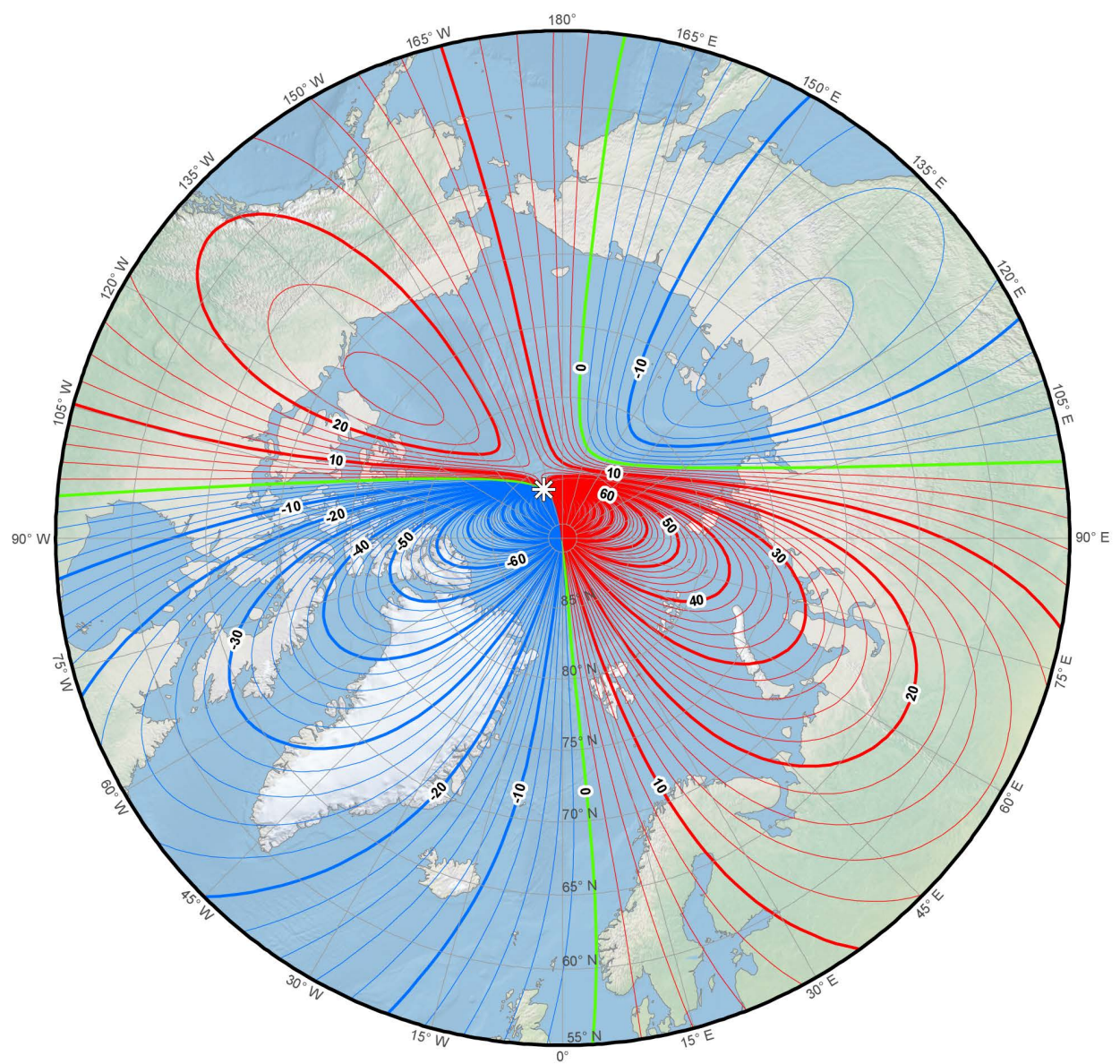
Main field horizontal intensity (H). Contour interval is 1000 nT. North polar region.
Polar Stereographic Projection.



Main field total intensity (F). Contour interval is 1000 nT. North polar region.
Polar Stereographic Projection.

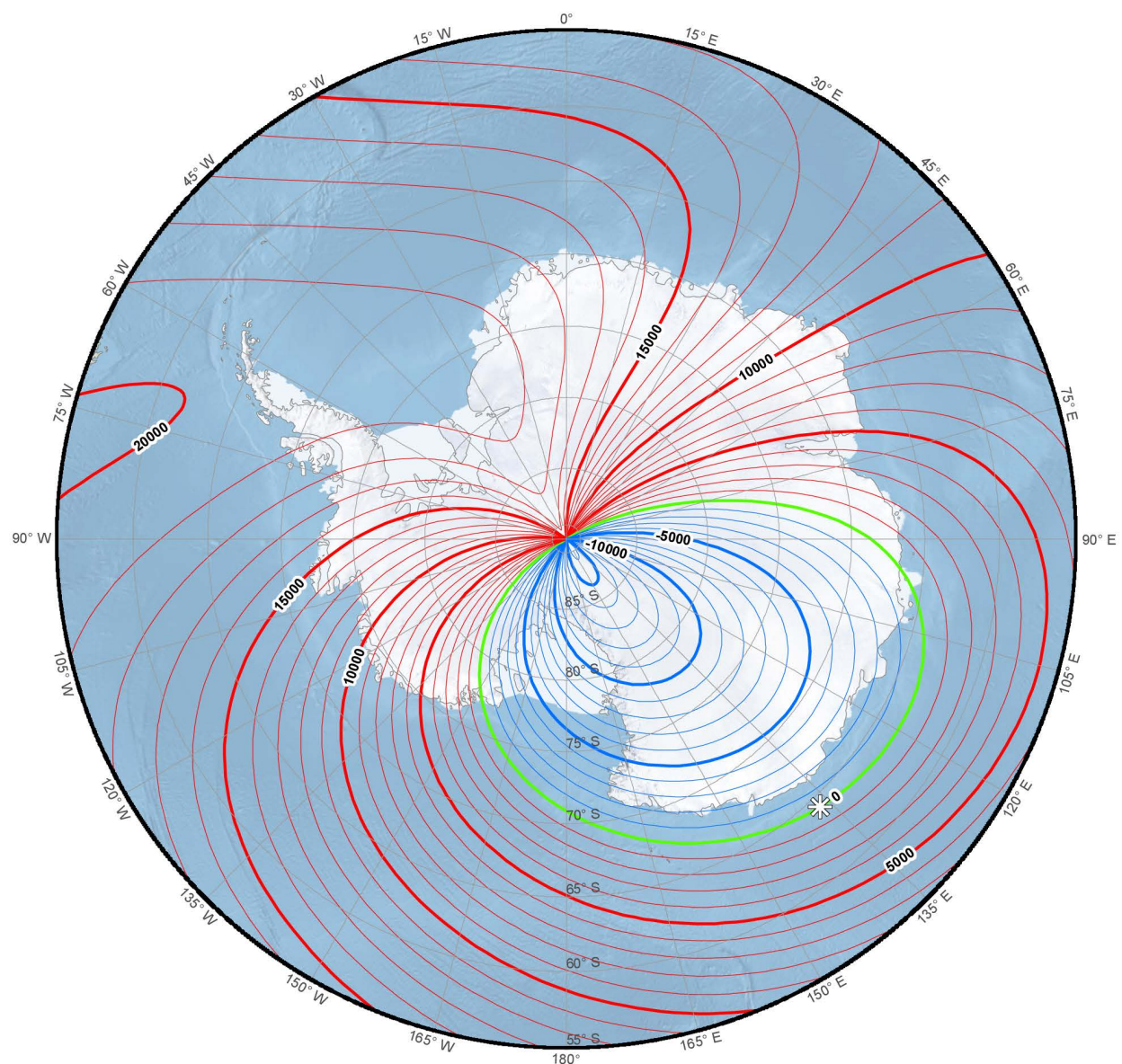


Main field inclination (I). Contour interval is 2 degrees. North polar region.
Polar Stereographic Projection.

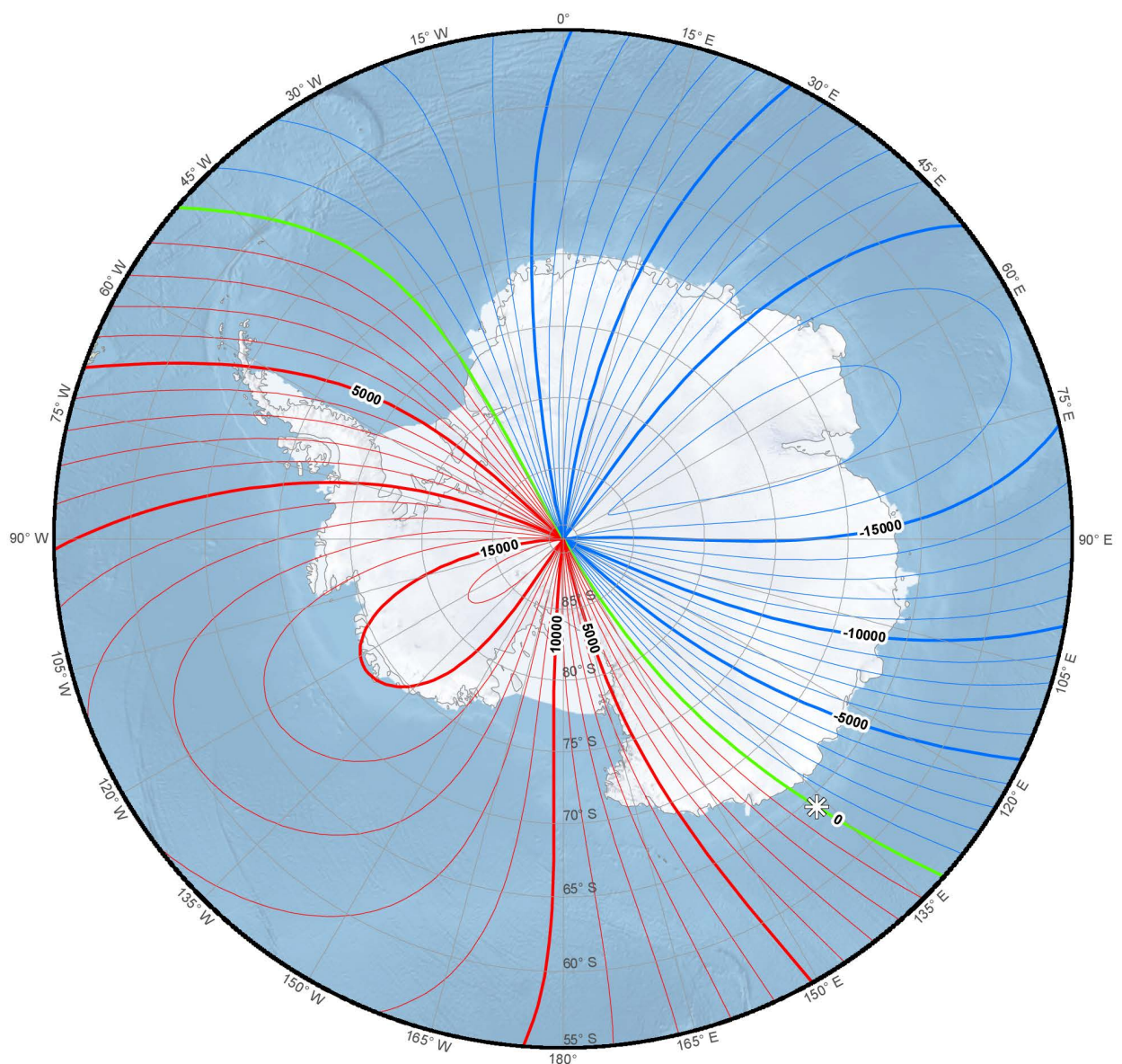


Main field declination (D). Contour interval is 2 degrees, red contours positive (east); blue negative (west); green zero (agonic) line. North polar region. Polar Stereographic Projection.

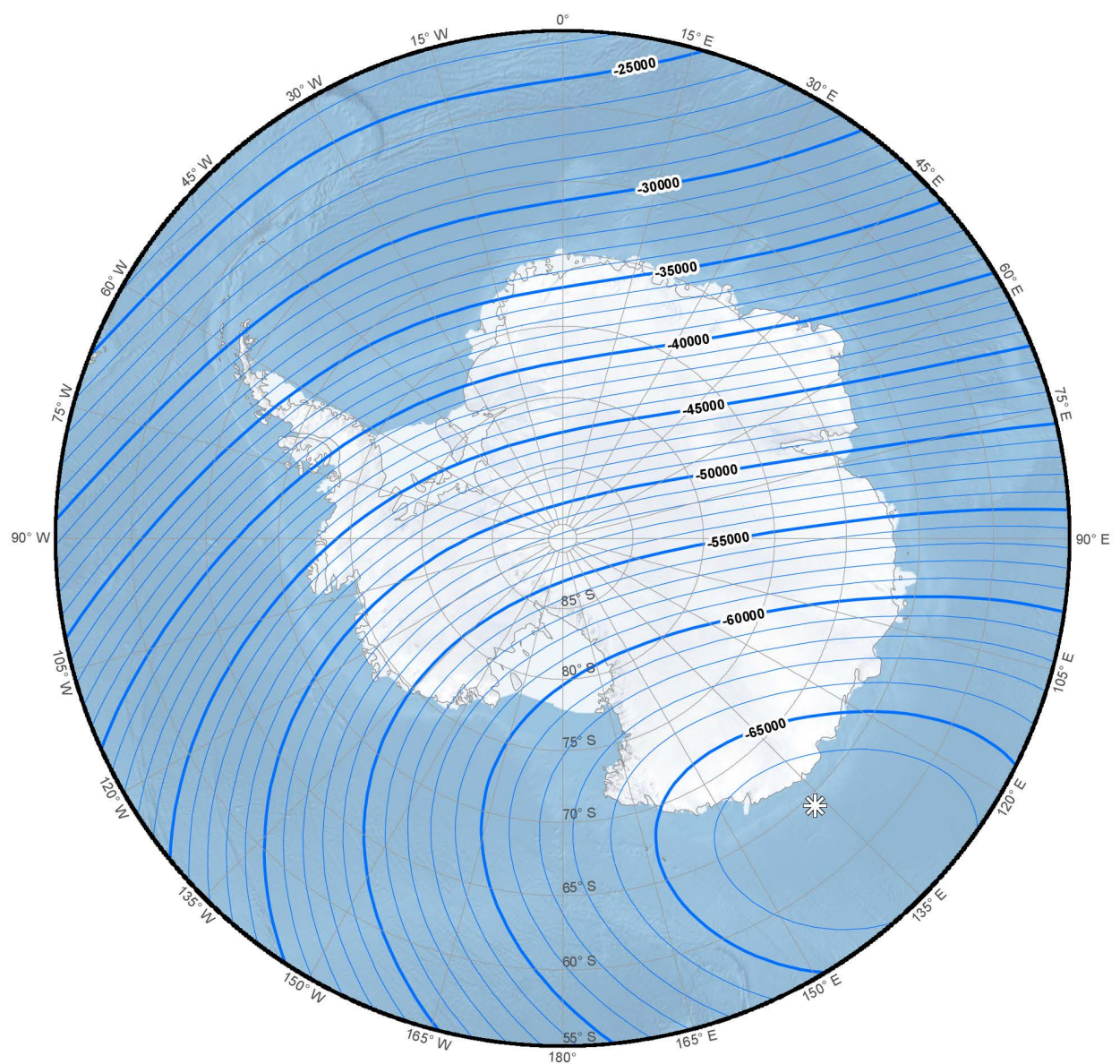
MAIN FIELD MAPS: SOUTH POLAR STEREOGRAPHIC PROJECTION



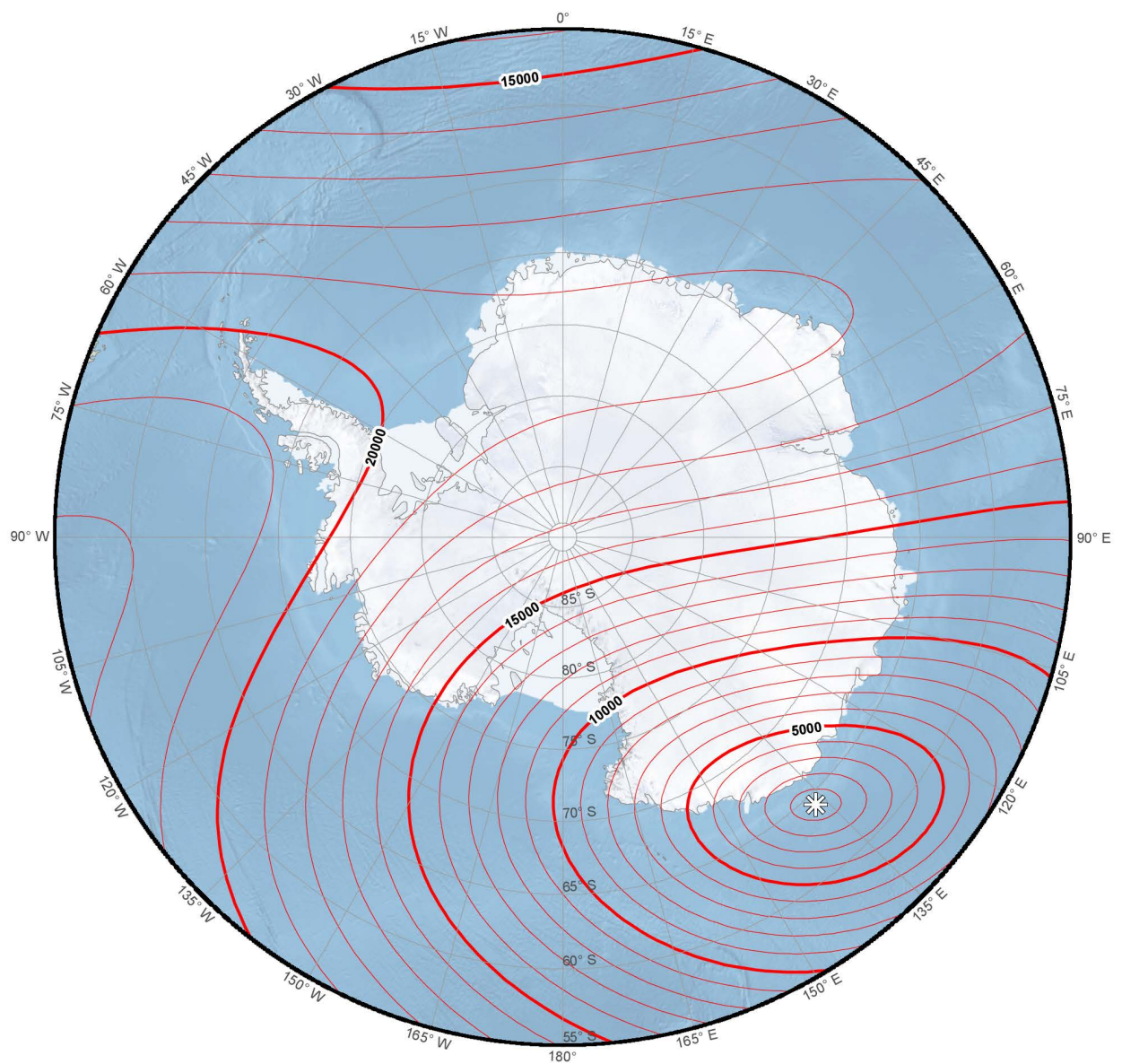
Main field north component (X). Contour interval is 1000 nT, red contours positive (north); blue negative (south); green zero line. South polar region. Polar Stereographic Projection.



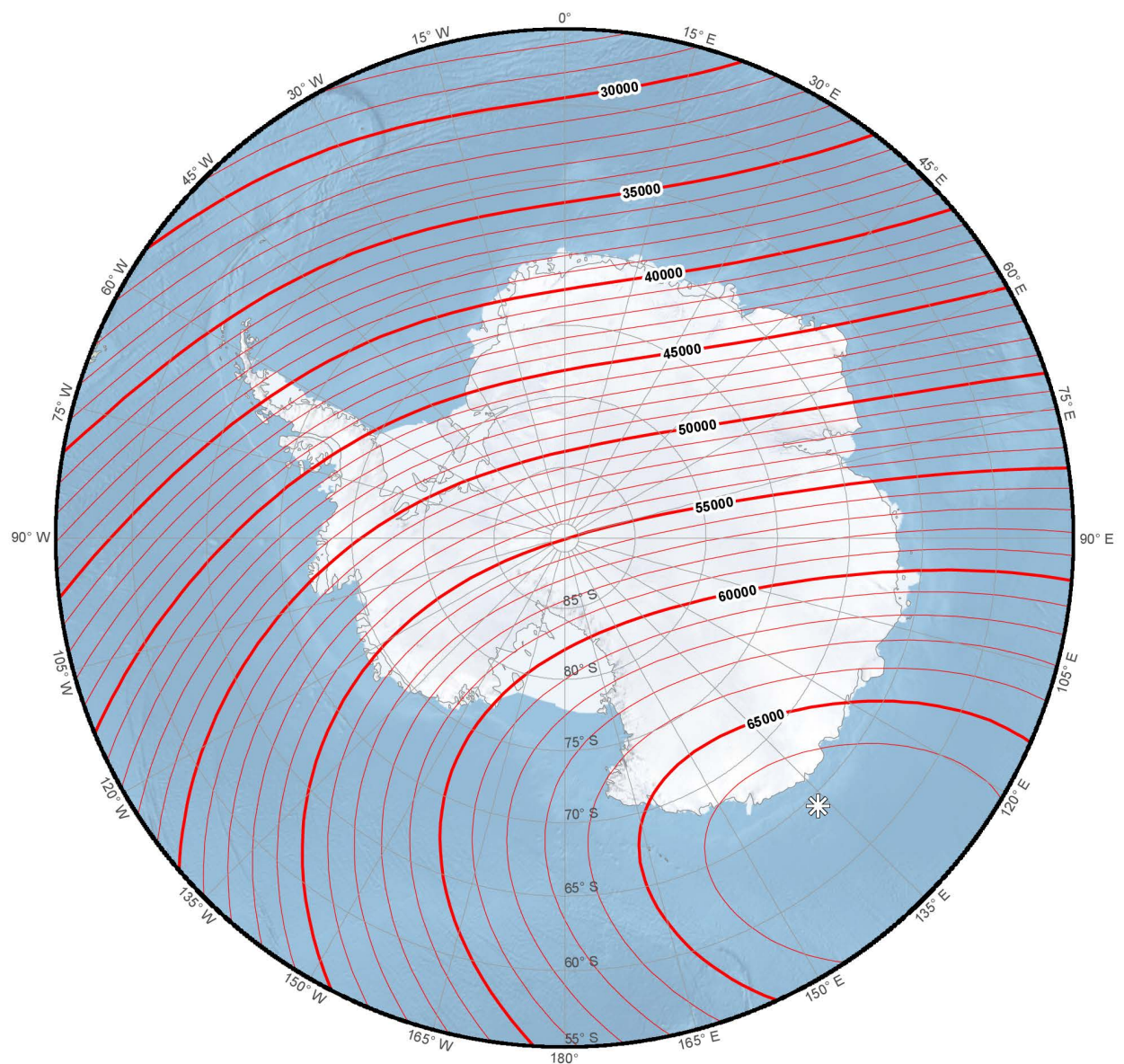
Main field east component (Y). Contour interval is 1000 nT, red contours positive (east); blue negative (west); green zero line. South polar region. Polar Stereographic Projection.



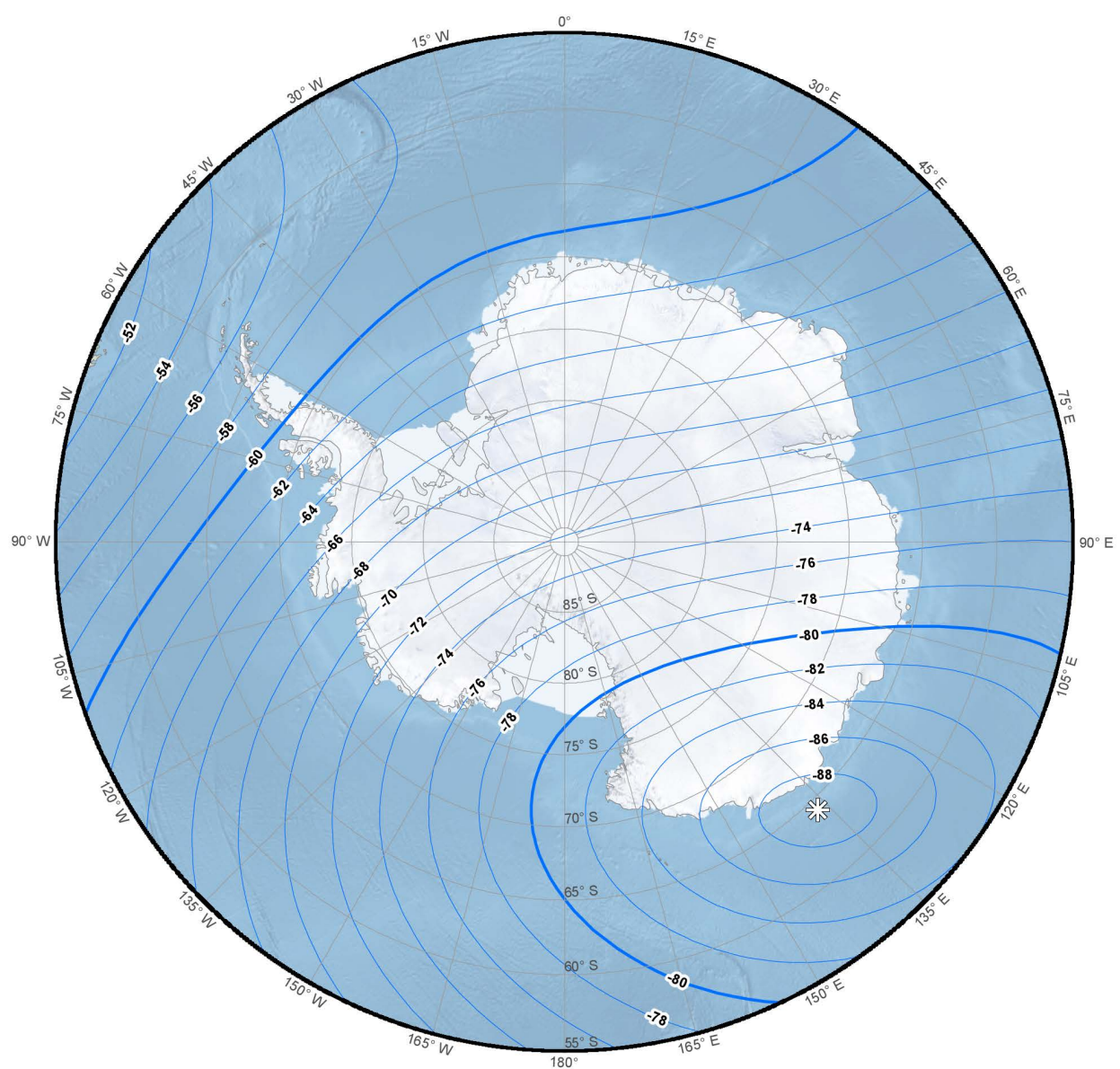
Main field down component (Z). Contour interval is 1000 nT. South polar region.
Polar Stereographic Projection.



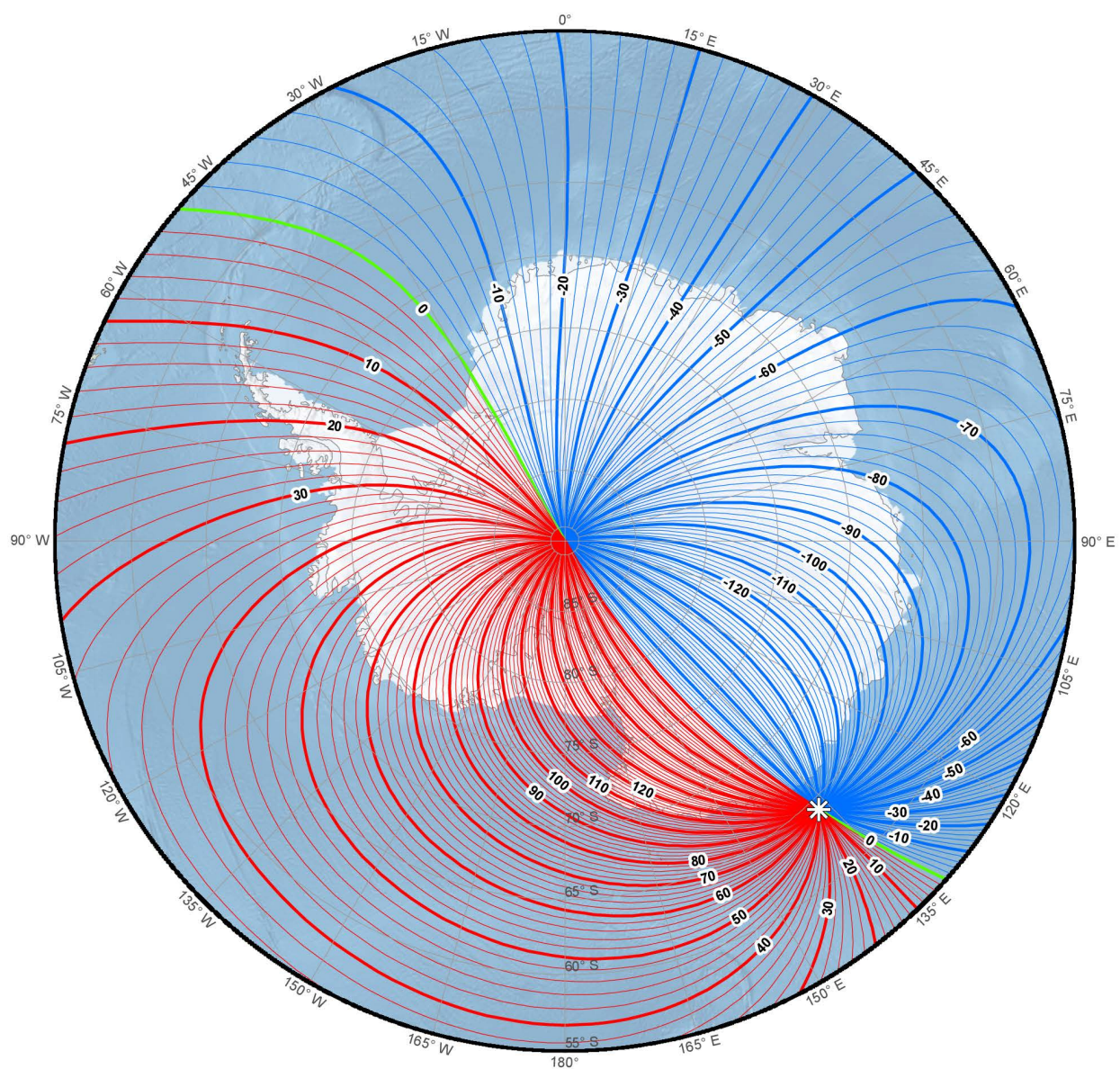
Main field horizontal intensity (H). Contour interval is 1000 nT. South polar region.
Polar Stereographic Projection.



Main field total intensity (F). Contour interval is 1000 nT. South polar region. Polar Stereographic Projection.

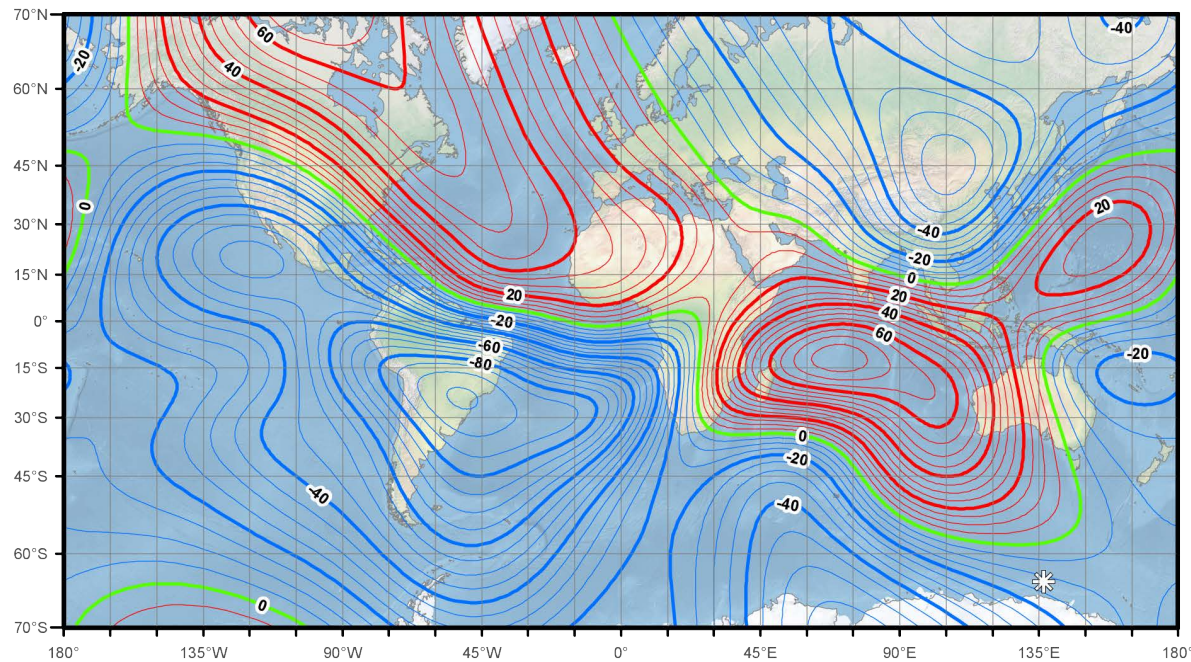


Main field inclination (I). Contour interval is 2 degrees. South polar region. Polar Stereographic Projection.

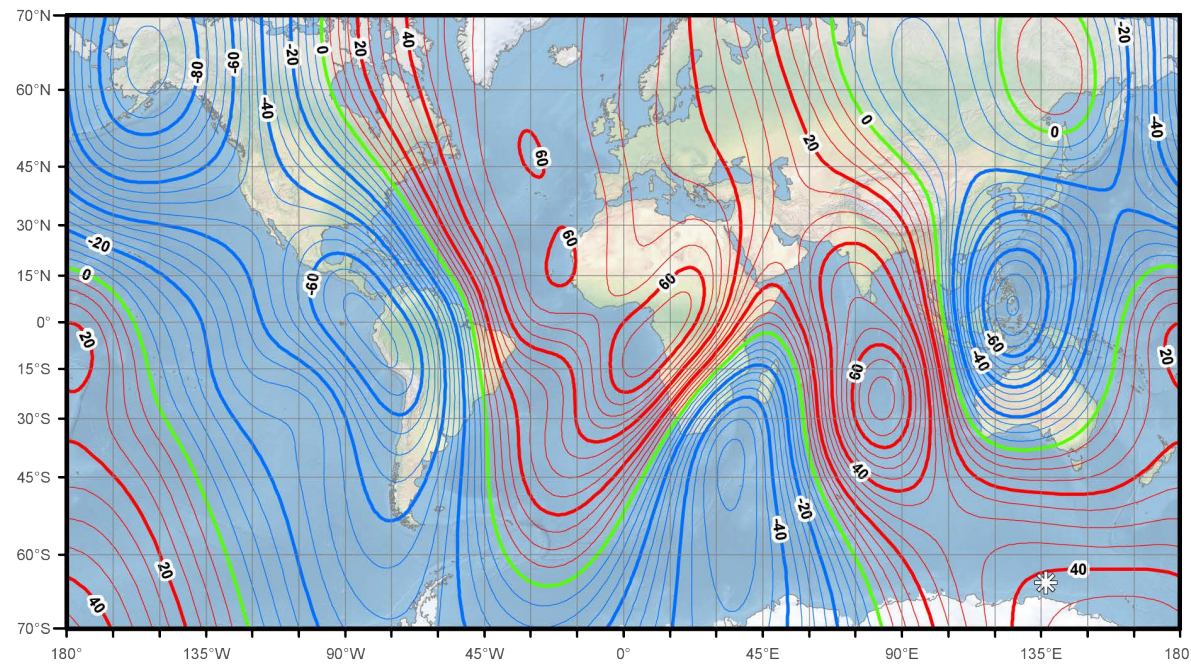


Main field declination (D). Contour interval is 2 degrees, red contours positive (east); blue negative (west); green zero (agonic) line. South polar region. Polar Stereographic Projection.

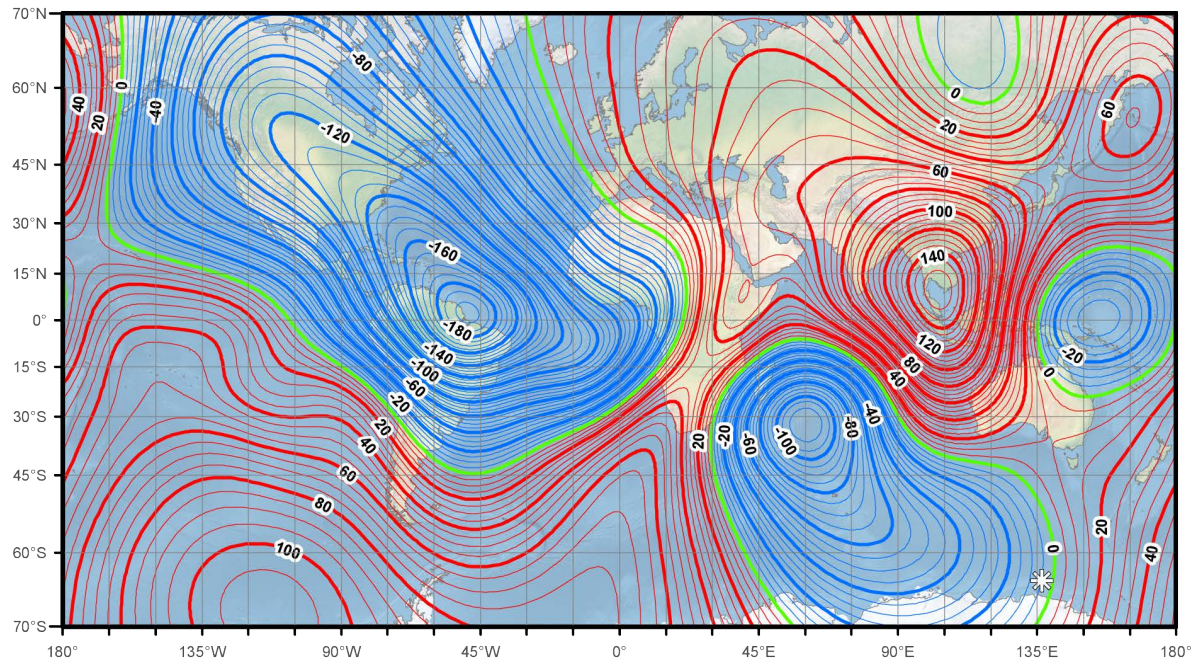
SECULAR VARIATION MAPS: MERCATOR PROJECTION



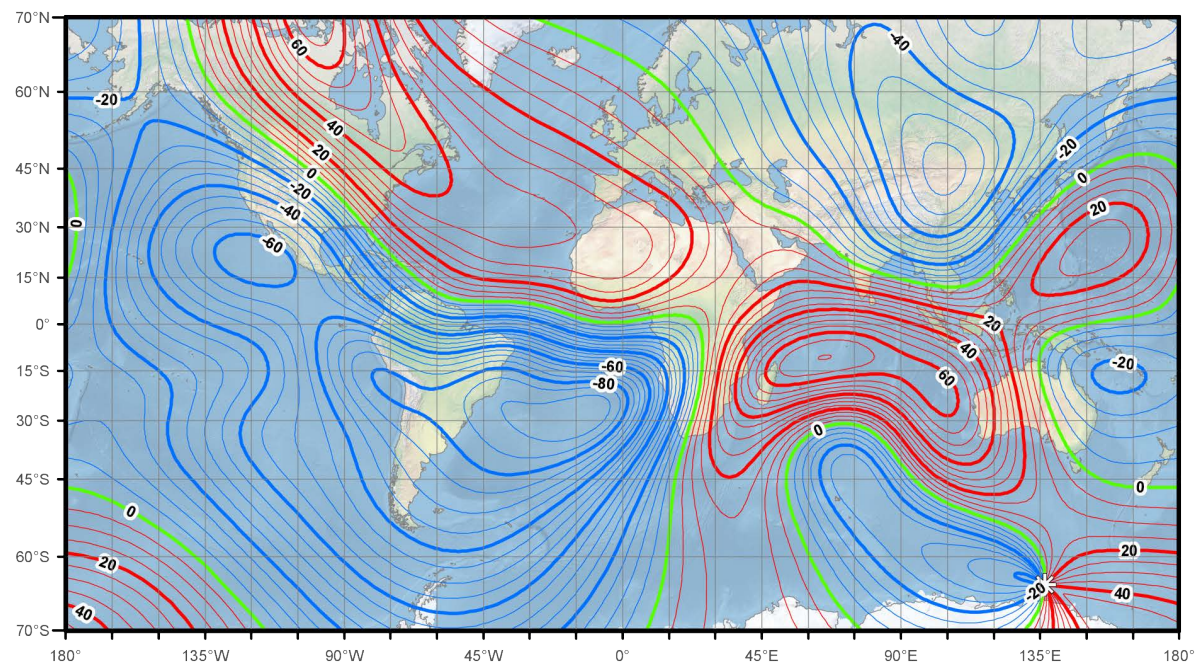
Annual change north component (X). Contour interval is 5 nT / year, red contours positive (north) change; blue negative (south) change; green zero change. Mercator Projection.



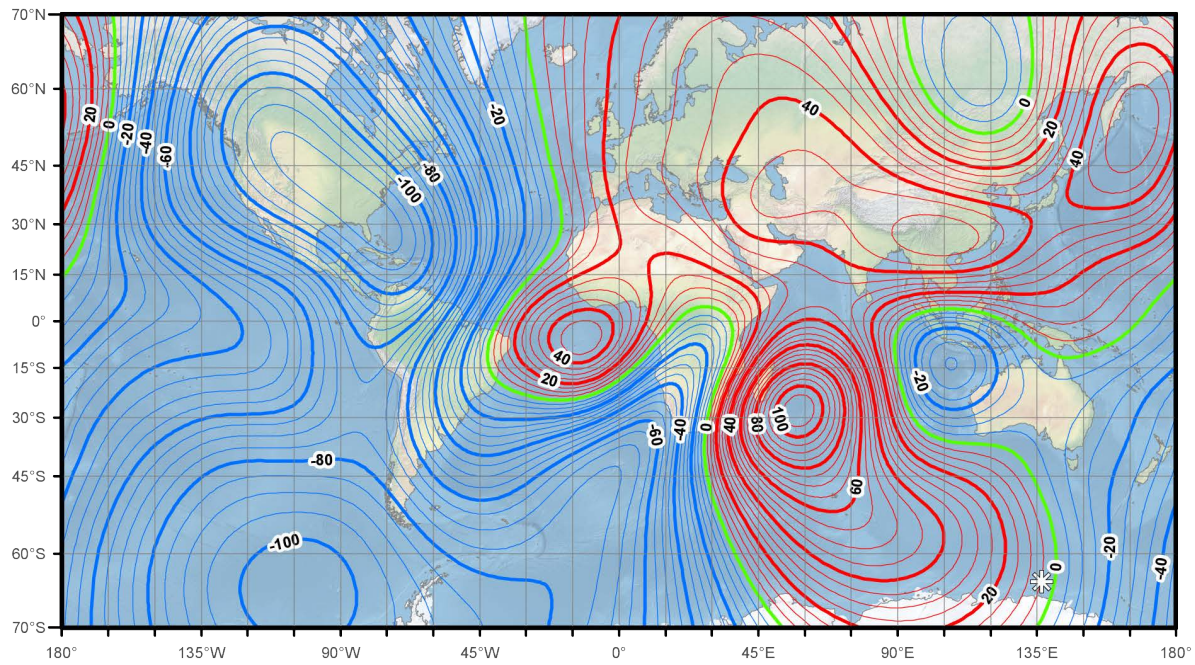
Annual change east component (Y). Contour interval is 5 nT / year, red contours positive (east) change; blue negative (west) change; green zero change. Mercator Projection.



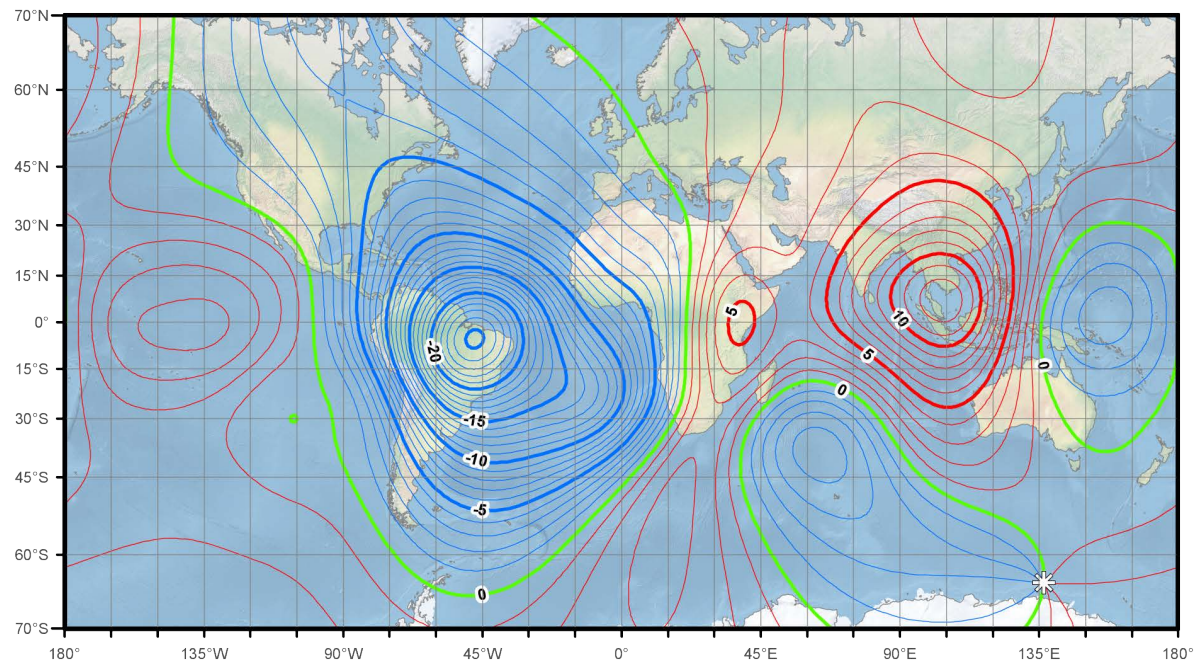
Annual change down component (Z). Contour interval is 5 nT / year, red contours positive (down) change; blue negative (up) change; green zero change. Mercator Projection.



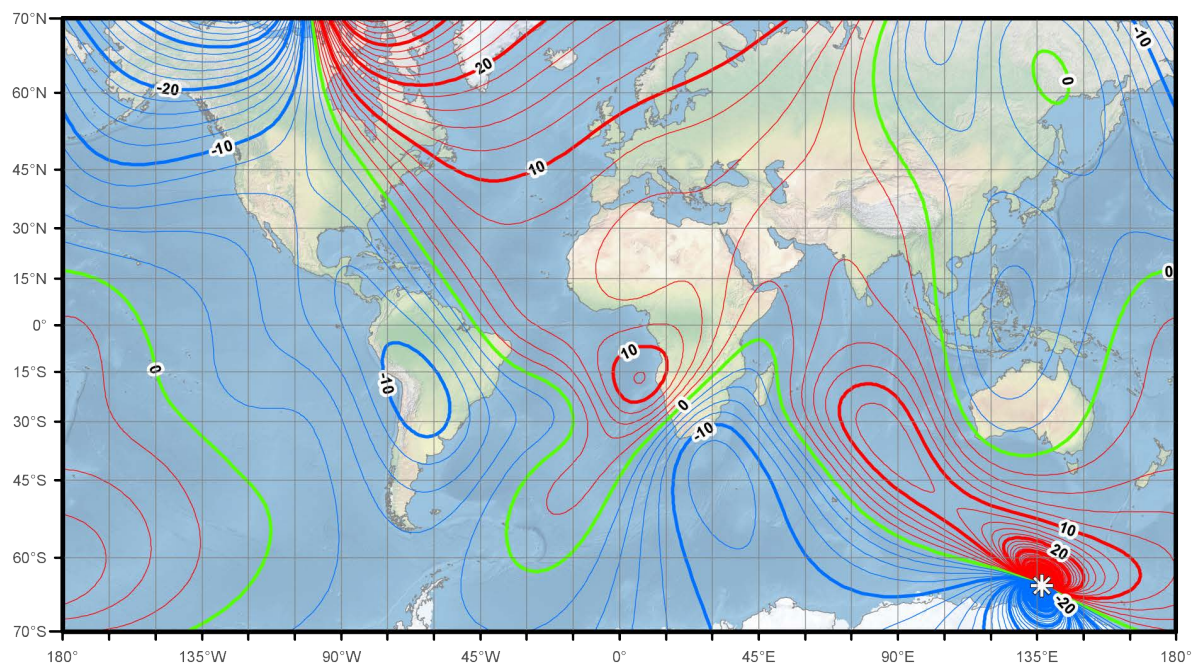
Annual change horizontal intensity (H). Contour interval is 5 nT / year, red contours positive change; blue negative change; green zero change. Mercator Projection.



Annual change total intensity (F). Contour interval is 5 nT / year, red contours positive change; blue negative change; green zero change. Mercator Projection.

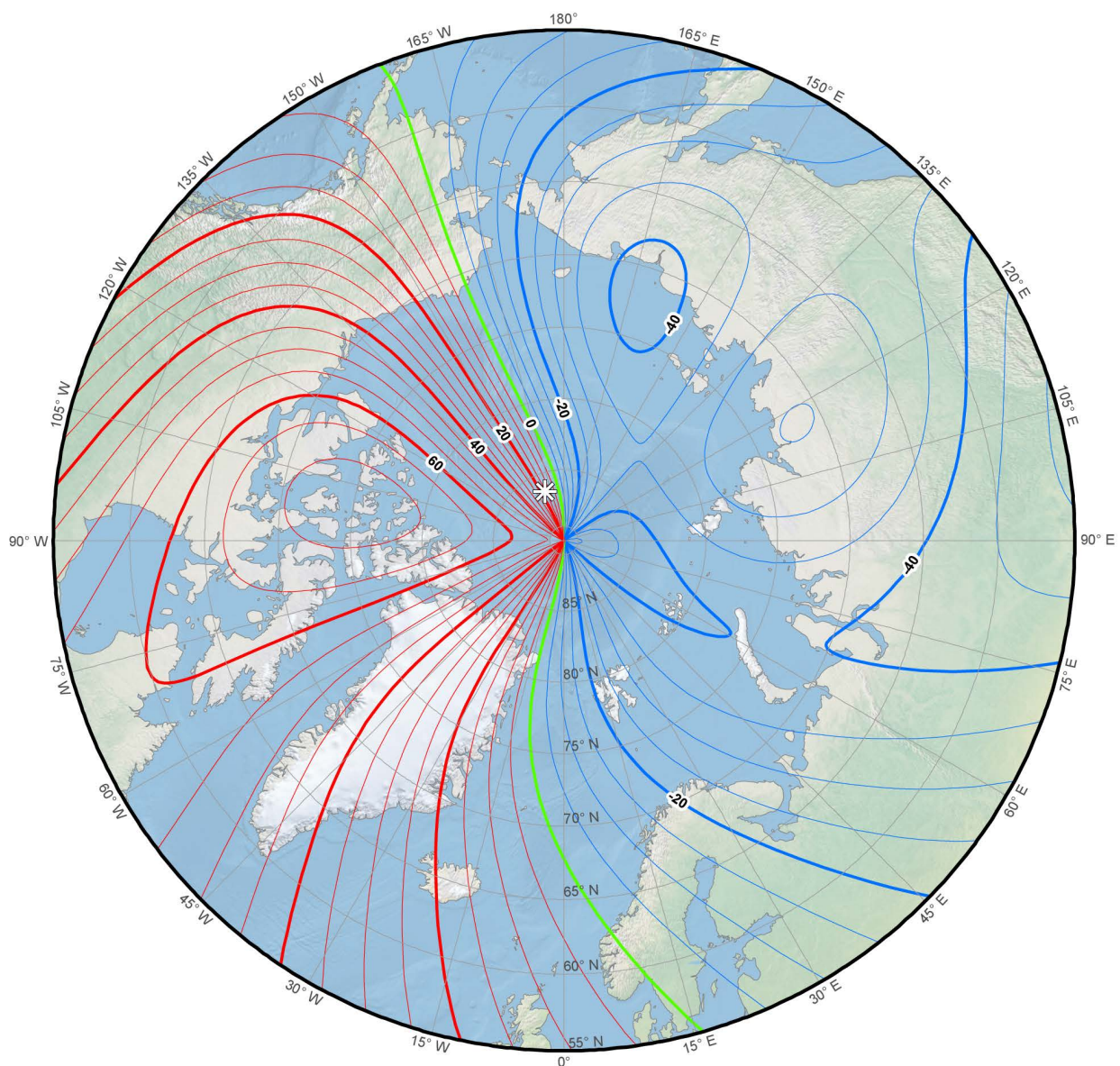


Annual change inclination (I). Contour interval is 1 arc-minute / year, red contours positive (downward) change; blue negative (upward) change; green zero change. Mercator Projection.

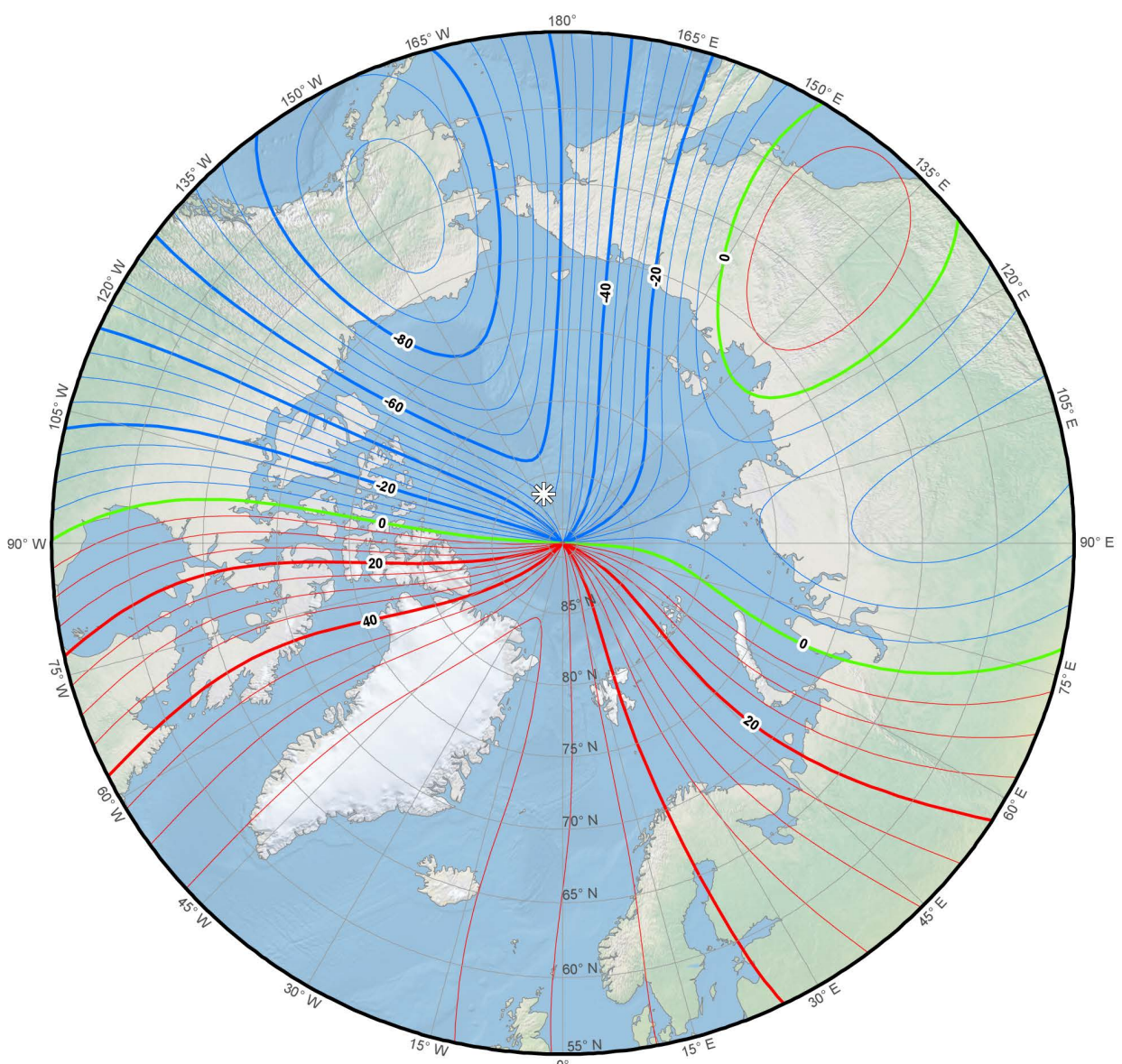


Annual change declination (D). Contour interval is 2 arc-minutes / year, red contours positive (clockwise) change; blue negative (counter-clockwise) change; green zero change. Mercator Projection.

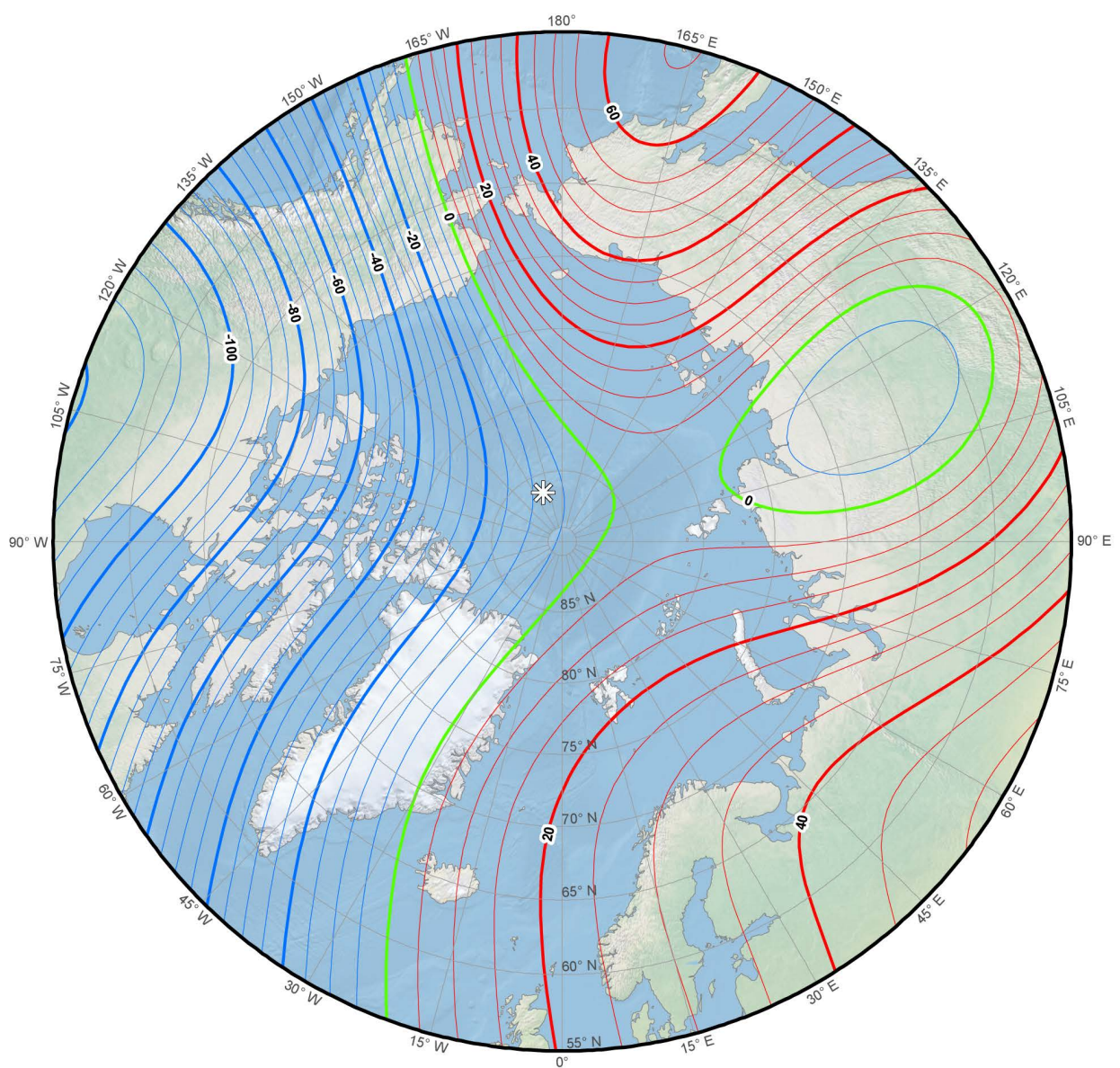
SECULAR VARIATION MAPS: NORTH POLAR STEREOGRAPHIC PROJECTION



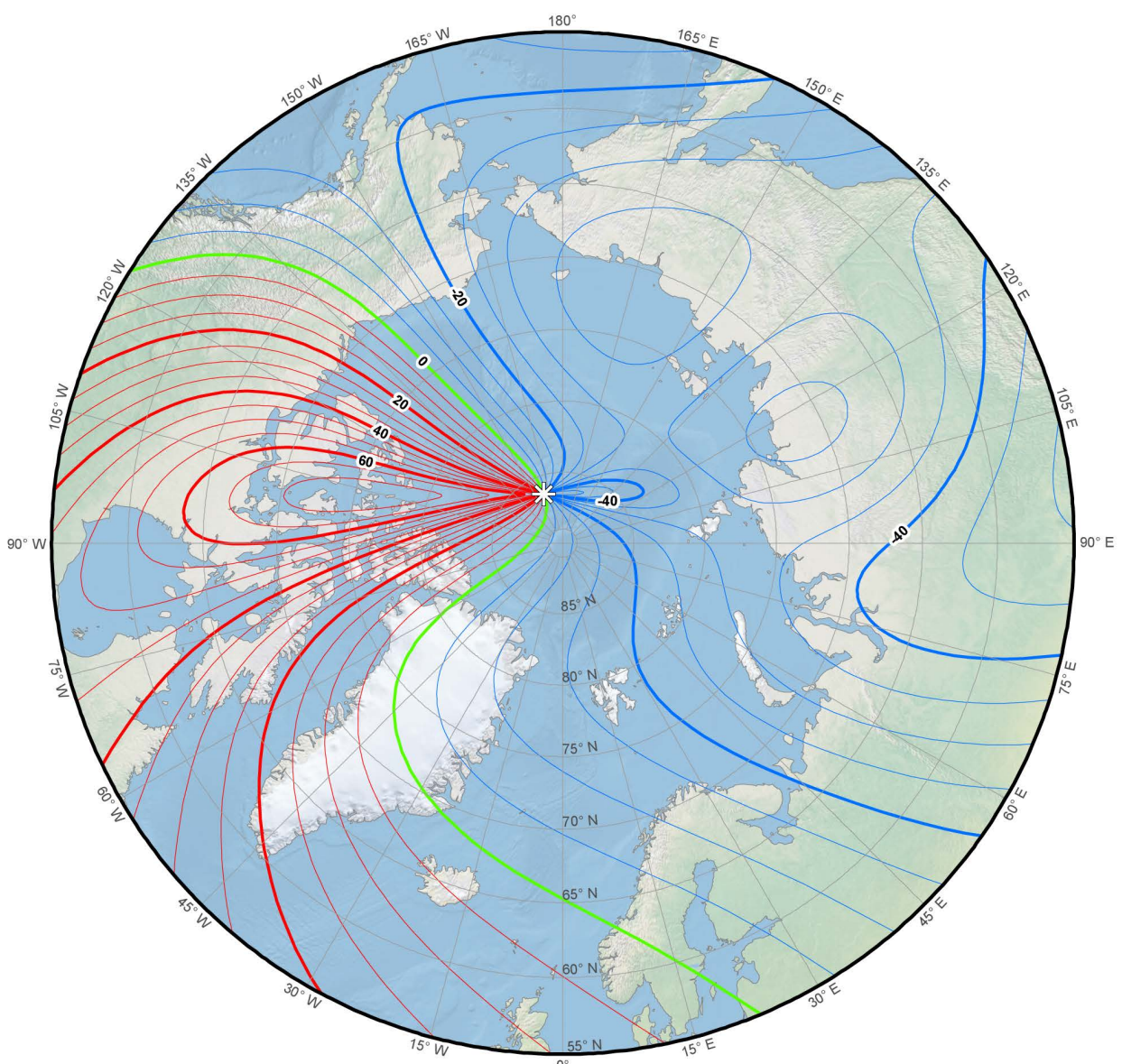
Annual change north component (X). Contour interval is 5 nT / year, red contours positive (north) change; blue negative (south) change; green zero change. North Polar Region. Polar Stereographic Projection.



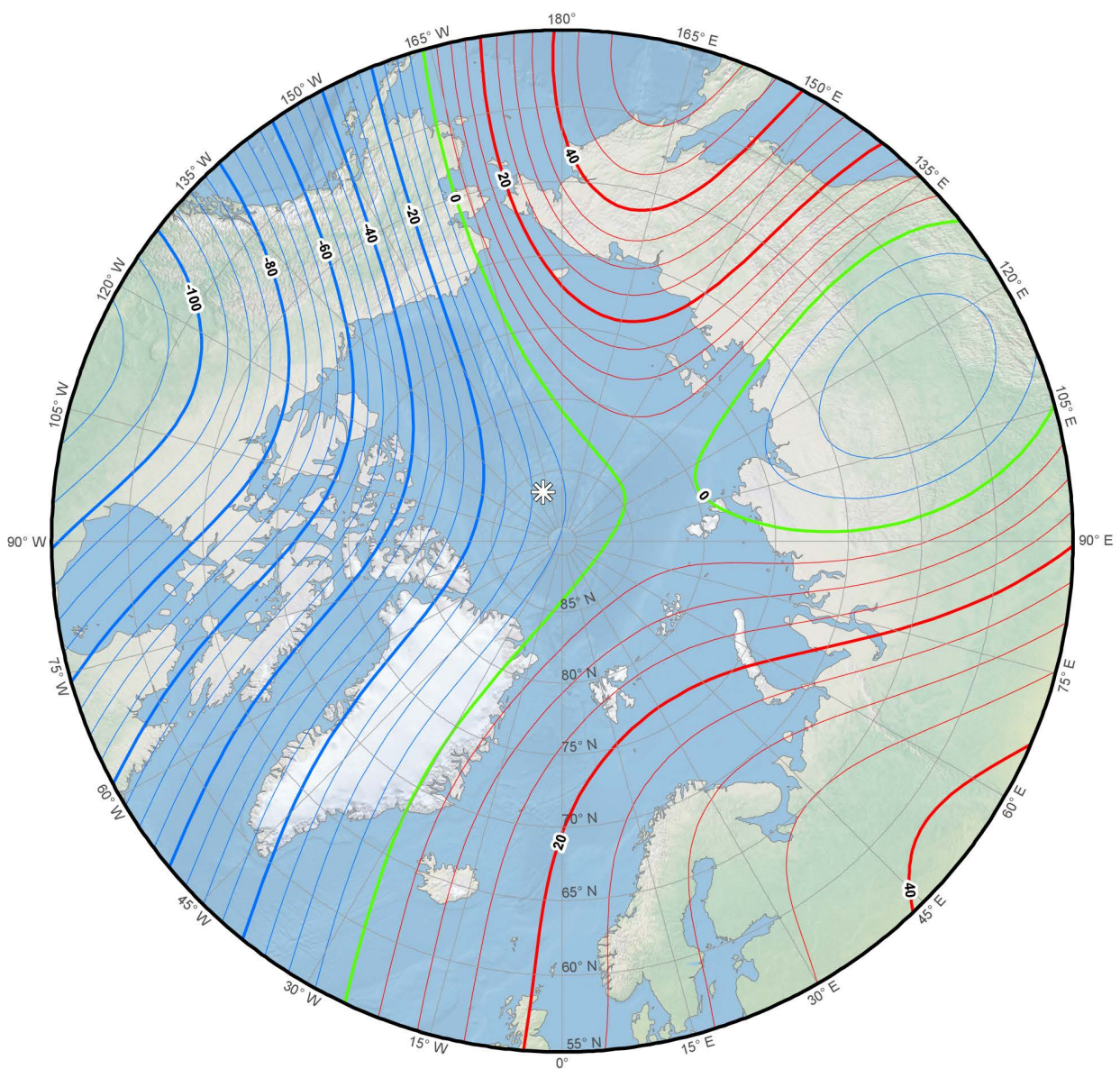
Annual change east component (Y). Contour interval is 5 nT / year, red contours positive (east) change; blue negative (west) change; green zero change. North Polar Region. Polar Stereographic Projection.



Annual change down component (Z). Contour interval is 5 nT / year, red contours positive (down) change; blue negative (up) change; green zero change. Polar Stereographic Projection.



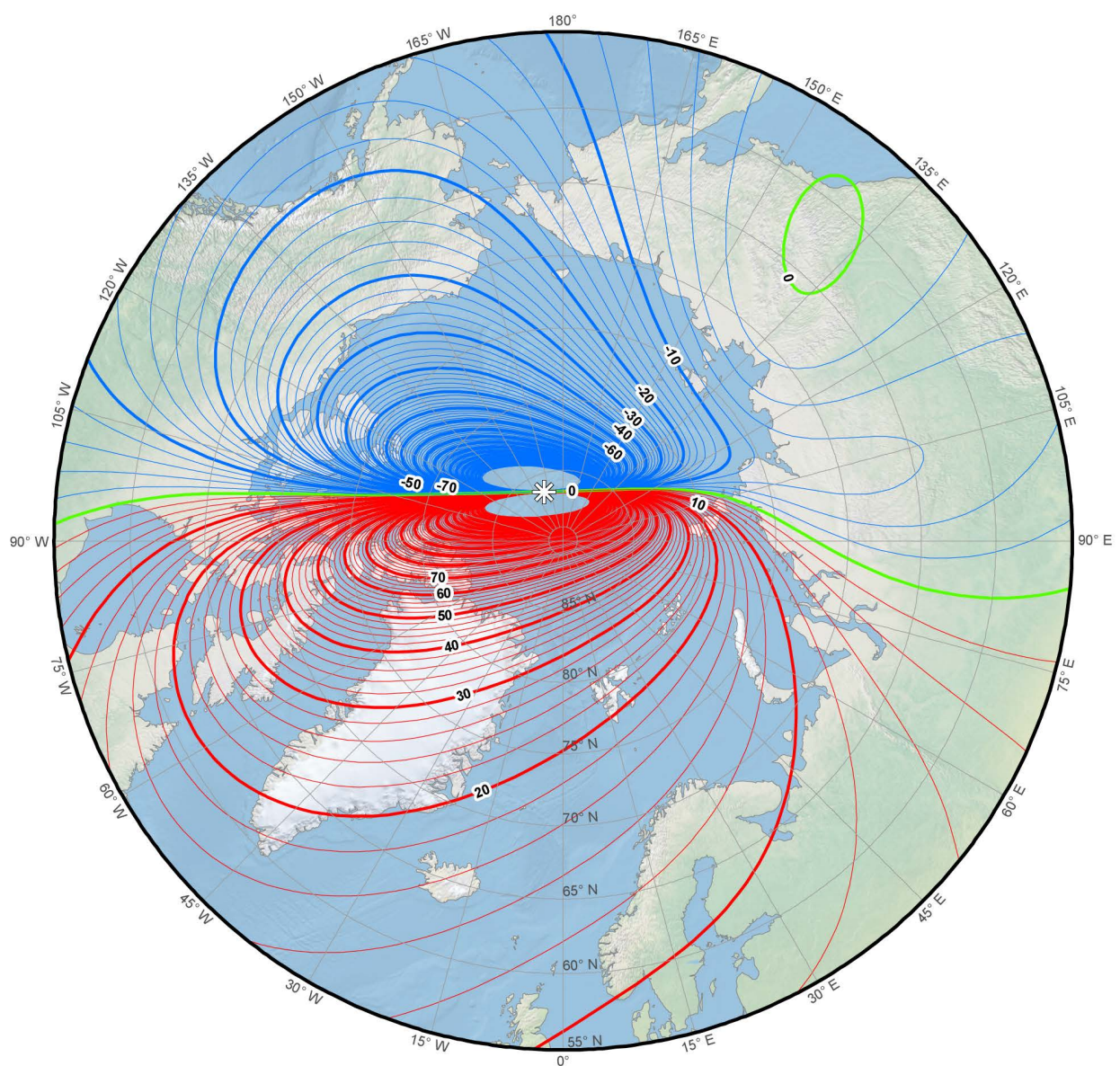
Annual change horizontal intensity (H). Contour interval is 5 nT / year, red contours positive change; blue negative change; green zero change. North Polar Region. Polar Stereographic Projection.



Annual change total intensity (F). Contour interval is 5 nT / year, red contours positive change; blue negative change; green zero change. North Polar Region. Polar Stereographic Projection.

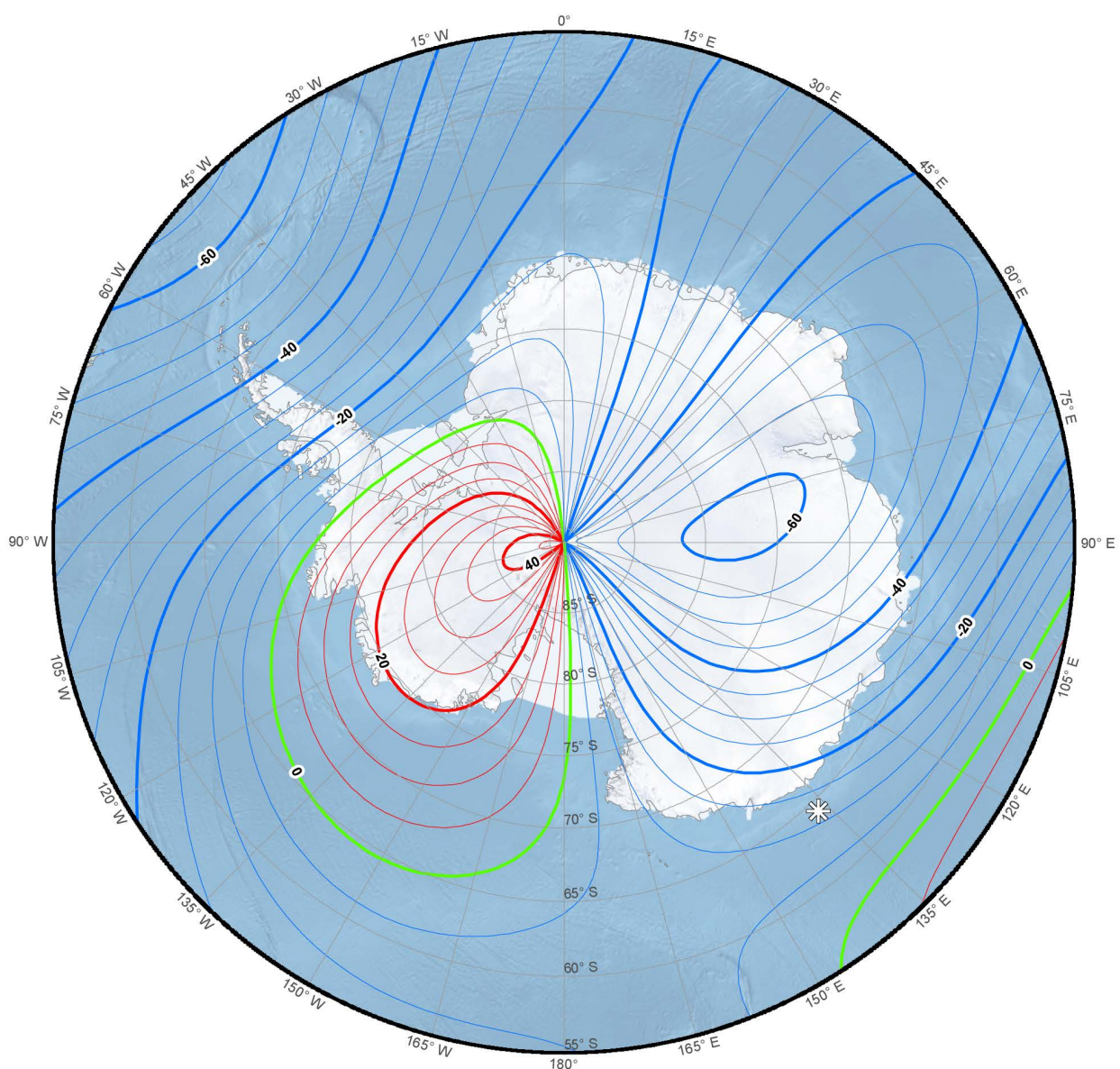


Annual change inclination (I). Contour interval is 1 arc-minute / year, red contours positive (downward) change; blue negative (upward) change; green zero change. North Polar Region. Polar Stereographic Projection.

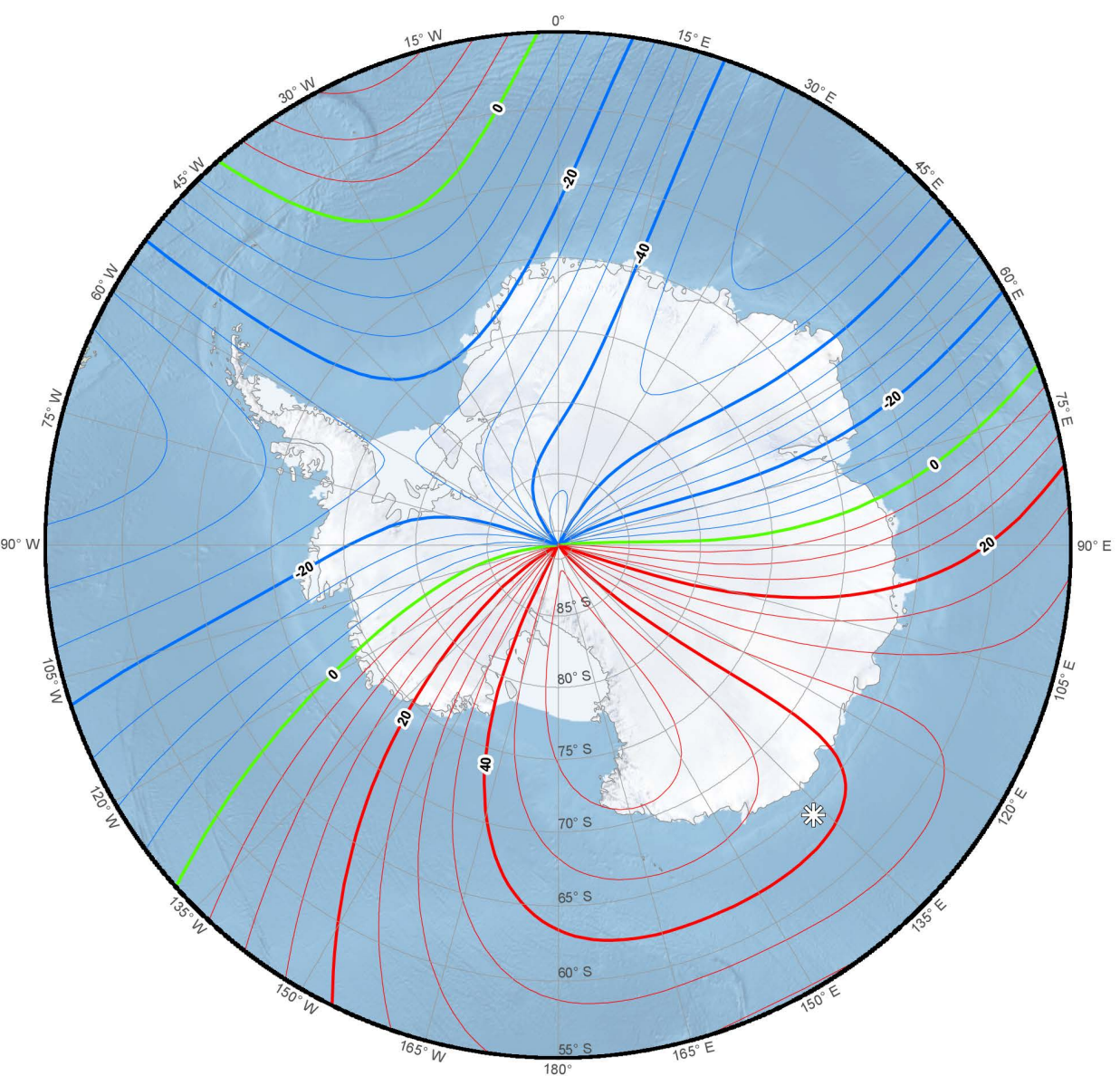


Annual change declination (D). Contour interval is 2 arc-minutes / year, red contours positive (clockwise) change; blue negative (counter- clockwise) change; green zero change. North Polar Region. Polar Stereographic Projection.

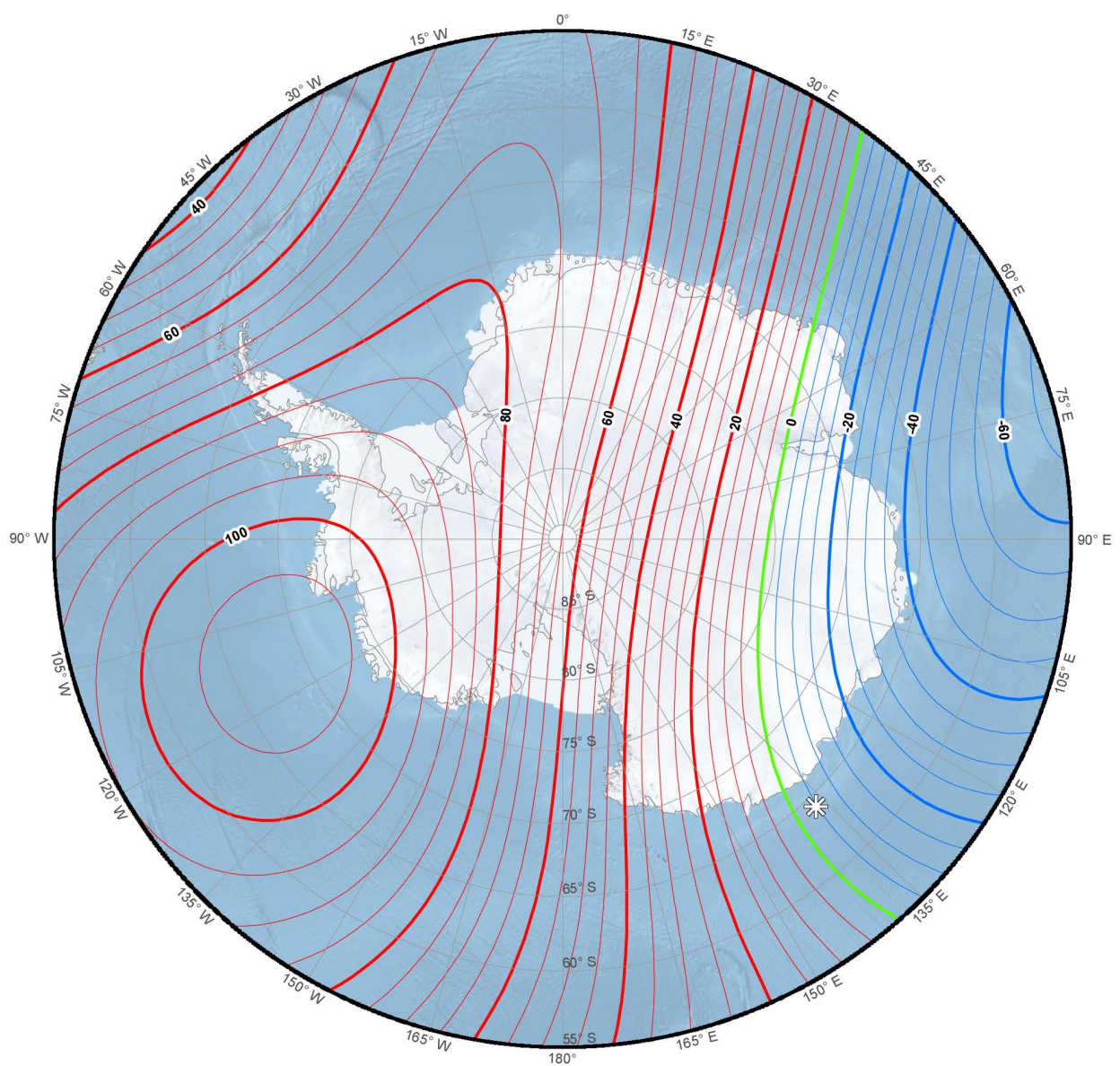
SECULAR VARIATION MAPS: SOUTH POLAR STEREOGRAPHIC PROJECTION



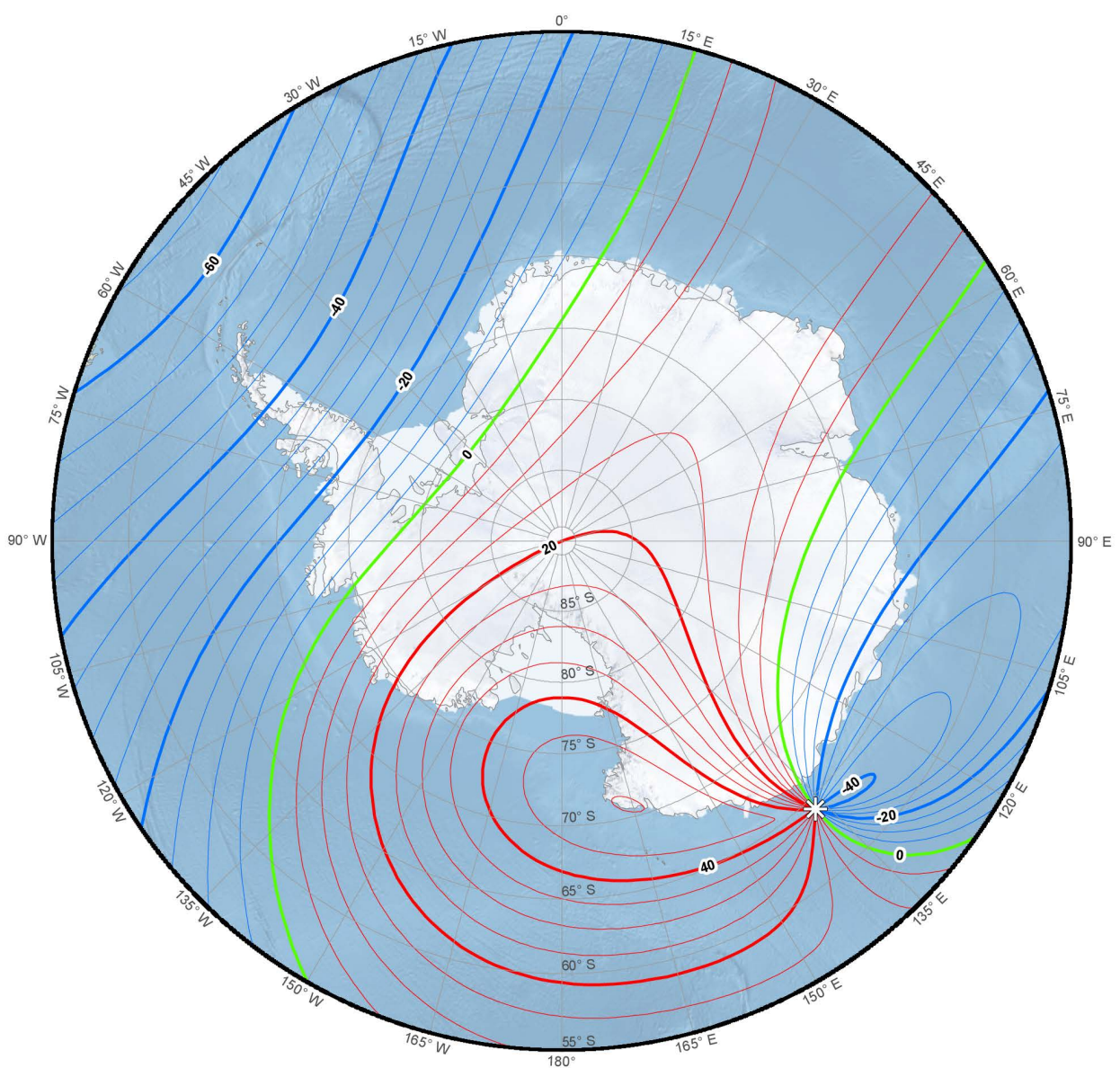
Annual change north component (X). Contour interval is 5 nT / year, red contours positive (north) change; blue negative (south) change; green zero change. South Polar Region. Polar Stereographic Projection.



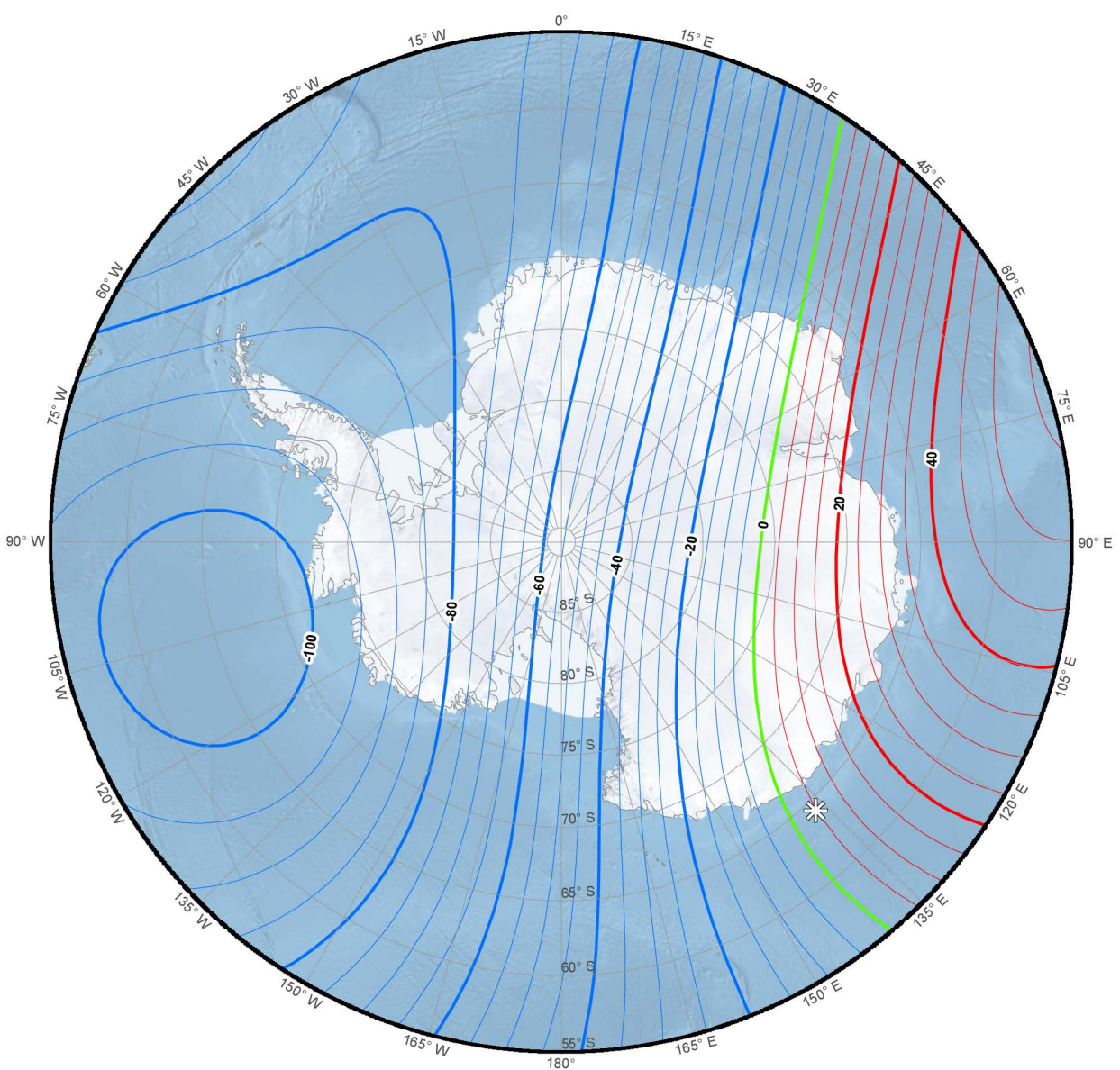
Annual change east component (Y). Contour interval is 5 nT / year, red contours positive (east) change; blue negative (west) change; green zero change. South Polar Region. Polar Stereographic Projection.



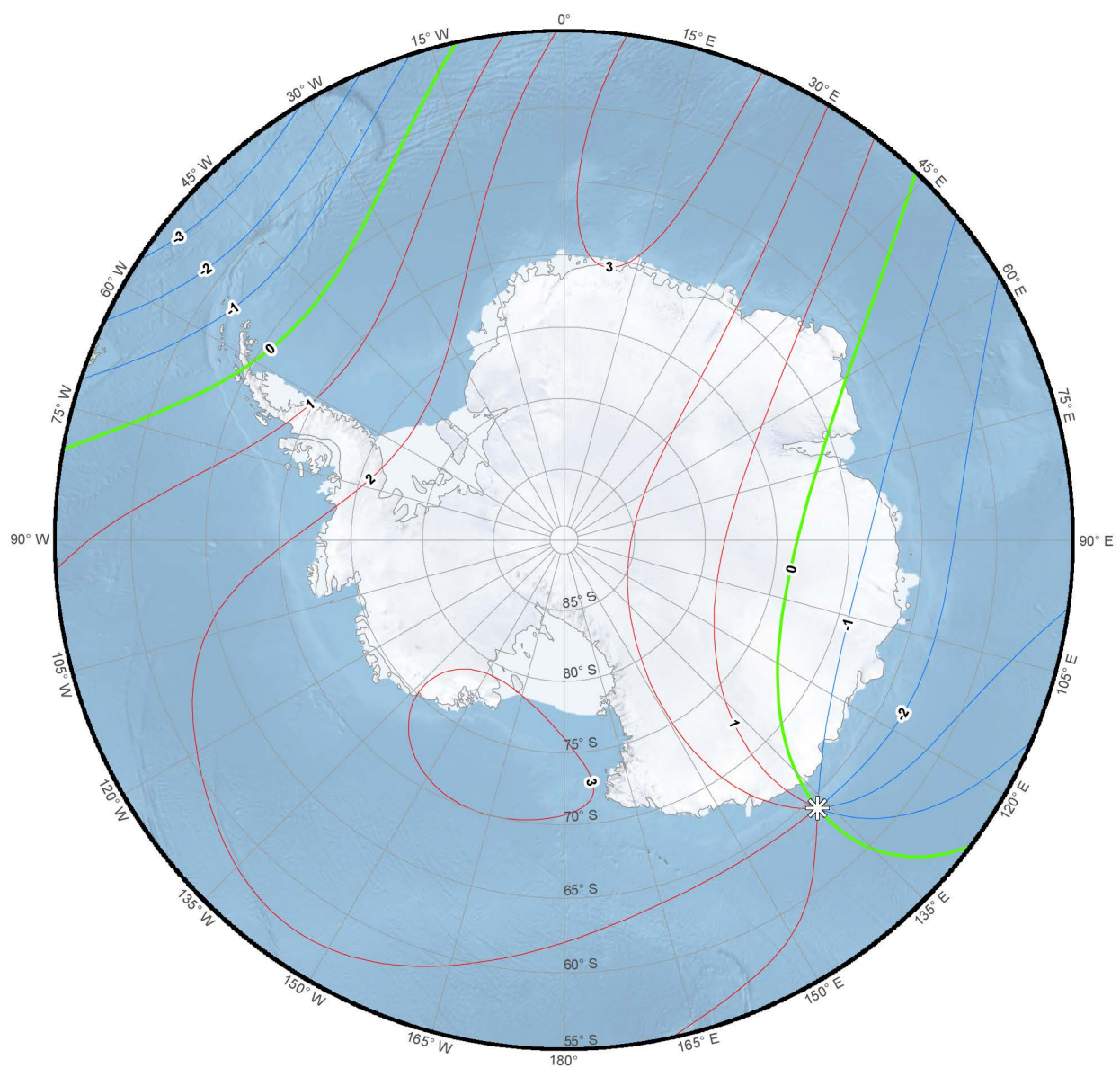
Annual change down component (Z). Contour interval is 5 nT / year, red contours positive (down) change; blue negative (up) change; green zero change. South Polar Region. Polar Stereographic Projection.



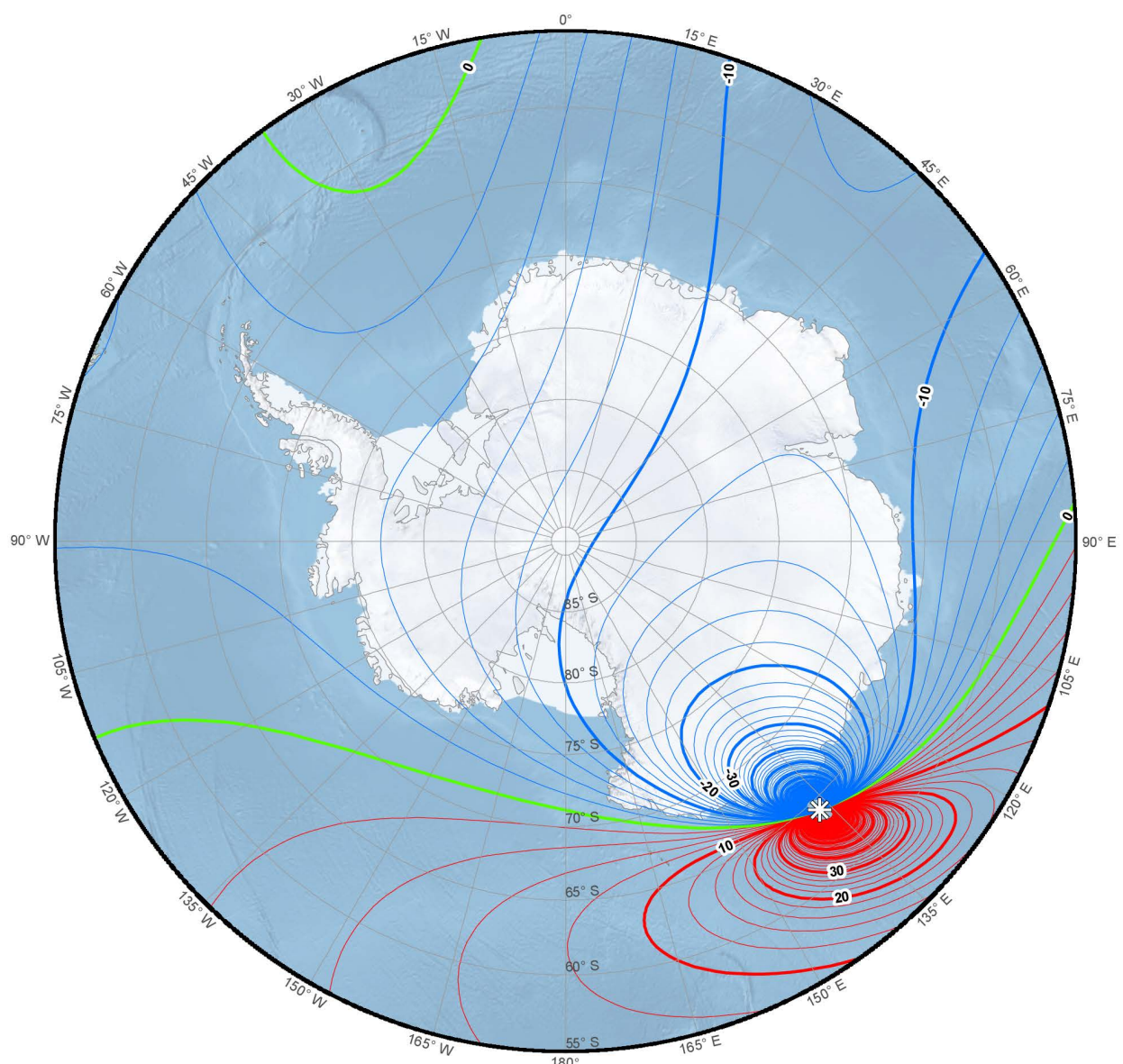
Annual change horizontal intensity (H). Contour interval is 5 nT / year, red contours positive change; blue negative change; green zero change. South Polar Region. Polar Stereographic Projection.



Annual change total intensity (F). Contour interval is 5 nT / year, red contours positive change; blue negative change; green zero change. South Polar Region. Polar Stereographic Projection.

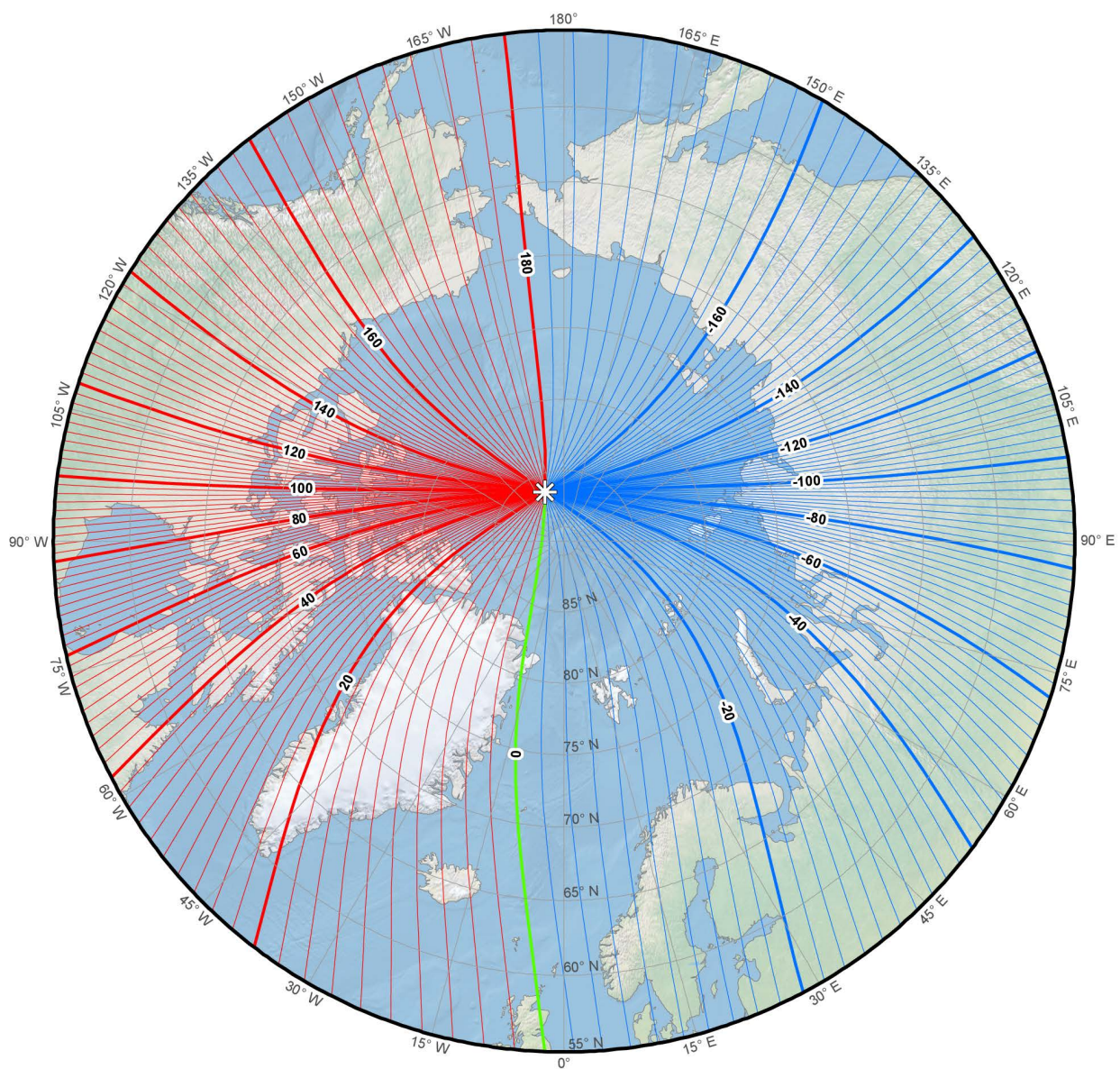


Annual change inclination (I). Contour interval is 1 arc-minute / year, red contours positive (downward) change; blue negative (upward) change; green zero change. South Polar Region. Polar Stereographic Projection.

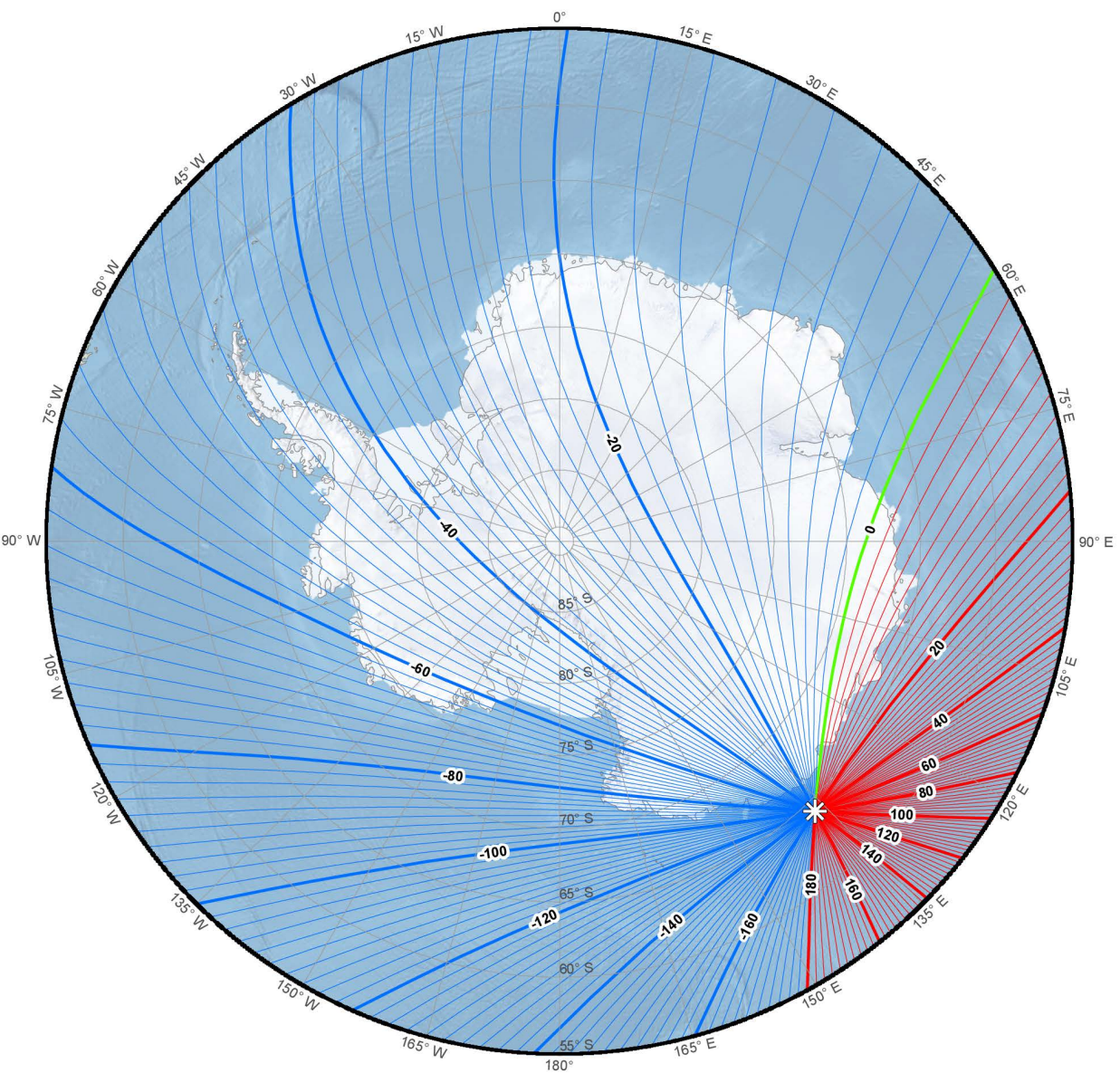


Annual change declination (D). Contour interval is 2 arc-minutes / year, red contours positive (clockwise) change; blue negative (counter-clockwise) change; green zero change. South Polar Region. Polar Stereographic Projection.

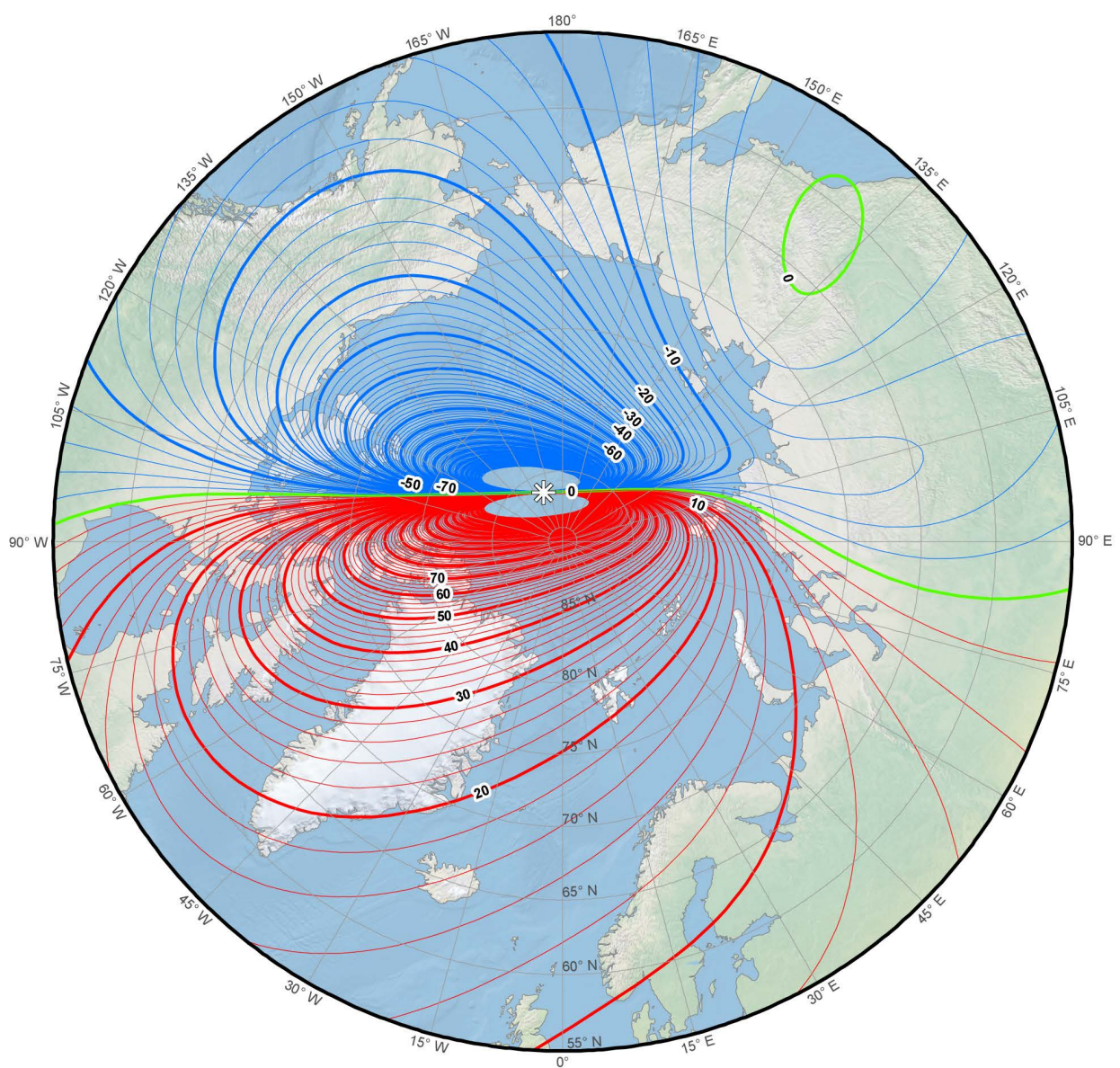
GRID VARIATION MAPS: POLAR STEREOGRAPHIC PROJECTION



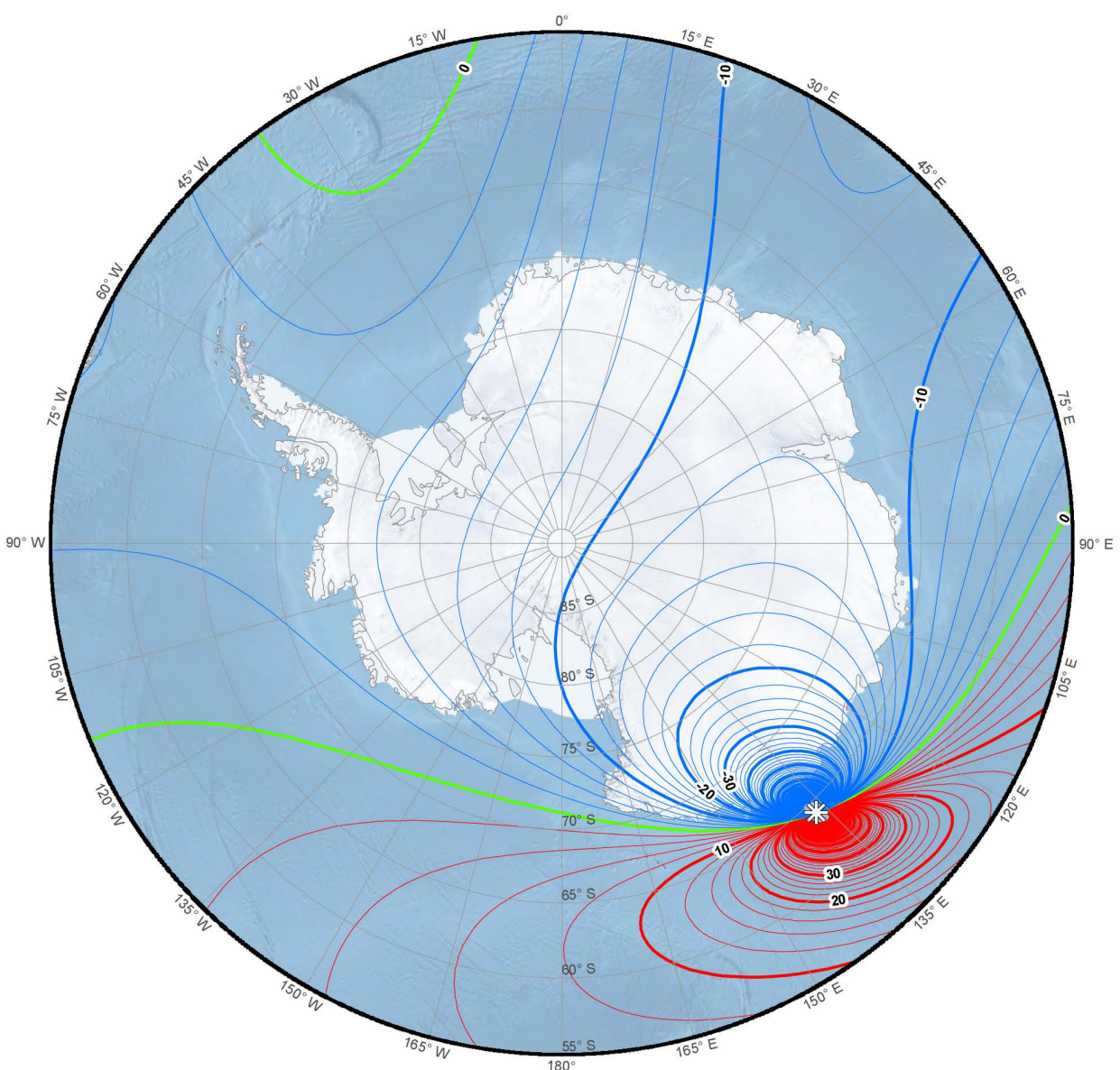
Main field grid variation (GV). Contour interval is 2 degrees, red contours positive; blue negative; green zero line. North Polar Region. Polar Stereographic Projection.



Main field grid variation (GV). Contour interval is 2 degrees, red contours positive; blue negative; green zero line. South Polar Region. Polar Stereographic Projection.

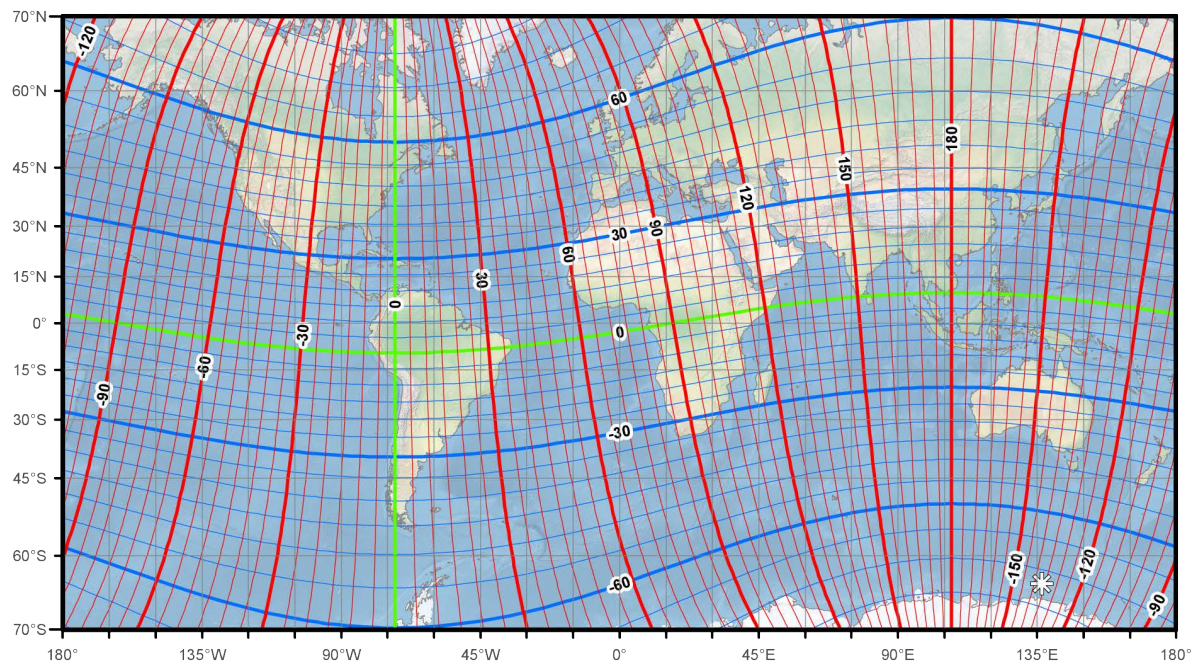


Annual change grid variation (GV). Contour interval is 2 arc-minutes / year, red contours positive (clockwise); blue negative (counter-clockwise); green zero line. North Polar Region. Polar Stereographic Projection.



Annual change grid variation (GV). Contour interval is 2 arc-minutes / year, red contours positive (clockwise); blue negative (counter-clockwise); green zero line. South Polar Region. Polar Stereographic Projection.

GEO MAGNETIC LONGITUDE AND LATITUDE



Geomagnetic longitude and latitude. Mercator projection.

5. REFERENCES AND BIBLIOGRAPHY

- Abramowitz, M. and I.A. Stegun, 1972. *Handbook of mathematical functions with formulas, graphs, and mathematical tables*. Washington, D.C.: U.S. Dept. of Commerce, National Bureau of Standards.
- Alken, P., S. Maus, A. Chulliat, and C. Manoj, 2015. NOAA/NGDC Candidate Models for the 12th generation International Geomagnetic Reference Field. *Earth Planets Space*, submitted.
- Backus, G., R.L. Parker, and C. Constable, 1996. *Foundations of geomagnetism*. Cambridge (UK): Cambridge University Press.
- Clarke, E., O. Baillie, S.J. Reay, and C.W. Turbitt, 2013. A method for the near real-time production of quasi-definitive magnetic observatory data. *Earth Planets Space*, 65, 1363-1374. [doi:10.5047/eps.2013.10.001](https://doi.org/10.5047/eps.2013.10.001)
- Defense Mapping Agency, 1993. *Military specification for World Magnetic Model (WMM)*. Document MIL-W-89500. Retrieved from <http://www.tpub.com/content/MIL-SPEC/MIL-W/MIL-W-89500/>
- Friis-Christensen, E., H. Lühr and G. Hulot, 2006. Swarm: A constellation to study the Earth's magnetic field. *Earth Planets Space*, 58, 351-358. [doi:10.1186/BF03351933](https://doi.org/10.1186/BF03351933)
- Gradshteyn, I.S. and I.M. Ryzhik, 1994. *Table of integrals, series and products* (5th ed). San Diego: Academic Press.
- Heiskanen, W. and H. Moritz, 1967. *Physical geodesy*. San Francisco: W.H. Freeman and Company.
- Jankowski, J. and C. Sucksdröff, 1996. *Guide for magnetic measurements and observatory practice*. Boulder: International Association of Geomagnetism and Aeronomy. Retrieved from http://www.iugg.org/IAGA/iaga_pages/pdf/IAGA-Guide-Observatories.pdf
- Kan, J.R. and L.C. Lee, 1979. Energy coupling function and solar wind magnetosphere dynamo. *Geophys. Res. Lett.*, 6, 577–580. [doi:10.1029/GL006i007p00577](https://doi.org/10.1029/GL006i007p00577)
- Langel, R.A., 1987. The main field. In *Geomagnetism*, edited by J.A. Jacobs, Academic Press, 249-512.
- Lemoine, F.G., S.C. Kenyon, J.K. Factor, R.G. Trimmer, N.K. Pavlis, D.S. Chinn, C.M. Cox, S.M. Klosko, S.B. Luthcke, M.H. Torrence, Y.M. Wang, R.G. Williamson, E.C. Pavlis, R.H. Rapp and T.R. Olson, 1998. *The development of the joint NASA GSFC and NIMA Geopotential Model EGM96*. Technical Report NASA/TP-1998-206861, NASA Goddard Space Flight Center, Greenbelt, Maryland.
- Lühr, H. and S. Maus, 2010. Solar cycle dependence of quiet-time magnetospheric currents and a model of their near-Earth magnetic fields. *Earth Planets Space*, 62, 843-848. [doi:10.5047/eps.2010.07.012](https://doi.org/10.5047/eps.2010.07.012)
- Macmillan, S., 2007. Observatories, Overview. In *Encyclopedia of geomagnetism and paleomagnetism*, edited by D. Gubbins and E. Herrero-Bervera, Springer, 708-711.

- Macmillan, S. and N. Olsen, 2013. Observatory data and the Swarm mission. *Earth Planets Space*, 65, 1355-1362. [doi:10.5047/eps.2013.07.011](https://doi.org/10.5047/eps.2013.07.011)
- Maus, S. and P. Weidelt, 2004. Separating magnetospheric disturbance magnetic field into external and transient internal contributions using 1D conductivity model of the Earth. *Geophys. Res. Lett.*, 31, L12614. [doi:10.1029/2004GL020232](https://doi.org/10.1029/2004GL020232)
- Maus, S. and H. Lühr, 2005. Signature of the quiet-time magnetospheric magnetic field and its electromagnetic induction in the rotating Earth. *Geophys. J. Int.*, 162, 755-763. [doi:10.1111/j.1365-246X.2005.02691.x](https://doi.org/10.1111/j.1365-246X.2005.02691.x)
- Maus, S., F. Yin, H. Lühr, C. Manoj, M. Rother, J. Rauberg, I. Michaelis, C. Stolle and R. D. Müller, 2008. Resolution of direction of oceanic magnetic lineations by the sixth-generation lithospheric magnetic field model from CHAMP satellite magnetic measurements. *Geochem. Geophys. Geosyst.*, 9, Q07021. [doi:10.1029/2008GC001949](https://doi.org/10.1029/2008GC001949)
- Maus, S. et al., 2009. EMAG2: A 2-arc min resolution Earth Magnetic Anomaly Grid compiled from satellite, airborne, and marine magnetic measurements. *Geochem. Geophys. Geosyst.*, 10, Q08005. [doi:10.1029/2009GC002471](https://doi.org/10.1029/2009GC002471)
- Maus, S., S. Macmillan, S. McLean, B. Hamilton, A. Thomson, M. Nair and C. Rollins 2010. The US/UK World Magnetic Model for 2010-2015, NOAA Technical Report NESDIS/NGDC. Available at www.geomag.bgs.ac.uk/documents/WMM2010_Report.pdf and www.ngdc.noaa.gov/geomag/WMM/data/WMM2010/WMM2010_Report.pdf.
- Merrill, R.T., M.W. McElhinny and P.L. McFadden, 1996. *The magnetic field of the earth: paleomagnetism, the core and the deep mantle*. San Diego: Academic Press.
- NATO Standardization Agency, 2011. *STANAG 7172 Use of Geomagnetic Models* (2nd ed).
- Olsen, N., L. Tøffner-Clausen, T.J. Sabaka, P. Brauer, J.M.G. Merayo, J.L. Jørgensen, J.-M. Léger, O.V. Nielsen, F. Primdahl and T. Risbo, 2003. Calibration of the Ørsted vector magnetometer. *Earth Planets and Space*, 55, 11-18. [doi:10.1186/BF03352458](https://doi.org/10.1186/BF03352458)
- Parkinson, W.D., 1983. *Introduction to geomagnetism*. Edinburgh: Scottish Academic Press.
- Peltier, A. and A. Chulliat, 2010. On the feasibility of promptly producing quasi-definitive magnetic observatory data. *Earth Planets Space*, 62, e5-e8. [doi:10.5047/eps.2010.02.002](https://doi.org/10.5047/eps.2010.02.002)
- Sugiura, M., 1964. Hourly values of the equatorial Dst for the IGY. *Ann. IGY*, 35, 9-45.
- Thomson, A.W.P. and V. Lesur, 2007. An improved geomagnetic data selection algorithm for global geomagnetic field modelling. *Geophys. J. Int.*, 169, 951-963. [doi:10.1111/j.1365-246X.2007.03354.x](https://doi.org/10.1111/j.1365-246X.2007.03354.x)
- Thomson, A.W.P., B. Hamilton, S. Macmillan and S.J. Reay, 2010. A novel weighting method for satellite magnetic data and a new global magnetic field model. *Geophys. J. Int.*, 181, 250-260. [doi:10.1111/j.1365-246X.2010.04510.x](https://doi.org/10.1111/j.1365-246X.2010.04510.x)